Master's thesis

NTNU
Norwegian University of Science and Technology
Faculty of Engineering
Department of Marine Technology

Eystein Holm Abrahamsen

Motion control problem in a multi-torus floating solar island concept, using tension cables – A 2D approach

Master's thesis in Marine Technology
Supervisor: Dong Trong Nguyen
Co-supervisor: Trygve Kristiansen
July 2022

NTNU
Norwegian University of
Science and Technology

Eystein Holm Abrahamsen

Motion control problem in a multi-torus floating solar island concept, using tension cables – A 2D approach

Master's thesis in Marine Technology
Supervisor: Dong Trong Nguyen
Co-supervisor: Trygve Kristiansen
July 2022

Norwegian University of Science and Technology
Faculty of Engineering
Department of Marine Technology

NTNU
Norwegian University of
Science and Technology

NTNU Trondheim
Norwegian University of Science and Technology
Department of Marine Technology

MSC THESIS DESCRIPTION SHEET

Name of the candidate: Eystein Holm Abrahamsen

Field of study: Marine cybernetics

Thesis title (Norwegian): Bevegeleseskontroll-problem for et multi-torus flytende soløy konsept, ved bruk av spenningskabler – En 2D tilnærming

Thesis title (English): Motion control problem in a multi-torus floating solar island concept, using tension cables – A 2D approach

Background

With rising global welfare for humans follows increased demand, in specific demand for energy in the form of electricity. With today's green paradigm shift in energy production, we may see a future surge in the photovoltaic industry. But since photovoltaics covers large areas, it is beneficial to place the photovoltaic plants in water bodies. Placed in ponds and other small water bodies, this not only prevents evaporation, but also generates power for the local community or for transporting. This in-land solar photovoltaic concept is already in use today and has been for some years. In more recent years, it has been proposed to move the floating photovoltaic scheme offshore. This could help provide power for other offshore installations, but will also assist in laying the foundations for power production of the future. The floating photovoltaics faces challenges during operation offshore, mostly concerning environmental forces having an impact on the structure carrying the solar panels. Control of floating photovoltaic can be used to solve these challenges; and hence extending the operation window. These bring to the interdisciplinary domain between marine control systems and marine structures.

Work description

1. Perform a background and literature review to provide information and relevant references on:
    - Modelling of flexible structures including 2D and 3D modelling. This should also include hydrodynamic modelling
    - Winch control

    Write a list with abbreviations and definitions of terms, explaining relevant concepts related to the literature study and project assignment.

2. Propose a control system using winch to reduce the motion of solar panels on the multi-torus floating photovoltaic concept.
    - From the literature review, briefly study the feasibility of using winch control on the multi-torus floating photovoltaic concept.
    - Propose a setup of winch and tensioned cables used for motion control for a 3D problem.
    - Propose a control algorithm to reduce the motions of the solar panels in varying sea states. This should be done in a 2D problem.
    - Propose a method to estimate the sea state as input to controller.

3. Modelling study for the control purpose for multi-torus in 2D problem.
    - Implement estimative calculations of tension and slack in solar panel carrying deck, deriving the required dimensions of the physical model scaled test setup.
    - Elaborate on the estimates, and develop a higher fidelity simulation of the system. This should be done in Matlab.
    - These simulations should be compared to the physical model scale tests, so robust simulations are needed before the physical model testing commences.

4. Execute the physical model scale test. The motion of the solar panel deck and the tension induced by the winching mechanism should be recorded. These recorded data should be compared to the simulation results acquired earlier. This should be done in a chapter dedicated to comparing physical and numerical results.
    - Use these dimensions as starting point for physical model development in the program Rhinoceros. The model sketched here should be sent to the model constructors.
    - The physical components should be identified. It should also be identified how to acquire these components, whether they are already available at the campus site, or if ordering the components online is needed.
    - Propose a method to estimate the sea state in the model scale test setup.

Tentative:

1. Estimate energy used by the control systems.
2. Investigate feasibility of actuators in the lab.

Specifications

The scope of work may prove to be larger than initially anticipated. By the approval from the supervisor, described topics may be deleted or reduced in extent without consequences regarding grading.

The candidate shall present personal contribution to the resolution of problems within the scope of work. Theories and conclusions should be based on mathematical derivations and logic reasoning identifying the various steps in the deduction.

The report shall be organized in a logical structure to give a clear exposition of background, results, assessments, and conclusions. The text should be brief and to the point, with a clear language. Rigorous mathematical deductions and illustrating figures are preferred over lengthy textual descriptions. The report shall have font size 11 pts., and it is not expected to be longer than 60-80 A4 pages, from introduction to conclusion, unless otherwise agreed upon. It shall be written in English (preferably US) and contain the following elements: Title page, abstract, acknowledgements, thesis specification, list of symbols and acronyms, table of contents, introduction with objective, background, and scope and delimitations, main body with problem formulations, derivations/developments and results, conclusions with recommendations for further work, references, and optional appendices. All figures, tables, and equations shall be numerated. The original contribution of the candidate and material taken from other sources shall be clearly identified. Work from other sources shall be properly acknowledged using quotations and a Harvard citation style (e.g. *natbib* Latex package). The work is expected to be conducted in an honest and ethical manner, without any sort of plagiarism and misconduct. Such practice is taken very seriously by the university and will have consequences. NTNU can use the results freely in research and teaching by proper referencing, unless otherwise agreed upon.

The thesis shall be submitted with a printed and electronic copy to the main supervisor, with the printed copy signed by the candidate. The final revised version of this thesis description must be included. The report must be submitted according to NTNU procedures. Computer code, pictures, videos, data series, and a PDF version of the report shall be included electronically with all submitted versions.

Start date: January 15, 2022. **Due date:** June 11, 2022.

Supervisor: Dong Trong Nguyen
Co-advisor(s): Trygve Kristiansen

Trondheim, 14.01.2022, Eystein Holm Abrahamsen

Dong Trong Nguyen
Digitally signed by Dong Trong Nguyen
Date: 2022.07.05 10:20:21 +02'00'

Dong Trong Nguyen
Supervisor

Preface

This thesis concludes my studies as a Master of Science within Marine Cybernetics at NTNU at the Department of Marine Technology. The work is conducted during the spring semester of 2022, and the work gives 30 Norwegian studying credits (ECTS).

The general topic was chosen from a list of possible topics suggested by professor Dong Trong Nguyen, who has been my main supervisor. After some discussion with Dong, the topic was chosen to revolve around a multi-torus floating solar island concept. This concept was proposed by professor Trygve Kristiansen, who has been my co-supervisor.

The reader should have some knowledge about control theory, hydrodynamics, and structural dynamics.

Trondheim, 05.07.2022

Eystein Holm Abrahamsen

Acknowledgements

A big thanks goes to my main supervisor, prof. Dong Trong Nguyen, for fruitful problem solving sessions and excursions to the labs. Also a thanks goes to my co-supervisor and the envisioner of the floating solar island idea in the topic of this thesis, prof. Trygve Kristiansen, for useful input and discussions.

The work conducted in this thesis would not have been possible without the great efforts and experience of Trond Innset and Ole Erik Vinje in making and repairing the model used in this thesis. A big thanks is also due Robert Opland, Terje Røsten, and Torgeir Wahl, for providing guidance and ideas, and helping with instrumentation during model testing.

To my family, thank you for always supporting me during the five years spent here in Trondheim. To my office A2.007, thank you for intense work sessions and good times. And lastly, to my classmates in the class of 2017, thank you for five great years.

E.H.A.

Summary

Floating solar islands are emerging as markets and fields of research, and some academic and commercialized floating solar island concepts exist or are in operation. One academic concept that is in a phase of research and development is the multi-torus structure proposed by Trygve Kristiansen as a floating island supporting photovoltaic equipment. This concept takes the form of several concentric flexible toruses interconnected by trusses, with a flexible membrane solar panel carrying deck resting on top of the toruses. The island is designed to follow the waves in heave to a large extent. The solar deck is envisioned to be hanging freely in between the toruses, making it prone to resonant swinging motions. A solution to this problem was in this thesis proposed in the form of a semi-active control system.

The proposed control system is based on control of the natural frequency of the solar deck, instead of active control of the motion of the solar deck. This is necessary as direct active control requires a lot of energy to the actuators, and it is important to conserve energy on floating solar islands. The natural frequency of the solar deck is controlled by changing the tension in the solar deck. The control algorithm controls the tension in the solar deck by comparing the natural frequency of the solar deck calculated as a function of the current tension level, and the frequency of the present waves. The frequency of the waves is obtained by employing a wave frequency estimator based on the fast Fourier Transform of the measured heave response, since the structure is meant to follow the waves in heave.

A small scale model was built and tested in approximately a 1:10 scale of what is believed to be a fitting size for the multi-torus structure, demonstrating the control system. The model represents a 2D simplification of two consecutive torus cross sections with the solar deck freely hanging in between them. The resulting small scale model consisted of two rigid circular cylinders with a rectangular membrane solar deck hanging freely in between the cylinders. Optical motion capture markers from Qualisys were placed on the model, and the live data stream of the marker positions was used as input to the real-time wave frequency estimator. A linear actuator performing control action on the tension in the solar deck was initially supposed to be included in the model tests, but the actuator was not powerful enough to statically hold the needed tension. Moreover, the measured tension in the solar deck was not available as real-time data. This represented a step away from a closed-loop system, so the tension was changed by adjusting the tension using a manual chain hoist. Real-time wave frequency estimation was still performed by the Fast Fourier Transform algorithm. This algorithm was tested in regular and irregular waves for varying wave frequencies, solar deck tension levels, and sampling frequencies. The results showed that the Fast Fourier Transform can to an acceptable accuracy estimate the wave frequency also for irregular waves.

An empirical mapping of the response of the solar deck for varying solar deck tension levels and wave frequencies was created. The model was tested in regular waves with period T = 0.4 s up to 1.5 s with 0.1 s increments. The tension was varied from 10 N to 50 N with 5 N increments. The results showed that increasing the tension reduced the vertical motion of the solar deck to some extent. The middle of the solar deck had a peak at T = 0.6 s

for all tensions, with the largest values for a tension of 10 N. A special case wave period where the regular wave length is equal to the length between the cylinders or toruses was also tested. The period was then 0.566 s, and tension levels were tested from 5 N to 60 N with 5 N increments. These tests showed that 25 N was critical, as a peak in vertical motion in the middle of the solar deck was measured. However, due to the model test setup being of a 2D nature it was concluded to be unclear if the natural frequency of the solar deck or the model test setup had been tested.

For calculating the eigenfrequency of the solar deck as input to the controller, two main methods were proposed. One was based on approximating the solar deck as a string, while the other modelled the solar deck as discrete masses and springs. The string approximation gave results that agreed somewhat with the peaks noted from the empirical mapping. The discrete mass and spring model yielded erroneous eigenfrequencies, since the natural frequencies decreased for increasing tension levels, which was concluded to be unphysical.

It is concluded that the multi-torus floating island is promising, although the solar deck is prone to resonant swinging motions. A solution to this problem was proposed as a semi-active control system in this thesis. However, more research on the multi-torus structure is needed to converge towards optimal solutions and designs of its layout.

Sammendrag

Flytende soløyer dukker opp som markeder og forskningsfelt, og noen akademiske og kommersialiserte flytende soløy-konsepter eksisterer eller er i drift. Ett akademisk konsept som er i en fase av forskning og utvikling er multi-torus-strukturen foreslått av Trygve Kristiansen som en flytende øy som bærer solcelleutstyr. Dette konseptet har form av flere konsentriske fleksible toruser sammenkoblet av fjærer, med et fleksibelt solcellepanel-bærende membran-dekk som hviler oppå torusene. Øya er designet for å følge bølgene i hiv i stor grad. Soldekket er tenkt å henge fritt mellom torusene, noe som gjør det utsatt for resonante svingende bevegelser. En løsning på dette problemet er i denne oppgaven foreslått i form av et semi-aktivt kontrollsystem.

Det foreslåtte kontrollsystemet er basert på kontroll av soldekkets egenfrekvens, i stedet for aktiv kontroll av bevegelsen til soldekket. Dette er nødvendig da aktiv kontroll krever mye energi til aktuatorene, og det er viktig å spare energi på flytende soløyer. Soldekkets egenfrekvens kontrolleres ved å endre spenningen i soldekket. Kontrollalgoritmen styrer spenningen i solcelleanlegget ved å sammenligne egenfrekvensen til soldekket beregnet som en funksjon av nåværende spenningsnivå, med frekvensen til de nåværende bølgene. Frekvensen til bølgene fås ved å bruke en bølgeestimator basert på 'Fast Fourier Transform' av den målte hivresponsen, siden strukturen er ment å følge bølgene i hiv.

En modell i liten skala ble bygget og testet i omtrent 1:10 skala av det som antas å være en passende størrelse for multi-torus-strukturen, for å demonstrere kontrollsystemet. Modellen representerer en 2D-forenkling av to påfølgende torus-tverrsnitt med solcelledekket fritt hengende mellom dem. Den resulterende småskalamodellen besto av to stive sirkulære sylindre med et rektangulært membransoldekk hengende fritt mellom sylindrene. Optiske bevegelsesmålingsmarkører fra Qualisys ble plassert på modellen, og strømmen av sanntidsdata av markørposisjonene ble brukt som input til bølgefrekvensestimatoren i sanntid. En lineær aktuator som gjorde kontrollpådrag på spenningen i solcelledekket skulle i utgangspunktet være inkludert i modelltestene, men aktuatoren var ikke kraftig nok til å holde den nødvendige statiske spenningen. Dessuten var den målte spenningen i soldekket ikke tilgjengelig som sanntidsdata. Dette representerte et skritt bort fra et lukket sløyfesystem, så spenningen ble endret ved å justere spenningen ved hjelp av en manuell kjettingtalje. Bølgefrekvensestimering i sanntid ble likevel utført av Fast Fourier Transform algoritmen. Denne algoritmen ble testet i regulære og uregelmessige bølger for varierende bølgefrekvenser, spenningsnivåer på soldekket og samplingsfrekvenser. Resultatene viste at Fast Fourier Transform algoritmen kan med en akseptabel nøyaktighet estimere bølgefrekvensen også for uregelmessige bølger.

En empirisk mapping av responsen til soldekket for varierende soldekkspenningsnivåer og bølgefrekvenser ble laget. Modellen ble testet i regulære bølger med periode T = 0,4 s opp til 1,5 s med inkrementer på 0,1 s. Spenningen ble variert fra 10 N til 50 N med inkrementer på 5 N. Resultatene viste at en økning av spenningen reduserte den vertikale bevegelsen til soldekket til en viss grad. Midten av soldekket hadde en topp på T = 0,6 s for alle spenninger, med de største verdiene for en spenning på 10 N. Et spesialtilfelle hvor den regulære bølgelengden er lik lengden mellom sylindrene eller torusene ble også testet.

Perioden var da 0,566 s, og spenningsnivåer ble testet fra 5 N til 60 N med inkrementer på 5 N. Disse testene viste at 25 N var kritisk, da det ble målt en topp i vertikal bevegelse midt på soldekket. Men på grunn av at oppsettet til den testede modellen var av en 2D-karakter ble det konkludert med at det var uklart om egenfrekvensen til solcelledekket eller modelltestoppsettet hadde blitt testet.

For å beregne egenfrekvensen til soldekket som input til kontrolleren, ble to hovedmetoder foreslått. Den ene var basert på å tilnærme soldekket som en streng, mens den andre modellerte soldekket som diskrete masser og fjærer. Strengetilnærmingen ga resultater som stemte til en viss grad med bevegelsestoppene notert fra den empiriske mappingen. Den diskrete masse- og fjærmodellen ga feil egenfrekvenser, siden egenfrekvensene sank for økende spenningsnivåer, noe som ble konkludert med å være ufysisk.

Det konkluderes med at den flytende multi-torus øya er lovende som konsept, selv om soldekket er utsatt for resonante svingende bevegelser. En løsning på dette problemet ble foreslått som et semi-aktivt kontrollsystem i denne oppgaven. Imidlertid er det nødvendig med mer forskning på multi-torus-konseptet for å konvergere mot optimale løsninger og design av utformingen.

Table of Contents

List of Figures

List of Tables

Nomenclature

Abbreviations

2D	Two-dimensional
3D	Three-dimensional
BVP	Boundary Value Problem
DAF	Dynamic Amplification Factor
DES	Discrete Event Simulation
DIT	Decimation In Time
DOF	Degree of Freedom
FPV	Floating photovoltaics
IMU	Inertial Measurement Unit
PID	Proportional - Integral - Derivative controller
PSC	Polymer Solar Cells
PV	Photovoltaics
RAO	Response Amplitude Operator
SISO	Single Input Single Output
ZFT	Zero Frequency Theory

Greek letters

ω	Angular frequency $[rad/s]$
ω_0	Natural frequency $[rad/s]$
ζ	Surface elevation $[m]$
ζ_a	Wave amplitude $[m]$
λ	Wave length $[m]$
ρ	Density $[kg/m^3]$

Roman letters

EA	Axial stiffness $[N]$
EI	Bending stiffness $[Nm^2]$
k	Wave number $[rad/m]$
A_{33}	Added mass in heave $[kg]$
B_{33}	Damping in heave $[kg/s]$
C_{33}	Water plane stiffness in heave $[N/m]$
g	Gravitational constant $[m/s^2]$
T	Regular wave period $[s]$

1 Introduction

According to the US Energy Information Administration, global energy consumption is expected to increase by almost 50% by 2050 (US Energy Information Administration 2022). Energy production and consumption can be divided into three main purposes: electricity, heat, and transportation (Our World In Data 2022). Energy consumption increasements are results of growing human populations and an increase in human welfare. These factors drive the demand for energy, goods, and services, which needs to be met.

Today, 63.3% of the global electricity amount consumed is produced through fossil fuel sources. These are energy sources like coal, natural gas, and petroleum variants. Fossil fuels for electricity production takes a toll on the environment by the release of climate gases into the atmosphere upon combustion. However, despite there existing large fossil reservoirs underground that are already known of and more being found each year, these energy sources will not last forever. They exist in finite quantities in the earth's crust, constrained in mass and volume by the mechanism of their creation (Moore 2022).

It is necessary to constrain the amount of unnatural releases of climate gases into the atmosphere in order to slow down man made climate change. Relying too much on energy sources that will eventually run out is not sustainable. Therefore, a shift towards green and renewable energy sources is needed. These greener alternatives are energy sources where the forces of nature are utilized in a way that does not heavily rely on the combustion of a fuel. Thus, they do not affect the environment as much as fossil based energy sources during their operation time. Important examples are wind based, solar based, and geothermal based energy sources.

Over the last couple of years, a surge in investments has been seen in the offshore wind industry (Buljan 2022). This may indicate future trends of implementing renewable energy sources offshore, instead of on land. At the same time, the technology behind photo-voltaics (PV) is maturing with developments in semi-conductor technology. Over the past decade there has been increased interest in inshore floating photo-voltaic (FPV) installations (Trapani and Santafé 2015). And over the last couple of years, industrial and academic efforts have been made researching the concept of placing FPV installations offshore.

This thesis will revolve around a relatively new (it has been a research topic among for about 4 years) concept for a floating island meant to be the foundation for which photovoltaics can rest on as a complete offshore FPV installation. The concept was suggested as a research topic by Trygve Kristiansen (Winsvold 2018). This concept can be described as a multi-torus structure, meaning the buoyancy providing foundation is in the form of five concentric, flexible toruses, all with equal cross-sectional diameters. The toruses are connected by trusses in eight radial directions, all being equally spaced, meaning there is 45 degrees between each truss between two toruses. A visualization of what the multi-torus structure would look like is pictured in Figure 1.1.

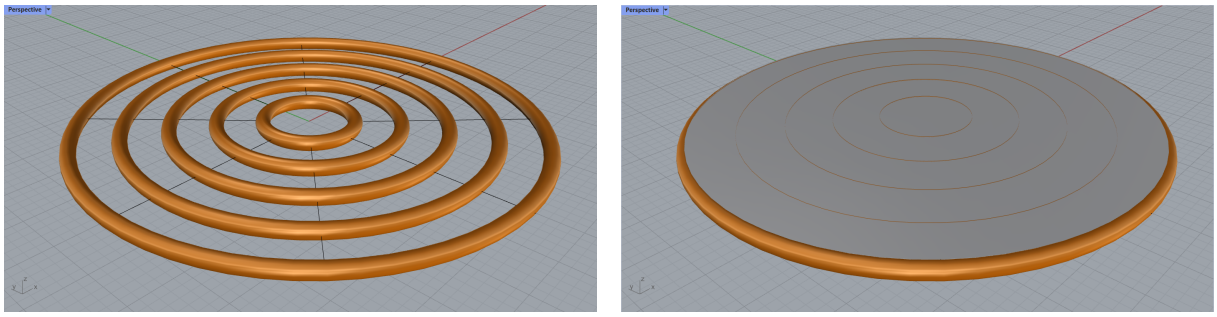

Figure 1.1: Full scale multi-torus structure with and without solar deck. The deck is here shown as a smooth surface but would in reality be in the form of a well-draining membrane-deck covered with solar panels. The global diameter of the outermost torus is envisioned to be 50 m, and the cross sectional diameters of all toruses are envisioned to be 1.6 m.

This thesis will propose a method to control the motion of the solar cell panel carrying deck of this structure. This is done by controlling the tension in the deck carrying the solar panels. The desired tension level is based on mathematical models for the deck and the incoming wave frequencies, giving an opportunity to assess the likelihood of resonant vibrations in the solar deck. The incoming wave frequencies are estimated in real-time by computing the discrete Fourier transform (DFT) on the structure wave response in heave. Since the structure is meant to follow the waves in heave, this will give reliable estimations of the dominating wave frequencies in the present sea state.

During the process of making and writing the project thesis and the present thesis, there were discussions on the practical limitations to the layout of the multi-torus concept. One such topic of discussion has been the idea of the deck resting on top of the toruses while also having sufficient slack to also touch the water surface in between the toruses. This implies significant steepness in parts of the deck. Steepness and inclination and declination of PV panels could have both a positive and negative impact on the density of incoming solar radiation. At the same time, it could also cause shadows on areas of the installment, which is not desired. Therefore it could be argued that if several toruses are involved like in the multi-torus concept, the solar panel carrying deck should be elevated off from the water. Otherwise, it would have been a better solution to only have one torus with the deck resting on the water surface in the middle of the single torus, much like in the Ocean Sun concept, mentioned in Section 1.1.

The multi-torus concept is still in a developing research phase. Therefore, the layout of the solar plant is not firmly decided or known. This means that certain layouts of the multi-torus concept can be studied in an evolutionary process in optimizing the design. So in this thesis, it is envisaged that the deck rests freely in between the toruses, not touching water.

1.1 Background

PV power production installations take up large land areas. With increasing centralization and expanding cities, this can lead to conflicts regarding land area usage. So instead of

installing photovoltaic plants on land, a reasonable alternative is placing them on water.

It was first proposed to move solar installations to inshore ponds or lakes (Trapani and Santafé 2015). Many inshore FPV installations already exist, as shown in Figure 1.2. Here the solar installations not only provide power for nearby human settlements, but they can also reduce evaporation from the ponds or lakes by absorbing the heat radiation. This is helpful when considering that fresh water might become scarce in the future Tom Smedley 2021. At the same time, the effect of water cooling on the solar cells increases their electrical efficiency, as is also mentioned in Trapani and Santafé 2015, and observed in Trapani and Millar 2014.

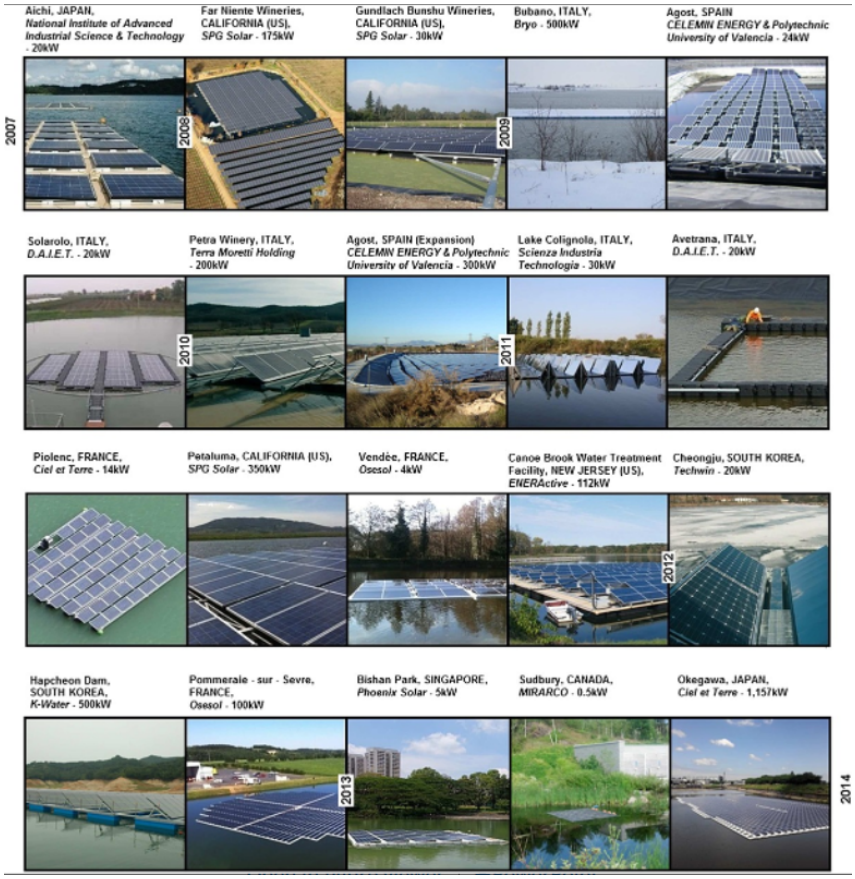

Figure 1.2: A selection of inshore pond FPV project concepts from 2007 to 2013. Offshore FPVs have to a large extent gained traction in the years after this article was composed (not as a result). Photo courtesy of K. Trapani and M. R. Santafe from Trapani and Santafé 2015.

Recently it has been proposed to further expand on the idea of floating photovoltaic concepts. This involves installing FPV installations offshore instead of in inshore lakes. While offshore, solar islands can produce electricity for existing offshore installations, but they might also be used for synthetic fuel production. This topic is treated in Patterson et al. 2019, which is a proposal for a synthetic fuel production offshore island. Here, methanol production is proposed through recycling carbon dioxide CO_2 and electrolytic production of hydrogen gas H_2 from sea water. Although there are big electrochemical challenges related to these processes, the idea is for the catalytic reaction between these

two components to form methanol. Hydrogen gas as direct fuel for offshore vessels and land based vehicles has also gained traction over the last years, and synthetic fuel production and consumption are emerging as markets and fields of research.

Wave loads on a floating solar island installation will be greater offshore than inshore. To deal with these conditions, offshore solar floating islands must be robust. There are some examples of commercial FPV concepts where the seakeeping capabilities are in focus. These are either in project phases, or have already been implemented at sea. Two promising Norwegian examples are Ocean Sun's membrane concept, and Equinor and Moss Maritime's multi module concept.

Figure 1.3: Ocean Sun AS concept (left), and Equinor and Moss Maritime concept (right). The Ocean Sun illustration shows the idea and design of the solar island. The Equinor and Moss Maritime concept illustration shows roughly what the concept could look like at an offshore location. Photo courtesy of Ocean Sun and Equinor and Moss Maritime from Ocean Sun 2021 and Equinor 2021

Ocean Sun's concept is shaped as one flexible buoyancy torus with a thin membrane in it's interior, where the membrane rests on the sea surface (Ocean Sun 2021). The solar panels are mounted on the membrane. This concept has been installed on many sites, among them the Banja reservoir in Albania, where power production commenced in 2021. Unfortunately, due to a storm this installation was destroyed short after (Hovland 2021). However, the rig was up and running again in the spring of 2022 (Garanovic 2022). The Equinor and Moss Maritime concept is more rigid. It is a modular concept where an arbitrary amount of identical and rectangular modules can be connected together to form a larger floating island (Equinor 2021). The modules are interconnected by a patented joint-technology that only allows rotations. Additionally, this concept aims to be as cheap as possible, as the designers aim to use components already available in the industry (Onsrud 2019). In 2021, it was announced that they will be testing the seakeeping capabilities of the concept in offshore conditions outside the Norwegian island of Frøya. Both of these mentioned concepts appear promising.

In the multi-torus structure, the solar panels will be suspended in mid-air in between the toruses, unlike in Ocean Sun's concept, where the solar panels are resting on the membrane on the water surface. As can be seen from Figure 1.3 in the Ocean Sun concept, there is a need for a pump that can pump out water from overtopping waves or rainwater. This is due to the bowl-shape of the concept. For the multi-torus concept envisioned in this thesis, the solar deck membrane is elevated off from the water surface with about 1m. This

removes the need for accumulated water to be pumped away from the structure, given that the deck is well draining.

The idea behind the multi-torus structure originally arises from the results from Borvik 2017. Here, a floating solar island foundation was proposed in the shape of a single torus with a disc-shaped air cushion inside the floating torus. The air-cushion was proposed as the bearing mechanism for the PV panels. A small-scale model was built and tested. However, the results from this study resulted in the author recommending finding an alternative for the air cushion. As a result, it was proposed by their supervisor for the next master's thesis to replace the air cushion with several, smaller toruses for supporting a solar panel deck.

This resulted in the work of Winsvold 2018, which is discussed later in Section 1.3. It is proposed that the full scale multi-torus structure has toruses with cross sectional diameters of 1.6 m. The global diameter of each torus varies (with increments of 10 meters) from 10 meters for the innermost torus to 50 meters for the outermost torus. Hence, there are in total 5 toruses. This makes the outermost torus in the multi-torus structure the same size as the circular floater in many fish farms today. It is assumed that the global diameters describes the distance for the cross-sectional center point. Between the toruses, in eight radial directions, are trusses with given stiffnesses. These trusses help the structure hold the intended shape and position when exposed to the environmental loads.

1.1.1 Other offshore FPV concepts

The FPV concepts of Ocean Sun, and Equinor and Moss Maritime are not the only FPV concepts in existence. There are several offshore FPV concepts from other countries in Europe, and in Vo et al. 2021, some of these are reviewed. One promising project is the Zon-op-Zee (Sun-at-Sea) project in the Netherlands, where six dutch companies have cooperated in the making of the concept. The pilot installation, North Sea 1, was installed in 2019 by the dutch company Oceans of Energy (Oceans-Of-Energy 2022). This project is claimed to be the first offshore FPV installation at open sea in the world, having survived some of the recent North Sea storms with up to 13 m high waves. The concept relies on foam-backing under the solar panels, and additional floaters for buoyancy.

Other FPV projects from Europe include two concepts from Austria. One is still only a concept, but it has been tested in wave maker tanks. This first concept is called Helio-Float, and was conceptualized by a team from the Technical University of Wien (Technical-University-Wien 2022). This concept is a rigid platform with a special foundation where buoyancy is provided by vertical axis round cylinders with a closed top, but an open bottom. This creates a pocket of compressed air functioning as a shock absorber, and making the structure motion to some degree decoupled from the wave motion in heave. The other Austrian concept is made by an Austrian company called Swimsol. This company specializes in FPV installations in tropical waters for local electrical power consumption in for example the Maldives and Indonesia. The FPV rigs are installed in shallow water, often in shielded areas of sea, meaning that extreme weather conditions may not be affecting their structures (Swimsol 2022). The Swimsol installations are similar to the Heliofloat,

and Equinor and Moss Maritime concepts, in that they consist of several rigid modules that are interconnected.

The concepts mentioned above are far from all the FPV concepts that exist. The fact that many FPV concepts exist is good for the FPV market. Competition drives down the costs, and a diversified spectrum of concepts lead to optimal designs. It also demonstrates the developments and investments in FPV markets that may be seen in the coming decades. However, with emerging and expanding markets there is an underlying risk of the markets being overvalued. This is important to consider with many of these companies not generating profits as of yet, like for example the previously mentioned Ocean Sun company (OceanSun 2022, p. 18). Levelized Cost of Energy (LCOE) is therefore an important metric for these projects. LCOE is defined as the total economic cost per energy unit produced over the project lifetime (ScienceDirect 2022). With competition in the markets and sufficient research and development, it may be possible to reduce the LCOE to levels where profits are generated.

1.2 Motivation and simplification

The multi-torus structure is a structure consisting of 5 concentric toruses. All the toruses have similar cross sections and cross section diameters, but they have different global diameters. Although it is envisioned for the structure to consist of 5 toruses, it could prove to be a more optimal design with either more or fewer toruses. This would have to be seen in relation to the weather and environment conditions at planned location.

The solar panel carrying deck is meant to be stretched over the toruses, leaving the solar panels suspended in mid-air in between the toruses. The deck must drain water well in order to prevent water accumulation on top of the structure. Therefore, the deck can be pictured as a net laid over the toruses over the area enclosed in the outermost torus. Additionally, other solar panel carrying mechanisms working in tandem with the net could be needed. These could be pictured as wires in a spider-web-like manner over the toruses. The wires would carry a portion of the load from the solar panels, adding some redundancy in the structural integrity of the deck as a whole.

The multi-torus concept has been described by the creator, prof. Trygve Kristiansen, as being prone to resonant swinging motion in the solar deck, due to the solar deck being suspended in mid-air. The inertia of the solar panel loaded deck could potentially result in vibrations and even snapping loads when moving with the multi-torus structure in heave. Another reason for the proneness to resonant swinging motion is due to the flexibility of the toruses and the deck itself.

So the problem of avoiding resonant swinging motion and other jerky movements of the solar deck is to be treated in this thesis. It is not known if this actually will pose a severe threat to the structure in full scale, but it is believed to be a problem. So solutions lay in good designs of the solar deck and possibly motion control systems. In this thesis, the solution is envisioned as a motion control system incorporating winches that pull on parts of the solar island. Pulling on certain points within the structure alters the stiffness

throughout the already flexible system, leading to changes in the natural frequency of the structure. In this thesis, this is envisioned to be achieved through the use of winching action on the solar panel carrying deck. This is treated later in Section 3.

It is difficult and would require extensive global control implementations to control the tension between the toruses for a multi-torus structure. Therefore, this thesis will focus on a cross-sectional simplification of the multi-torus structure. The effect on the structure eigenfrequencies by introducing more or less tension into the system is thus reduced to a 2D problem. Considering a 2D problem also makes it easier to assess the efficiency of the control methods. A visualization of the 2D problem reduction and how the layout of the physical model studied in this thesis is acquired, is shown in Figure 1.4.

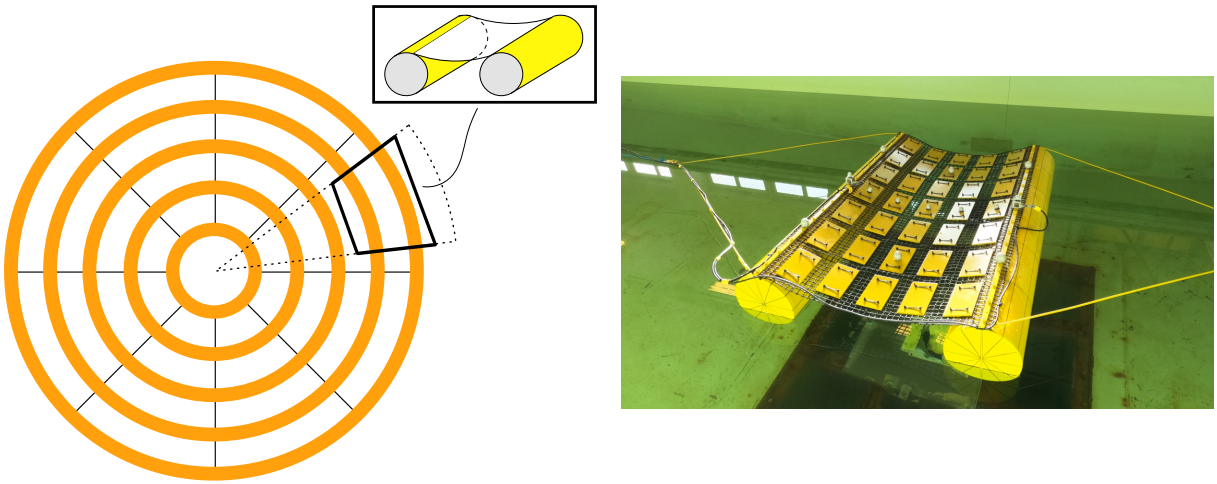

Figure 1.4: Illustration of how the problem and structure is reduced from 3d to 2d, with the resulting model that was tested. This thesis focuses on how control of the pretension in the solar deck affects the eigenfrequency of the deck.

Although it is not part of the scope of this thesis, it is of interest to mention that it is assumed that the solar panels are crystalline and rigid in the multi-torus concept in this thesis. However, the technology behind flexible solar panels is maturing (US Office Of Energy Efficiency 2022). It would be interesting to analyse how a multi-torus installation utilizing flexible solar panels would behave, and if this behaviour would be different than when using rigid solar panels. It would still be necessary to make a good design for the deck and PV panel interface, to allow good drainage for offshore applications.

Trapani and Millar 2014 presents the thin film flexible floating PV (T3F-PV) array concept. This concept is also mentioned in Trapani and Santafé 2015, written by the same author. A prototype is built and tested out in a small pond in Sudbury, Canada over the duration of one and a half month. There is an estimated 0.5% decrease in electrical efficiency, largely because of sediment accumulation of top of the panels. From another 3 day comparison test period, the FPV concept showed a 5% improvement compared to a reference air cooled solar array installation. Also, increased efficiency was discovered when the array was allowed to be submerged to the point where the solar panels were just below the water surface. As mentioned, Yin et al. 2021 also revolves around flexible solar panels. The material used here is a polymer solar cell (PSC).

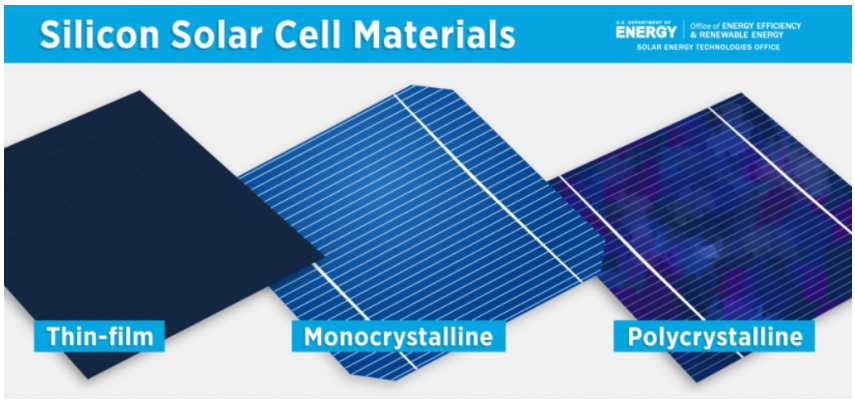

Figure 1.5: Types of solar cell materials. The thin-film type could be fitting for usage on water, both offshore and inshore. Photo courtesy of US Office Of Energy Efficiency, from US Office Of Energy Efficiency 2022

1.3 Existing literature on related topics

This thesis involves many topics, so literature from several branches of marine technology can be useful. The following are synopses of previous research on the multi-torus solar island itself and modelling, and sea state estimation.

1.3.1 Multi-torus literature

There are four students from the Institute of Marine Technology (IMT) who have written their master's thesis about the multi-torus concept before.

Winsvold 2018 continues the work by Borvik 2017, and studies the multi-torus concept as an alternative to the air cushion. A 1:50 scale multi-torus model is made, corresponding to the size of the envisioned full scale dimensions of 50 m global diameter. This small scale model is tested in regular and irregular waves, for setups where five toruses are present and one torus is present. Only the toruses are tested, so a membrane deck is not included for neither of the model setups. For the case of five toruses, these are connected to each other using pre-tensioned elastic rubber bands, similar to a regular hair tie. The results from the two test setups are compared to results obtained respectively from a low-frequency linear slender bodied theory from Li 2017, and Zero Frequency Theory (ZFT) from Odd M. Faltinsen 2011. The single torus test showed good agreement with the theory, while the five toruses showed good agreement with theory for very long waves. However, the multi-torus setup did not result in motion amplitudes as large as for the single torus theory and model test. This was expected as a result of the truss and mooring interaction on the toruses. The main concern and problem with the experimental implementation was identified as waves overtopping over the toruses. It was concluded that the multi-torus concept shows potential, but needs more research and work.

Sigstad 2019 improves on the work done by Winsvold 2018 by optimizing the small scale multi-torus model. The elastic bands are replaced with stiffer bands, and a membrane deck is included on top of the model. Small masses are placed on top of the deck, representing the solar panel load. The results from physical model testing were also compared to

results obtained through numerical analyses. The numerical solver is verified and well functioning on simple systems with known dynamics. However, for the coupled truss and floater system, the solver has a unresolved bug causing the results to become non-physical. According to the model constructing team, overtopping waves resulted in small ponds of water on the solar panel bearing membrane. This was due to the membrane not being permeable enough for the scale. Because of this, a permeable deck was chosen for the model tested in this thesis. It is mentioned briefly that curiosity is associated with the pretension on the solar deck, concerning the eigenfrequencies of the deck. This is what will be treated in depth in this thesis, with the added element of controlling this eigenfrequency.

The overtopping waves in Sigstad 2019 was carried in mind while designing the model for the present thesis. Trygve Kristiansen also suggested having a deck that could drain water well. So the choice of solar deck landed on a rough meshed net, with quite low ability to absorb water in the threads themselves.

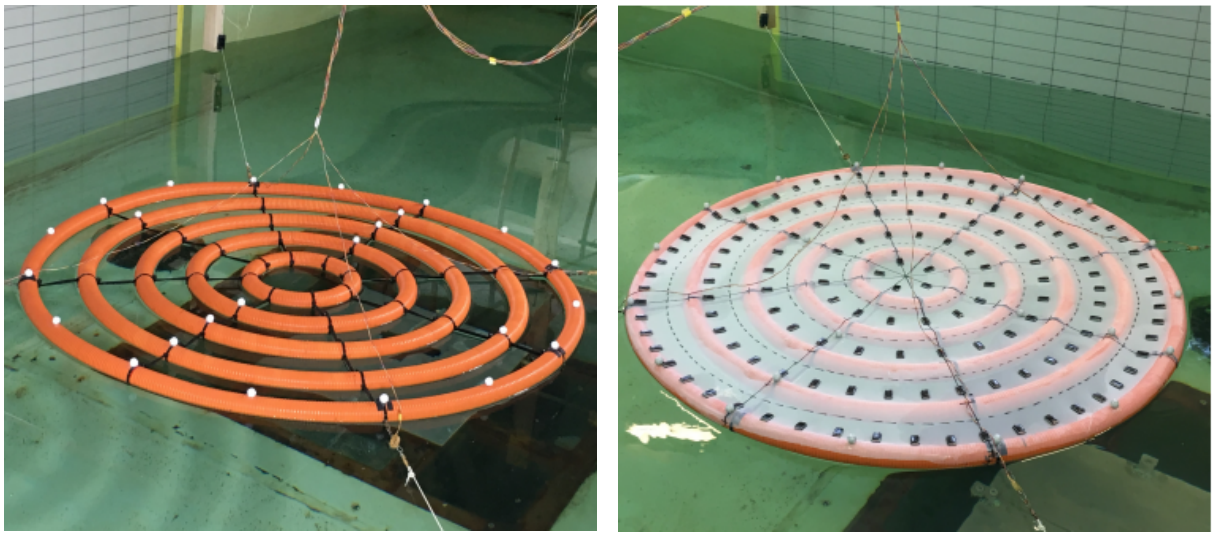

Figure 1.6: Multi-torus 1:50 model scale, with and without a solar deck. Photo courtesy of Mari Vassdokken Sigstad from Sigstad 2019

Tolaas 2020 and Olsen 2020 are works done in collaboration. They present numerical and theoretical studies on the hydrodynamical coupling and the structural coupling through the trusses between the toruses. A numerical integration scheme is implemented in MATLAB. The resulting vertical mode Response Amplitude Operators (RAOs) appear to follow the ZFT closely. A main goal of the studies was to figure out if irregularities seen in the RAOs of Winsvold 2018 and Sigstad 2019 was due to structural interactions between the toruses through the elastic bands holding them together. It is concluded that both hydrodynamic and structural interaction between the toruses can affect the behaviour of the multi-torus concept. The numerical models are found to contain small errors, but it is concluded that they are still good representation of the real system and robust frameworks for further numerical studies. The truss model, which is also presented and used in Sigstad 2019, is believed to be applicable also to a 2D consideration of the solar deck hanging in mid-air between the toruses. However, this truss model was not implemented in this thesis.

1.3.2 Sea state estimation

There will also be implemented a wave estimator in this thesis. This will be done with the Qualisys motion capture facilities available in the laboratories. Estimating the frequency of the waves is necessary for giving an input to the controller. Depending on the incoming waves and the current tension level, the controller will command the desired tension in the solar deck between the cylinders.

Brodtkorb, Nielsen and Sørensen 2015 estimates the sea state using motion measurements from a small scale model ship. A signal based sea state estimation algorithm is presented based on the Fourier transform of the motion measurements, and is verified in the lab. Brodtkorb, Nielsen and Sørensen 2018 also uses online vessel measurements to estimate wave frequencies. This is similar to what is to be done in this thesis. This method of acquiring a sea state does not rely on Response Amplitude Operators (RAO) for the model. In this article, the object for which the sea state is estimated is a rigid body. In this thesis, the body used for estimating the wave frequencies is not completely rigid. The multi-torus structure is rather supposed to follow the waves in heave, so by definition it should be possible to use the structure for estimating the dominating frequency of a sea state.

Fossen 2021 (p. 397) also states that the Fast Fourier Transform (FFT) can be used in order to estimate the wave frequency. It also contains some observer designs for wave estimation. It states that the FFT algorithm takes time to execute, leading to the data arrived at from the algorithm being outdated. However, Fossen states that for controlling states that slowly vary over time, roughly 30 minutes, it is feasible to use this approach. This is what is envisioned in the control system for the full scale multi-torus concept. The sea state is varying slowly, so a lagging algorithm is acceptable for the purpose of controlling the momentary response of the multi-torus structure based on the general sea state it experiences.

Ren et al. 2021 additionally states that a wave spectrum can be directly measured by means of video measurements, satellites, unmanned aerial vehicles (UAV), and weather balloons. This way, an overview of the sea state in a larger ocean area can be estimated. These direct measurement methods include long communication delays, and make them unfit for active control. However, it is suitable for a semi-active control approach as is envisioned in this thesis. Direct measurement is therefore an alternative to using the multi-torus structure as a wave estimator.

1.4 Contribution

This thesis explores a novel non-commercialized FPV plant concept, shaped like multiple concentric toruses. It presents simple methods to model the static and dynamic behaviour of a 2D simplification of a freely hanging deck supporting the load of PV panels and equipment in this concept. This solar deck layout is not similar to many other FPV concepts where the PV backing rests on the sea surface. A model representing a 2D simplification of the multi-torus structure is built and tested, and test results are presented for the case where a solar panel load is present. The solar deck used in the tests is very

permeable, as was noted to be an advantage from previous studies, and it is not very elastic. This leads to increased understanding of the behaviour of a weighted membrane suspended in mid-air between two floating elements.

1.5 Objective and scope

Some research already exists on the multi-torus concept as seen in Section 1.3. These previous studies have mostly focused on the hydroelastic response and global analyses. This thesis will focus on the effect of pretension on the resonant vibrations in the solar deck motion in regular waves. Because resonant swinging and vibration occurs for discrete frequencies, regular waves will be the main topic studied in this thesis. A real-time wave frequency estimation algorithm based on the Fast Fourier transform is proposed for estimating the frequency of the sea state as window-based input to a semi-active controller. The controller being semi-active is in this regard meant as the controller not continuously commanding new tension levels. The main objectives can be summarized as in the following.

1. Present literature and synopses that are relevant to the study, including general FPV, multi-torus, sea-state estimation, and winch control literature.

2. Perform a modelling study for the purpose of introducing control for the multi-torus structure in a 2D problem. Estimate the static solar deck configuration and natural frequency, and elaborate on the estimates in a higher-fidelity model study, which is done in Matlab.

3. From the modelling study, propose a control scheme for the multi-torus and assess the feasibility of efficiently using winches as actuators to perform control action on the structure.

4. Design and build a small scale model in an appropriate scale for solar deck vibrations to be measurable. Perform experimental studies on the 2D model, aimed at producing resonant motions in the solar deck and estimating the wave frequency. Compare the theoretically obtained natural frequencies of the solar deck with the experimentally observed ones.

1.6 Thesis outline

Section 1 presents background information on FPV concepts that exist, and introduces the simplifications and assumptions further used in this thesis.

Section 2 includes the theory used for control purposes, including methods to model the solar deck behaviour in waves.

Section 3 revolves around proposing an efficient control scheme for the solar island, using winches and tensioned cables.

Section 4 presents the small scale model, and the model setup in during testing.

Section 5 presents the experimental results from the model tests, and the theoretical results from the solar deck behaviour.

Section 6 discusses the findings in the result section.

Section 7 summarizes the work done in the thesis, and concludes on the results obtained. Future work is also suggested.

Appendix A presents how the model was made.

Appendix B revolves around the model breaking and how it was fixed.

Appendix C Presents the discussion on the feasibility of including an actuator for automatically changing the tension in the solar deck in real time during testing.

Appendix D presents the resulting FFT frequency spectrum plots produced during the regular wave model testing.

2 Theory

2.1 Static configuration of 2D solar deck suspended in mid air

The solar deck can be regarded as a membrane with little to no bending stiffness which is hanging freely with two opposing sides being fixed to the floaters, while the two other sides are free. Since this membrane is rectangular, it can be regarded as a 2D freely hanging member. A freely hanging member with evenly linearly distributed mass and negligible bending stiffness takes the form of a catenary. The catenary equation is given in Equation 2.1, from Weisstein 2021.

$$y(x) = a \cdot cosh(\frac{x}{a}) \tag{2.1}$$

Here, a is some constant, x is the input to the function, and cosh is the hyperbolic cosine function. This is one possible representation for the solar deck. The catenary equation is obtained by assuming that the vertical gravity force is distributed along the catenary axis and depends on the inclination of the catenary at a certain point. A simplified representation relies on the assumption that the load working on the freely hanging member is evenly distributed along it's horizontal projection. This results in a parabolic shape of the member, as shown in Figure 2.1.

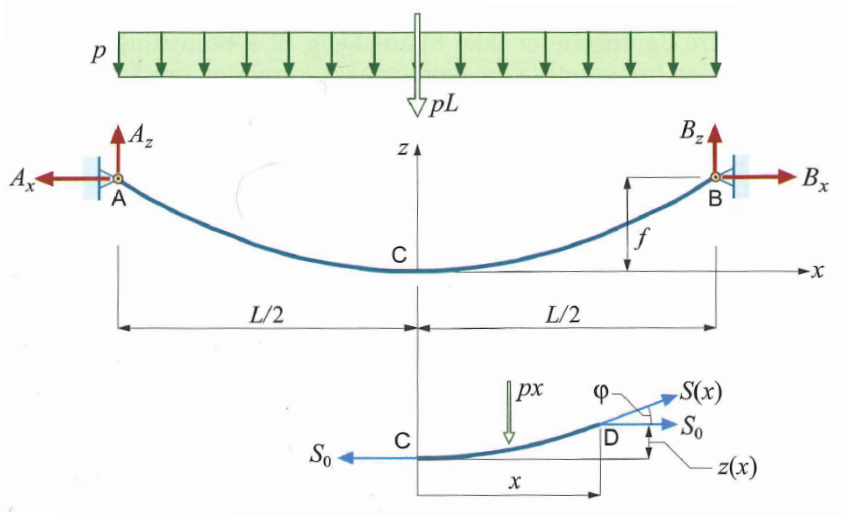

Figure 2.1: Mechanical representation of a symmetrical parabola line. Photo courtesy of Kolbein Bell from Bell 2014.

The error involved with using a parabolic shape diminishes when the sag is small. Since the sag is in order one tenth of the span length for the solar deck in this thesis, the error is also quite small. From Bell 2014, when the sag is less than one fifth of the span length, the error made with the parabola simplification is less than 5%.

The function for the parabola shown in Figure 2.1 from Bell 2014 can be found by considering a static force and moment equilibrium, which yields Equation 2.2.

$$z(x) = -\frac{A_z}{A_x}x + \frac{p}{2A_x}x^2 \tag{2.2}$$

Here, A_z and A_x are the response forces at the left fixation of the parabola line, while p is the distributed load on the parabola line. The variable x runs from the lowest point of the parabola. It can be shown that the connection between the horizontal force in the member and the sag of a symmetric parabola line, is given by Equation 2.3.

$$S_0 = A_x = B_x = \frac{pL^2}{8f} \tag{2.3}$$

Where S_0 is the horizontal force at the lowest point in the parabola, L is the distance between the two fixed points, and f is the sag from the bottom of the parabola line up to the height of the two fixed end points. A_x and B_x are still as in Equation 2.2, and can also be regarded as inputs resulting in a desired sag. This equation was used extensively for deciding dimensions and the draft of the floaters in the physical model.

2.2 Vibration of solar deck in 2D

The main goal of the solar deck modelling is to accurately describe the eigenfrequency of the deck. The controller estimating the frequency of the waves needs to compare the wave frequency to the eigenfrequency of the deck, in order to give commands to the actuators that, in the case for resonance being likely, can change the eigenfrequency of the deck. Desired deck models are therefore models that yields and directly calculates the eigenfrequency of some member that represents the solar deck. Since there is no simple way to assess vibration on a catenary or parabola shape, a next step is to assess the vibration of a tensioned member in 2D. For beam and string vibration, the tension T is needed to create a mapping between the tension T and the eigenfrequency ω_0.

The first mode vibration, as shown in Figure 2.2 as n=1, is the main cause for concern, as this allows for the largest motion amplitudes and accelerations, which is not good for the structural integrity of the equipment on the solar deck and the solar deck itself. First mode vibration is also assumed to be the dominating type of vibration for the solar deck. This makes the measurements at the middle of the solar deck the most important ones in the model tests.

2.2.1 String and beam with tension

From Bachynski et al. 2019, the eigenmodes for a vibrating string with no bending stiffness, and for a tensioned beam that is simply supported in both ends are given by Equation 2.4.

$$\phi(x) = \phi_0 \cdot sin(\frac{n\pi}{L}x)\,, \qquad n = 1, 2, 3, ... \tag{2.4}$$

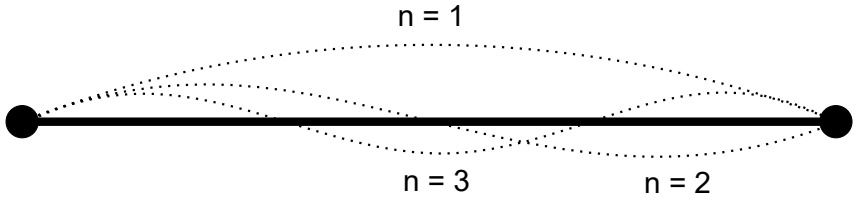

Figure 2.2: The first three modes of string vibration. The first mode is the mode of most concern for the solar deck in the multi-torus concept.

Here, ϕ_0 is the amplitude of the vibration mode, l is the length of the string, and n is the mode number as in Figure 2.2. Lastly, x is the running variable from one end of the string to the other. For a string, each mode shape has an eigenfrequency given by Equation 2.5.

$$\omega_{s,n} = \frac{n\pi}{L}\sqrt{\frac{T}{m}}\,, \qquad n = 1, 2, 3, ... \tag{2.5}$$

Here, n and L is as in Equation 2.4. T is the tension in the string, and m is the linear mass per unit length of the string. Although the solar deck has a small bending stiffness, it is not zero. Therefore, an assessment of the bending stiffness contribution to the eigenfrequency is considered in the following. For a tensioned beam with uniform stiffness over the length, each mode shape corresponding to Equation 2.4, has an eigenfrequency given by Equation 2.6.

$$\omega_{b,n} = \frac{n^2\pi^2}{L^2}\sqrt{\frac{EI}{m}}\,, \qquad n = 1, 2, 3, ... \tag{2.6}$$

Here, n, L, and m is as in Equation 2.5, and EI is the bending stiffness of the beam. The eigenfrequency of a beam with axial tension is then given as in Equation 2.7.

$$\omega_{bs,n} = \sqrt{\frac{k_{tot}}{m}} = \sqrt{\frac{k_s + k_b}{m}} = \sqrt{\omega_s^2 + \omega_b^2} = \sqrt{\frac{n^2\pi^2}{L^2}\cdot\frac{T}{m} + \frac{n^4\pi^4}{L^4}\cdot\frac{EI}{m}}$$

$$= \frac{n\pi}{L}\sqrt{\frac{T}{m} + \frac{n^2\pi^2}{L^2}\cdot\frac{EI}{m}} \tag{2.7}$$

As all the terms inside the square root in Equation 2.7 are positive, it can be deduced that the natural frequency of the beam with tension is greater than or equal to the natural frequency of just the string from Equation 2.5, illustrated by the following inequality.

$$\omega_{beam\ with\ tension} \geq \omega_{string} \tag{2.8}$$

This means that adding a tensioned beam contribution to the continuous system increases the natural frequency, as can be seen from Equation 2.7. This is also known from the

general natural frequency equation with the square root of the general stiffness k over the general mass, meaning that a higher general stiffness increases the natural frequency.

During the model tests to be executed, the goal is to produce resonant vibrations in the solar deck. If the solar deck has a very high natural frequency, as anticipated by Equation 2.7 if the bending stiffness is large, it could be difficult to produce resonant vibrations in the solar deck. This is because there are constraints on the velocity and stroke length of the cylinders producing the wave motion. For wave frequencies equal to the natural frequency of the solar deck, unwanted and nonlinear wave effects could occur. This was observed for regular waves with period 0.3 s and height 0.01 m, as transverse sloshing in the direction normal to the wave direction, as seen in Figure 4.7. Modelling the solar deck with some bending stiffness is therefore not beneficial for the accuracy of the mathematical model of the deck.

The continuous string and tensioned beam equations have an underlying assumption that there is no sag in the member. However, this is in reality not possible for a loaded member with no bending stiffness fixed at the ends. As can be seen from the simplified parabola theory in Equation 2.3, a sag tending to zero implies an infinitely large horizontal force at the fixed ends. This is unphysical, so the applicability of the continuous string and tensioned beam equations on the relatively heavy solar deck in this thesis is a topic for discussion. In the model tests, the solar deck does not always have the tension needed for the sag to be small enough that the string and tensioned beam equations are good representations of the solar deck, which is why other approaches to assessing the natural frequency of the solar deck is necessary.

2.2.2 Discrete mass and spring system approach

From the author's knowledge and findings, not a lot of research has been done regarding resonant vibrations of freely hanging members. This means that simple estimates should be employed for this modelling approach. As shown in Figure 2.3, the solar deck can be discretized into six springs with five masses in between them. Five point masses is chosen because of the physical model having five masses along the 2D length of the member. The masses in the physical model are plates, so they are not point masses, but it is assumed that point masses are sufficient to describe the general dynamic behaviour. Also, modelling the member as springs in between the masses implies that there is some elasticity in the solar deck. Whether this is a reasonable assumption is a topic for discussion.

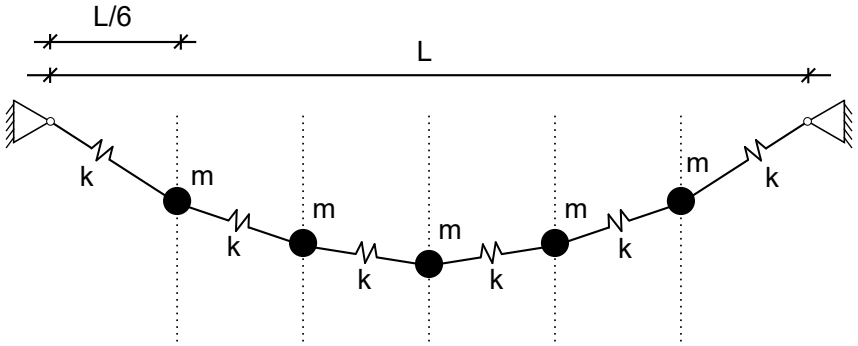

Figure 2.3: Discrete mass system consisting of five point masses that are restricted in horizontal direction, but free to move in vertical direction. In between them are springs with stiffnesses k. The length L is the length between the two end points of the hanging member. Hence, L/6 becomes the horizontal length between each point mass.

This 2D system with five degrees of freedom (dofs) can be reduced to a one-dimensional system with three dofs as shown in Figure 2.4.

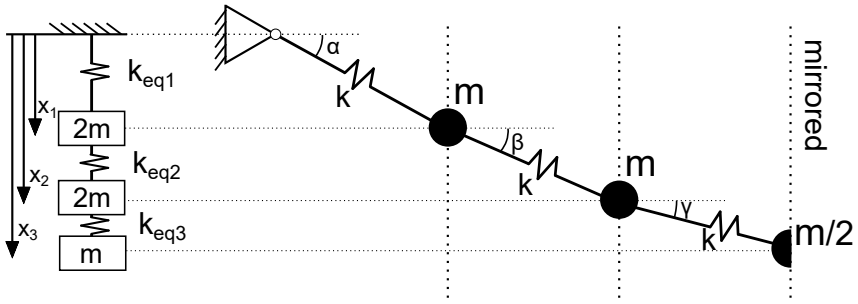

Figure 2.4: The 2D five dofs system reduced to a 1D three dofs system, assuming a symmetric behaviour of the freely hanging member. The point masses have a mass m, the springs have stiffnesses k, so that the vertical equivalent stiffnesses become $k_{eq,i}$. The springs have an declination to the horizontal in static equilibrium of α, β, and γ.

From this, the equivalent vertical stiffnesses k_{eq1}, k_{eq2}, and k_{eq3} must be found. The angle each spring in the original setup has with the horizontal is denoted as α, β, and γ, respectively. From a decomposition of the force in each spring, a vertical stiffness component can be found as in Equation 2.9, here for the leftmost spring.

$$F_v = 2 \cdot F \cdot sin(\alpha) = 2 \cdot k \cdot x \cdot sin(\alpha) = k_{eq1} \cdot x$$
$$\implies k_{eq1} = 2 \cdot k \cdot sin(\alpha) \tag{2.9}$$

Where F_v is the vertical component of the force F through the spring at an elongation x along the spring. The masses in the one-dimensional problem to the left in Figure 2.4 become the total mass of the mirrored system, meaning 2m for the two upper masses, and m for the lowermost mass.

Determining the angles, a static equilibrium case must be considered. The two opposing springs on each side of the symmetry line is considered to carry the total mass below the respective two springs, so that the first two springs carry a mass of 5m, the second two springs carry 3m, and the last two springs carry m. Since the masses are restricted in horizontal direction, the vertical spring forces can be assessed independent of each other.

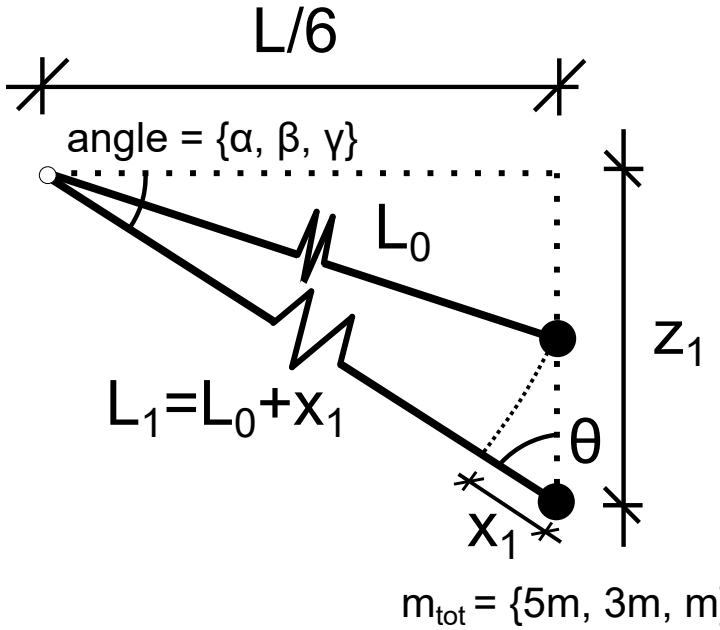

Figure 2.5: The static angle of the three mass cases m = m, 3m, and 5m which gives an elongation x_i along the spring. The elongation of each spring, here denoted x_1 leads to a force F_1 in the spring for each of the three mass-cases.

The idea with this is to find the angle with the vertical line θ so that the corresponding angles with the horizontal line, α, β, and γ, can be found. L/6 is the horizontal fixed length between the masses, and L_0 is the length each spring has when there is no force through the spring. L_1 then becomes the total length of the spring at static equilibrium. L_0 and L_1 are therefore given, and do not need to be found expressions for. z_1 is the vertical distance between the top and bottom of the string in vertical equilibrium. From Figure 2.5, it can be seen that the relation in Equation 2.10 holds.

$$cos(\theta) = \frac{z_1}{L_1} = \frac{z_1}{L_0 + x_1} \tag{2.10}$$

Furthermore, from a static force equilibrium in vertical direction, the following result in Equation 2.11 can be obtained.

$$2 \cdot F_1 \cdot cos(\theta) = 2 \cdot k \cdot x_1 \cdot cos(\theta) = m_i \cdot g \tag{2.11}$$

Here, F_1 is the force through the spring at static equilibrium. An additional geometric observation must be found, as in Equation 2.12.

$$\begin{aligned} (L/6)^2 + z_1^2 &= (L_0 + x_1)^2 \\ \implies z_1 &= \sqrt{(L_0 + x_1)^2 - (L/6)^2} \end{aligned} \tag{2.12}$$

Combining Equation 2.10, Equation 2.11, and Equation 2.12, the following relation can be obtained in Equation 2.13.

$$2 \cdot k \cdot x_1 \cdot \frac{\sqrt{(L_0 + x_1)^2 - (L/6)^2}}{L_0 + x_1} L_0 + x_1 = m_i \cdot g \tag{2.13}$$

Squaring Equation 2.13, it can be seen that the equation is a polynomial of fourth degree in x_1, which should be solved numerically using Matlab. When x_1 has been found, it can be inserted into Equation 2.12 to find z_1, and then x_1 and z_1 can be inserted into Equation 2.10, to find the angle θ, so that each of the angles with the horizontal line can be found by subtracting θ from $\pi/2$. Having found all angles at static equilibrium, Equation 2.9 can be used to find all equivalent vertical stiffnesses.

Having established the masses and stiffnesses in the three dof system, the natural frequency ω_0 can be calculated. Since the control problem is concerning control of the natural frequency of the solar deck system, this is the only property of the dynamic system that needs to be calculated. Writing the equation of motion for each of the new masses in the three dof problem gives the following Equation 2.14, Equation 2.15, and Equation 2.16.

$$2m \cdot \ddot{x}_1 = -k_{eq1} \cdot x_1 + k_{eq2} \cdot (x_2 - x_1) \tag{2.14}$$

$$2m \cdot \ddot{x}_2 = -k_{eq2} \cdot (x_2 - x_1) + k_{eq3} \cdot (x_3 - x_2) \tag{2.15}$$

$$m \cdot \ddot{x}_3 = -k_{eq3} \cdot (x_3 - x_2) \tag{2.16}$$

Collecting these equations into matrices gives the following Equation 2.17.

$$\begin{bmatrix} 2m & 0 & 0 \\ 0 & 2m & 0 \\ 0 & 0 & m \end{bmatrix} \cdot \begin{bmatrix} \ddot{x}_1 \\ \ddot{x}_2 \\ \ddot{x}_3 \end{bmatrix} = \begin{bmatrix} -k_{eq1} - k_{eq2} & k_{eq2} & 0 \\ k_{eq2} & -k_{eq2} - k_{eq3} & k_{eq3} \\ 0 & k_{eq3} & -k_{eq1} \end{bmatrix} \cdot \begin{bmatrix} x_1 \\ x_2 \\ x_3 \end{bmatrix} \tag{2.17}$$

For this problem, the natural frequency will be found by the classical eigenvalue problem as shown in (Bachynski et al. 2019, p. 71). The damping in the solar deck is also assumed to be negligible. Free vibration is therefore considered, implying Equation 2.18.

$$\mathbf{M}\ddot{\mathbf{x}} + \mathbf{K}\mathbf{x} = \mathbf{0} \tag{2.18}$$

A solution of the form as in Equation 2.19 is assumed.

$$\mathbf{x} = \mathbb{R}e\{\tilde{\mathbf{x}}e^{i\omega t}\} \tag{2.19}$$

Here, $\tilde{x}$ is a vector consisting of unknown complex constants (Bachynski et al. 2019). For Equation 2.18, this gives the following Equation 2.20.

$$(-\omega^2\mathbf{M} + \mathbf{K}) \cdot \tilde{\mathbf{x}}e^{i\omega t} = \mathbf{0} \tag{2.20}$$

The sought solutions from Equation 2.20 are the ones where $\mathbf{x}$ is non-zero and valid for all times t, so that the relation in Equation 2.21 is required.

$$(-\omega^2\mathbf{M} + \mathbf{K}) \cdot \tilde{\mathbf{x}} = \mathbf{0} \tag{2.21}$$

For $\tilde{x}$ to be nonzero, the following classical eigenvalue problem in Equation 2.22 must be solved for ω.

$$\det(-\omega^2\mathbf{M} + \mathbf{K}) = 0 \tag{2.22}$$

For the three dof problem, Equation 2.22 results in a third degree polynomial, which can be solved numerically in Matlab.

2.3 Hydrodynamics

2.3.1 Wave theory

For finite water depths, the velocity potential ϕ for regular waves is given as in Equation 2.23.

$$\phi = \frac{g\zeta_a}{\omega} \cdot \frac{cosh(k(z+h))}{cosh(kh)} \cdot cos(\omega t - kx) \tag{2.23}$$

Here, g is the acceleration of gravity, ζ_a is the amplitude of the wave, ω is the angular frequency of the wave, t is time, k is the wave number, and x is the 2D horizontal spatial variable. z is the vertical spatial coordinate with z = 0 at the still water level.

This velocity potential can be used to find the x and z components of the velocity and the acceleration. Since the multi-torus structure is meant to follow the waves in heave, the

z-components are of special interest. The z-components of velocity (w) and acceleration (a_3) then become as in Equation 2.24 and Equation 2.25 by differentiating the velocity potential.

$$w = \omega\zeta_a \cdot \frac{sinh(k(z+h))}{sinh(kh)} \cdot cos(\omega t - kx) \tag{2.24}$$

$$a_3 = -\omega^2\zeta_a \cdot \frac{sinh(k(z+h))}{sinh(kh)} \cdot sin(\omega t - kx) \tag{2.25}$$

Following the deep water assumption rule of thumb, the infinite water depth assumption is valid in the model tests to be done in this thesis if the wave length λ is less than 2 two times the water level of the basin tank. The water level here is assumed constant at approximately 0.8 meters, so the wave length must be less than 1.6m for this assumption to hold.

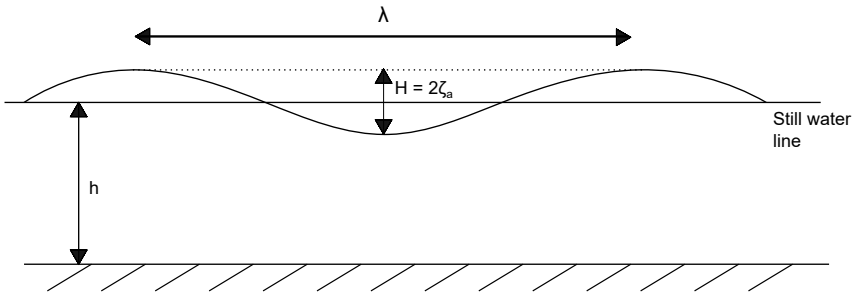

Figure 2.6: Regular wave with wave length $\lambda = \frac{2\pi}{k}$, where k is the wave number. Also, still water depth h, and wave height $H = 2\zeta_a$.

Regular wave theory is the theory of sinusoidal waves. Actual sea states in real life is assumed to be consisting of many regular waves, creating irregular waves. Surface elevation for a regular wave is given by Equation 2.26.

$$\zeta = \zeta_a \, sin(\omega t - kx) \tag{2.26}$$

ζ is the wave elevation, ζ_a is the amplitude of the wave, ω is the angular frequency of the wave, t is time, k is the wave number, and x is the 2D horizontal spatial variable. Wave height H is defined as $2 \cdot \zeta_a$. Wave steepness is then defined as H/λ.

The angular frequency ω and the wave number k are respectively connected to the wave period and wave length, through Equation 2.27 and Equation 2.28.

$$\omega = \frac{2\pi}{T} \tag{2.27}$$

$$k = \frac{2\pi}{\lambda} \tag{2.28}$$

The frequency ω and wave number k are related through the dispersion relation, which for shallow water is given by Equation 2.29. Deep water relations are usually used when $\lambda/H \geq 0.5$.

$$\omega^2 = k\, g\, tanh(kh) \tag{2.29}$$

And for deep water the relation simplifies to Equation 2.30. In both of the cases, k is the wave number and g is the gravitational constant.

$$\omega^2 = k\, g \tag{2.30}$$

Irregular waves are superpositions of sinusoidal regular waves, as treated in Pettersen 2018 (p. 5.1).

String excitation modes

The excitation forces on the member representing the solar deck in this thesis are assumed to mainly be forces acting perpendicular to the solar deck if this had been horizontal. Resonant vibrations on a string is possible to achieve with a perpendicular force on just one end. However, when the two fixed ends of the string representing the solar deck is connected to one floating element each, there will be two excitation forces on the string. These two forces can be applied at the two string ends at the same time to give string vibration with double amplitude in the middle of the string, under the assumption that the vertical motion of the two string ends are identical.

This double excited string vibration motion is believed to happen when the waves align to make the floater motions in heave coincide so that the floaters are on top of wave crests at the same time. This happens when there is an integer number of wave lengths between the floaters. The connection between the wave length λ and the length L between the floaters then become as in Equation 2.31.

$$\lambda \cdot n = L\,, \qquad n = 1,\, 2,\, 3,\, ... \tag{2.31}$$

Here, n is the number of wave lengths over the length L between two floaters. The required regular wave period for this to happen is given by Equation 2.32, assuming deep water conditions.

$$T = \frac{2\pi}{\omega} = \frac{2\pi}{\sqrt{kg}} = \frac{2\pi}{\sqrt{\frac{2\pi}{\lambda}g}} = \frac{2\pi}{\sqrt{\frac{2\pi n}{L}g}} = \frac{2\pi\sqrt{L}}{\sqrt{2\pi n g}}$$
$$= \sqrt{\frac{2\pi L}{ng}} \tag{2.32}$$

As mentioned, it is assumed that the vertical excitation of the solar deck ends is the dominating part of the total excitation forces. However, the mid-point of the solar deck will move vertically if the two end points are moved horizontally towards and away from each other in an oscillatory manner. This type of movement, however, is more of a change in the static configuration of the deck as a freely hanging member. Hence, this motion can be regarded as quasi-dynamic motion.

However, some dynamics may be involved with this type of movement for forces with large amplitudes. Furthermore, the horizontal and vertical modes might have a coupling. This could be explained by the two string ends moving up and down at the same time, resulting in up and down swinging of the deck, which may have an influence on the horizontal distance between the two end points. This may also work the other way around, when change in the horizontal distance between ends may cause vertical swinging motion, as mentioned above. These coupled phenomenons may depend on the material properties, e.g. elasticity, of the solar deck.

2.3.2 Wave body interaction

From Bachynski et al. 2019, in general the total wave field in a water body consists of all the free surface disturbances. The free surface disturbances are mainly incident, diffracted, and radiated waves. Some part of the free surface disturbances also consist of the local disturbances caused by diffraction and radiation.

The total velocity potential can be composed of eight independent velocity potentials. One velocity potential for the incident wave, and one for each of the six rigid body motions, and finally one for the diffracted wave, as shown in Equation 2.33.

$$\phi = \phi_0 + \sum_{i=1}^{6} \phi_i + \phi_7 \tag{2.33}$$

The six rigid body motion problems constitute the radiation problem. This concerns the free surface disturbances (including but not only waves) caused by the body forced to move in still water, that is no incident waves. This problem revolves around and yields the added mass and damping forces. Additionally, the restoring forces from the $\rho g z$ term in Bernoulli's equation is needed to describe the problem, as this is not included in the boundary value problem (BVP). The derivation and solution of the BVP for floating rigid bodies can be found in chapter 7 in Bachynski et al. 2019, but this is not the scope of this

thesis.

The problem of diffracted waves make up the diffraction problem. This concerns the free surface disturbances (including but not only waves) caused by the body held fixed in incoming incident waves. The incident waves then diffract off of the body, and contributes to the wave excitation forces. The wave excitation forces consist of the Froude-Krylov force and the diffraction force. The Froude-Krylov force typically makes up roughly half of the total force.

From Pettersen 2018, the radiation problem of can be formulated as in the following Equation 2.34. Newtons second law of motion is applied to the floating object in heave.

$$\sum F_{33} = M_{33} \cdot \ddot{\eta}_3 = -A_{33} \cdot \ddot{\eta}_3 - B_{33} \cdot \dot{\eta}_3 - C_{33} \cdot \eta_3 + F_{3,\,exc}$$
$$\implies F_{3,\,exc} = (M_{33} + A_{33}) \cdot \ddot{\eta}_3 + B_{33} \cdot \dot{\eta}_3 + C_{33} \cdot \eta_3 \tag{2.34}$$

Where M_{33} is the mass in heave of the object, A_{33} is the added mass in heave, while B_{33} is the damping coefficient in heave, and C33 is the stiffness coefficient in heave. η_3 is the motion in heave, so that $\dot{\eta}_3$ and $\ddot{\eta}_3$ becomes the velocity and acceleration in heave, respectively. $F_{3,\,exc}$ is the external excitation force in heave influencing the object.

From Pettersen 2018 and Odd Magnus Faltinsen 1990, added mass and damping coefficients are functions of the frequency of the applied external force, ω, when the object is near the surface. For an object deeply submerged, the added mass coefficient for a two-dimensional cylinder cross section is equal to the displaced volume, ∇, of the object. For the three-dimensional cylinder, the two-dimensional coefficient can be integrated over the length of the cylinder. For a floating two-dimensional circle with a draft equal to the radius, the limit added mass for when $\omega \to \infty$, is in the same manner equal to the mass of the displaced fluid volume. The added mass coefficient can then be written as in Equation 2.35.

$$A_{33} = \rho \cdot \nabla = \Delta \tag{2.35}$$

For the case when $\omega \to \infty$, the corresponding damping coefficient can be found to be zero. This heave damping coefficient is often negligible compared to the other coefficients. Lastly, the restoring coefficient in heave is given by Equation 2.36, regardless of the frequency.

$$C_{33} = \rho g A_{wp} \tag{2.36}$$

Showing that the small scale model follows the waves in heave

The length of a horizontal line over a circle (with diameter D and radius r) as a function of x, and x being the distance from the bottom to the line, given by Equation 2.37. The centre of the circle is located at the origin.

$$L_h(x) = 2 \cdot \sqrt{r^2 - (r - x)^2} \tag{2.37}$$

For the model scale cylinder, this becomes $L_h = 2 \cdot \sqrt{0.075^2 - (0.075 - 0.05)^2} = \frac{\sqrt{2}}{10} \approx 0.141$. A_{wp} for one cylinder in the model scale is therefore $0.9m \cdot 0.141m = 0.126m^2$. The waterplane stiffness coefficient from Equation 2.36 then becomes $1000 \cdot 9.81 \cdot 0.126$ N/m = 1236 N/m. For comparison, the added mass coefficient of one cylinder from the small scale model becomes, from Equation 2.35, $1000 \cdot 0.00516 \cdot 0.9 = 4.64.6kg$, where 0.00516 m^2 is the submerged area, and 0.9 m is the length of one cylinder, as shall be seen later. This means that the waterplane stiffness is far larger than the added mass and the damping, meaning that the floaters will follow the waves to a large extent, as intended. For simulation purposes, the elevation of the structure will then be identically equal to the wave elevation. These results are in line with the specification of the structure to be able to follow the waves closely.

Additionally, in order for the structure to be light and follow the waves, the draft had to be reduced to less than the radius of the cylinder. The draft of one third of the diameter gives some nonlinear effects, since linear theory assumes that the walls are vertical where they meet the still free surface. As discussed on email with Trygve Kristiansen (T. Kristiansen, personal communication, June 2022) this may give some nonlinear diffraction and radiation phenomenons, leading to superimposed wave profiles consisting of the incident and higher wave frequencies in between the cylinders. This can be seen in the FFT plots, as will be seen in Section 5.

2.4 Fast Fourier Transform

The Fast Fourier Transform (FFT) is one particular (and efficient) algorithm for computing the Discrete Fourier Transform (DFT) of a dataset containing a certain number of data points (Weisstein 2022a). The general, continuous Fourier Transform is given as in Equation 2.38.

$$\mathscr{F}\{f(t)\} = F(\omega) = \frac{1}{\sqrt{2\pi}} \int_{-\infty}^{\infty} f(t) e^{-i\omega t}\, dt \tag{2.38}$$

Here, $\mathscr{F}$ denotes the Fourier Transform operator, and f(t) : $\mathbb{R} \mapsto \mathbb{R}$ is a real function with real input t. It does not have to be a real function, it can also be complex. But for the purposes of this thesis, the inputs will be real as the sampled data is real-valued. The transform variable ω is the new Fourier Transformed running variable. The imaginary number i is in some definitions also included in the new variable, as F(iω). Lastly, e is Euler's number.

The continuous Fourier Transform is applied to continuous functions. However, applying the Fourier Transform on discrete data is also possible through the use of the Discrete Fourier Transform. This transform is similar to the continuous one, but with the difference in that the input to the transform is discrete datapoints, not continuous

functions. Applying the Discrete Fourier Transform to discrete data, it transforms N samples $x_n \coloneqq \{x_0, x_1, x_2, \ldots, x_{N-1}\}$ to the sequence $X_k \coloneqq \{X_0, X_1, X_2, \ldots, X_{N-1}\}$. This transform is done as shown in Equation 2.39.

$$X_k = \mathscr{F}\{x\} = \sum_{k=0}^{N-1} x_n \, e^{-i\frac{nk}{N}} \tag{2.39}$$

Here, k is the kth entry in the sequence X_k, which in total then will consist of N complex entries from the set x_n. The FFT algorithm is in a way simply an algorithm that fits polynomials of degree N, using N+1 distinct known points along the polynomial. The algorithm is a fast way to do the calculations corresponding to the DFT (Weisstein 2022b). The working principle behind the simplest variant, the radix-2 decimation-in-time (DIT) method, is that the discrete transforms are recursively split into two parts, one even and one odd part. There are other methods that do not rely on the sample size being a power of two, but these are a lot more complicated. The splitting of the problem allows the algorithm to evaluate fewer expressions due to the mirroring properties of even and odd functions. This can be illustrated through the Fourier matrix, as can be seen in Weisstein 2022c, but this will not be done in detail here. For a sample of n points the FFT algorithm reduces the amount of operations to be done to be of time-complexity $\mathcal{O}(n \log_2 n)$, where $\log_2 n$ is the base 2 logarithm. This is an improvement from the usual DFT time-complexity of $\mathcal{O}(n^2)$.

2.5 Control formulation

The solar deck makes up a dynamic system, which can be described by Equation 2.40.

$$m\ddot{x} + c\dot{x} + kx = F_{exc} \tag{2.40}$$

m is here the characteristic mass of the system, while c and k are the damping and stiffness in the system, and F_{exc} is the external excitation force affecting the system. x is the position of the masses in the system, so that $\ddot{x}$ and $\dot{x}$ become the acceleration and velocity, respectively. This is similar to in Equation 2.34, just that the dynamics now describe the freely hanging solar deck motions. This system can be written in the classical form as in Equation 2.41, when the external forcing is zero.

$$\ddot{x} + 2\zeta\omega_n\dot{x} + \omega_n^2 x = 0 \tag{2.41}$$

Here, ω_n is the natural frequency (also often called the eigenfrequency in this thesis) of the system, which is the frequency the system tends to vibrate in. Furthermore, ζ is the damping ratio between the actual damping c and the critical damping which for any mass spring damper system is $2 \cdot \sqrt{km}$. The goal is to control the natural frequency by changing the tension in the solar deck. One variable being controlled by another single variable leads to a single input single output (SISO) characterization of the control system. The

control state is then given by Equation 2.42.

$$\mathbf{x} = \omega_{0,\,deck} = \sqrt{\frac{k}{m}} \tag{2.42}$$

For actuating purposes, the winch types envisaged to be used in a full scale installation are assumed to have feedback control on the tension they produce. This is in order for the tension level not overshooting, thus using more energy than is needed. This could be achieved by for example a Proportional-Integral-Derivative (PID) controller, as treated in Balchen, Andresen and Foss 2016 (p. 347).

3 Motion control

A goal is to propose ways to control the tension in the deck efficiently, contributing to research in the field of control of flexible structures, while also contributing to the development of the solar deck design in the multi-torus concept.

3.1 Control for the flexible structure

The multi-torus floating island is a flexible structure. In other words, the toruses can be bent around axes perpendicular to the axis going through the center of the torus cross section, all while not being deformed permanently. This is necessary, as the multi-torus concept is intended to follow the wave motion in heave. The solar deck needs to be flexible as well, for it not to interfere with the flexibility of the torus structure.

Additional mobility of the flexible system is added when the solar deck is considered. The solar deck is resting on top of the toruses, carrying the mass of the rigid solar panels. The solar deck being elevated over the water surface has both advantages and disadvantages. It will reduce the probability of flooding the structure, given that good drainage systems are implemented. However, the deck being raised up from the water removes the cooling effect from the water. This was one of the reasons why FPVs have gained traction, so not including this feature is not beneficial for the electrical efficiency. Also, the deck being suspended in mid-air between the toruses can lead to slamming loads from waves from beneath. Most importantly, the freely hanging solar deck allows swinging motions to occur; reducing the extent to which this happens is the scope of this thesis.

There are several methods to mitigate the risk of resonant vibrations in the solar deck. Since this thesis is a conceptual study, some measures will be briefly mentioned and discussed here. The measures can be divided into passive and active methods of control. The passive ones include installing more carrying mechanisms and support for the solar deck in the areas between the toruses. This increases the rigidness of the solar deck, reducing the degree to which the solar panel carrying deck is hanging freely and therefore the proneness to vibrations.

However, a more rigid solar deck might interfere with the flexibility of the structure, hence affecting the ability to follow the waves. Therefore, an active control method is proposed here using winches. A control system can be implemented so that the tension and rigidity of the structure is controlled depending on the sea state. In calm sea states with long peak periods and small significant wave heights, no control is needed and the structure can float freely as intended. For rough sea states with steep waves, the multi-torus structure seems to be the most exposed to extreme wave excited motions (Sigstad 2019 and Winsvold 2018). In these rough sea states, resonant vibrations in the solar deck are more likely, so in these sea states the tension of the deck can be changed in order to avoid resonance.

Winching action is here proposed as the way to control the tension of the solar deck. Winches can only produce pulling forces, meaning that the winches must be placed in such a manner that they can efficiently increase the tension in the solar deck, so that the deck experiences increased tension and becomes less prone to swinging motions. Some winches

also have locking mechanisms so that they can maintain a tension level using little to no power. This is beneficial in offshore locations as the rough weather conditions can last for a long time. However, changing the tension in the solar deck is not the only way to affect its swinging motion. The deck can be approximated as a string, as seen in the following. Here, the eigenfrequency of the string approximated deck is changed by applying force in the middle of the string.

From the equation for the eigenfrequency for a string, Equation 2.5, it can be seen that the eigenfrequency of each mode n changes with $\frac{1}{L}$ and $\sqrt{T}$, where L and T are the length and tension of the string approximated deck. These two variables are the only ones that can be altered by control actuators, and changing one of them affects the other to a small degree according to the freely hanging parabola equation, Equation 2.3. The tension T is the variable that mainly can be changed, as the length between the toruses are assumed to be somewhat constant. Therefore, the natural frequency of the deck is mainly changed with the square root of the tension. Since the square root function is a slowly increasing function, this is mathematically not an efficient way of changing the natural frequency of the solar deck.

A more effective way would be to change L, which could be done in full scale by lifting or applying an upward force in between two toruses. This force could be evenly distributed or at discrete points. A 2D visualization of a single vertical force applied in the middle between two toruses is shown in Figure 3.1.

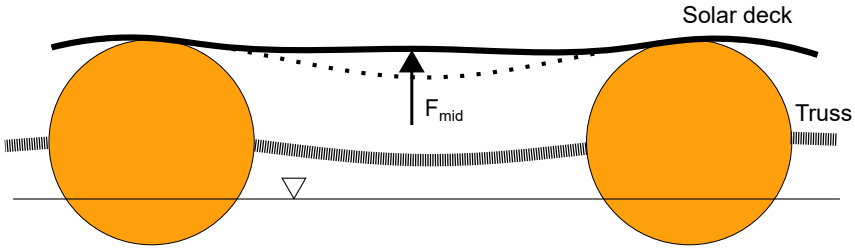

Figure 3.1: An alternative to tension control. A control principle where an external vertical force is applied to the solar deck, effectively halving the characteristic length L of the string-approximated solar deck behaviour.

3.2 Efficient winch control

Adding winches to the floating island will result in some additional mass to be accounted for. A winch with a high pulling force to own mass ratio is therefore preferable in a full scale installation, so the total mass of the solar island is not too heavily influenced by the winches.

There are several types of winches with different working principles, including hydraulic or air winches, and electric winches. The hydraulic winch is more efficient and reliable than the electrical winch (Offshore-Technology 2022). Air winch is often used in the marine industry because of its efficiency and power output. It uses air as the power source from a pneumatic motor (Thern-Winches-and-Cranes 2022), meaning there is no electrical sparks, reducing the risk of explosions and water short circuiting the mechanism. Air-winch could

be a good alternative because of this although compressed air would have to be available for when winching action would take place. On the other hand, electrical winches are often easier to install, which is important for FPV concepts to be competitive in the market (Offshore-Technology 2022).

A locking mechanism on the winches is necessary for the winch to hold the tension in the deck until the weather calms and the controller commands change in tension. Alternatively, an electrical winch could use power holding the tension, but this would use a lot of energy. Therefore, passive tension holding mechanisms are preferred. Most winches have built-in brake mechanisms on either the motor, transmission, or the drum, in order to hold tension (EMCE-Winches 2022). Friction plates push on a rotating plate, causing it to be locked in place. Other locking mechanisms are gear based, in which case gear grinding and fatigue would be a concern. However, locking mechanisms are seldom installed on pulling winches, only on lifting winches (EMCE-Winches 2022). Locking mechanisms are necessary for lifting winches in order to prevent the load to suddenly drop. Other alternatives could therefore be investigated.

Another alternative is making a system of winches and passive locking mechanisms. This can be implemented by having the tension cables being composites of chain, together with either metal or synthetic wire, much like mooring lines in general offshore applications. In order to easily lock the position of the tension cables, chain is a possible alternative for the ends of the tensioned cable. In this case, a stud-less chain type as shown in Figure 3.2 could be useful, since there is room for automatically sticking a locking pin into the chain rings. There would have to be implemented an automatic chain locking mechanism, as in MacGregor 2022, but in smaller scale.

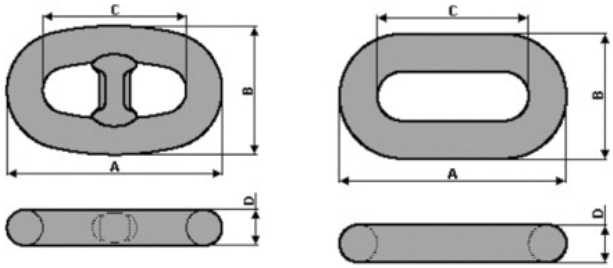

(a) Stud-Link (b) Studless Chain

Figure 3.2: Stud-link and stud-less chains that could be used in the winching system in order to allow the tension to be passively kept at a constant value. Photo courtesy of David T. Brown and Subrata K. Chakrabarti, from Brown and Chakrabarti 2005.

An example of a chain locking mechanism is the alternative used in the model tests in this thesis. This locking mechanism is shown in Figure 3.3. This mechanism locks the chain directly, so the winch would then not have to do the locking. This could be an advantage, but it could also make the tension system unnecessarily advanced, making the installing process tedious and inefficient. The chain would then need to be pulled by the winch through this locking mechanism which would need to be fixed in order to hold the tension. In other words, a somewhat challenging engineering task.

Figure 3.3: The locking mechanism of the chain hoist used in the model tests in this thesis.

There is likely some gear- or pin-based locking mechanism in the interior of the chain locker in Figure 3.3. These are also exposed to fatigue from cyclic and repetitive loads, which will be present for an offshore tension control system.

For the wire rope alternatives, usual materials used in offshore applications are polyester, nylon, high-modulus polyethylene (HMPE), and aramid (Brown and Chakrabarti 2005). These are synthetic materials, and therefore less prone to corrosion. The multi-torus floating solar island is meant to stay in the ocean all year round, meaning good materials will have to be chosen for all components. Metal wires are prone to corrosion, but they have smaller elongation than synthetics. Corrosion is likely the biggest challenge to overcome for metal tension cables offshore. Therefore, synthetic tension cables could be an appropriate alternative for winches actuating on the solar island all year round.

In summary, the setup of winches and tensioned cables will pose many challenges to make an efficient and functioning tension system in a full scale installation.

3.3 Full scale control proposals

Control for the full scale installation can be envisioned in a couple of different ways, as seen in the following. A global control approach for the multi-torus structure could be implemented as conceptually visualized in Figure 3.4. However, this global control method would require many winching actuators, or a well designed pulley system enabling one winch actuator to pull along several diagonals. This would cause losses through the pulleys. Therefore, powerful winch actuators would be needed.

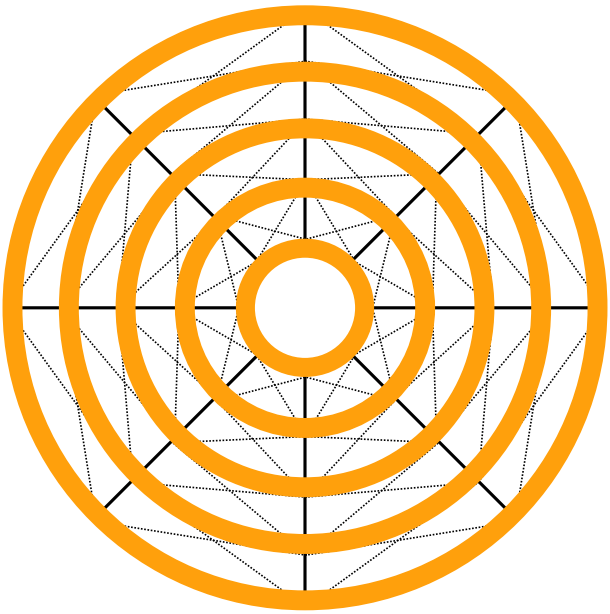

Figure 3.4: This is a control concept briefly discussed with the supervisors. Since each of the eight sectors between the toruses are divided into squares, pulling in one direction will cause wrinkles or slack in some other direction. Therefore, it is proposed to pull in both diagonals, shown as the dotted lines in the figure.

In addition, the pulling action and how it might occur is uncertain and therefore tentative. It could be envisioned that the winching action takes place on the toruses themselves, acting in tandem with the trusses, or the winches could pull on the solar deck. Pulling on the toruses would lead to torus deformations as shown in Figure 3.6, which could have negative implications on the compatibility of the structure. Alternatively, pulling action could be done on the solar deck itself. If the solar deck is in the form of a net, winching hooks can easily be fastened to the solar deck using the holes. Another option is to let there be wire rope fastened to the net itself along the dotted lines, so that tension is transferred through this wire.

Another control method for the solar deck on top of the multi-torus structure is shown in Figure 3.5.

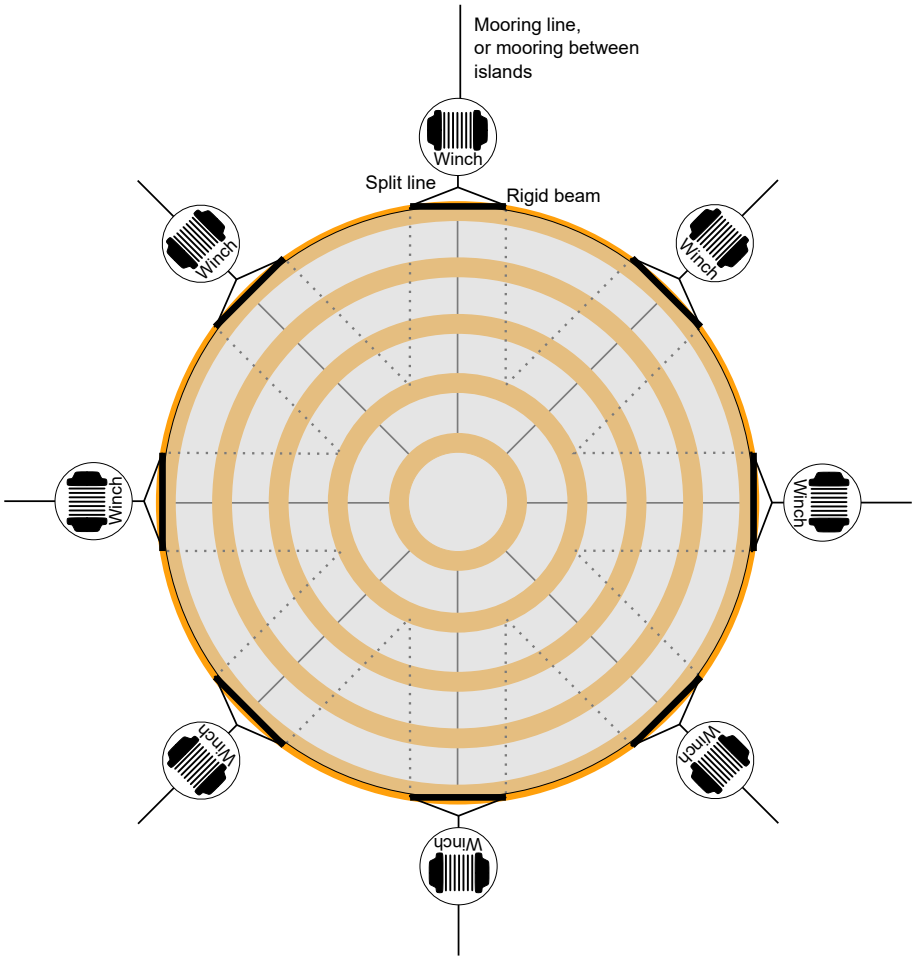

Figure 3.5: A control approach setup where the circular membrane deck is tightened in eight directions, by means of a stiff beam clamped at the end of the circular solar deck. The pulling action would then be done on the beam via a split-line, and not at a singular point on the periphery of the membrane.

This winching control approach would reduce the amount of wrinkling inside of the dotted area in the figure. However, some wrinkling would be expected outside of the dotted area, but increasing the length of the beams, and possibly letting the beams be curved would reduce the area outside of the dotted line.

3.3.1 Challenges with increasing tension in the solar deck

An issue with using winch at discrete points within the flexible structure is that the toruses might take a different shape, depending on the amount of directions that have winching action. This is illustrated in Figure 3.6.

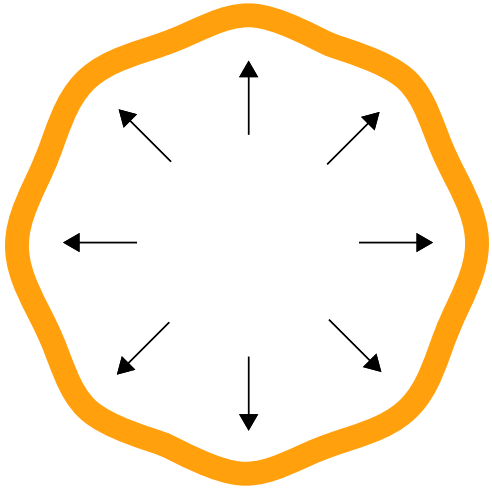

Figure 3.6: Deformed torus due to winch forces working at discrete points.

Torus deformations are also dependent on how the winching force propagates through the structure. If the solar membrane deck is to a large extent fixed to the toruses at e.g. the top of the toruses, the winching force would propagate through the toruses and would lead to these aforementioned torus deformations. Pulling on the deck would have little effect on the tension in the deck, or would require much more force as the increased tension would propagate through the toruses, causing deformations in the toruses. However, if the solar deck is adhered to the toruses only at some places along the toruses, the winching action would mainly propagate through the solar deck, which is desired. This setup where the solar deck is not considerably adhered to the toruses would require proper designs.

Another challenge would be the change in solar panel position relative to the toruses when pulling on the deck, if the solar deck to some degree is free to move over the toruses. Some margin would be needed for the placement of solar panels near the top of the torus, in order for crystalline rigid solar panels not to break over the torus curvature, as shown in Figure 3.7. This would not be an issue with flexible film PV technology, which would be able to bend with the torus curvature.

The issue in Figure 3.7 is a general challenge with the multi-torus concept as a floating island support structure for PV equipment. If the solar deck is meant to be flexible like the toruses, it is not beneficial to place rigid PV panels on top of it.

A final problem would be wrinkling and stretching of the solar deck, as shown in Figure 3.9 and Figure 3.8. This is a concern for example for the solar panels attached to the membrane, as stretching and wrinkling can lead to changed distances between geometrical points within the membrane. This can induce shear stresses on the adhering mechanism that fixes the solar panels to the flexible solar deck.

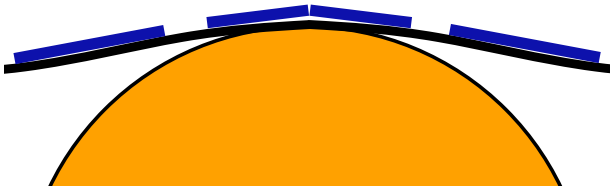

Figure 3.7: The issue of crystalline rigid solar panel breaking over the curvature of the torus.

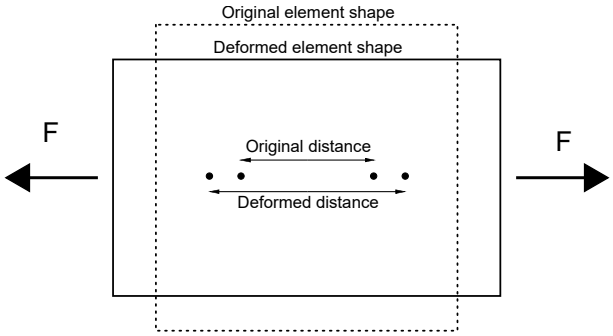

Figure 3.8: Membrane element stretching in one direction leading to compatibility problems for the solar panels where they are fixed to the membrane. This assumes an elastic membrane.

A solar panel being fixed at, for the sake of argument, 2 points to the membrane deck would also be affected by winching action. This is shown in Figure 3.8, as two points on an elongated elastic membrane experiencing stretching will be further apart. This induces shear forces on everything that is attached to the membrane, so this is an important aspect to consider when designing the membrane deck in the multi-torus structure.

However, overcoming stretching and wrinkling might be a challenge that is easily avoidable. If a not too elastic membrane deck is chosen, the membrane will not elongate, inducing shear stresses in the adhering mechanism fixing equipment to the membrane, and it will keep its original length for all tension conditions.

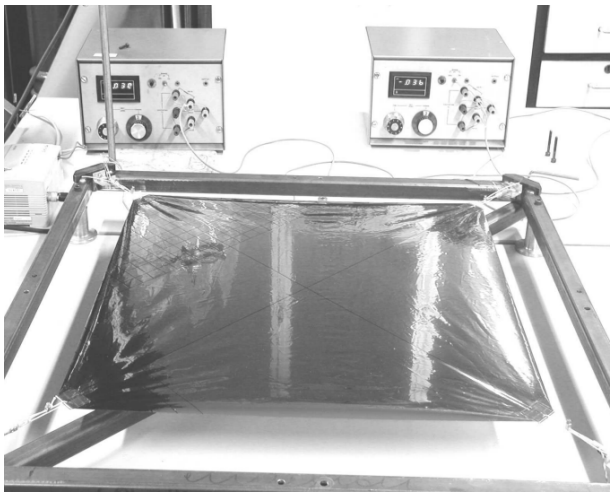

Figure 3.9: Wrinkles in a square membrane tensioned in the diagonal directions, where the diagonal forces are equal, or having a 1:1 ratio. Photo courtesy of Y. Wesley Wong and Sergio Pellegrino from Wong and Pellegrino 2006.

3.4 Solar deck motion control

For the project thesis made during the fall of 2021, an active PID control algorithm for the system was proposed. This controller was intended to control the tension and sag in the solar deck over one wave period, trying to counteract the waves pulling the toruses apart from each other. This controller would probably cause unnecessary wear and tear on the actuators and possibly fatigue in some components in the structure. It would also use a substantial amount of power, possibly more than the solar island could produce, making the whole control scheme pointless. This concept was therefore abandoned, and in this thesis the concept revolves around controlling the natural frequency of the solar deck based on the sea state. This means altering tension less often, only when the sea states are changing, in a semi-active control scheme.

The control scheme proposed in this thesis is based on frequency of the incoming waves. The wave height is not considered, but should in reality also be an input as a control parameter. The wave height could also be measured, or given as forecasted weather data. For using the structure as a wave estimator, Inertial Measurement Units (IMUs), or alternatively only accelerometers, would have to be mounted on the outer torus in a full scale installation. The device would measure the motion of the structure in heave, with the purpose of performing the FFT algorithm regularly on a stored data window of a given size and duration. The toruses are coupled hydrodynamically (Kristiansen et al. 2021), which could lead to smaller motion amplitudes of the inner toruses. The outermost torus is not shielded by other toruses, and may therefore be the torus following the waves in heave the closest. Optimal positioning of IMU devices might therefore be along the outermost torus.

For the present sea state, a dominant wave frequency will be obtained from the FFT algorithm. Based on the measured and known tension in the solar deck, the eigenfrequency of the solar deck will be calculated as a function of the measured tension in the deck.

The calculated present eigenfrequency is then compared to the dominant frequency of the present sea state. If they are similar and resonance resultingly being likely, the winching actuators are engaged to change the tension in the solar deck. This scheme is shown in Figure 3.10.

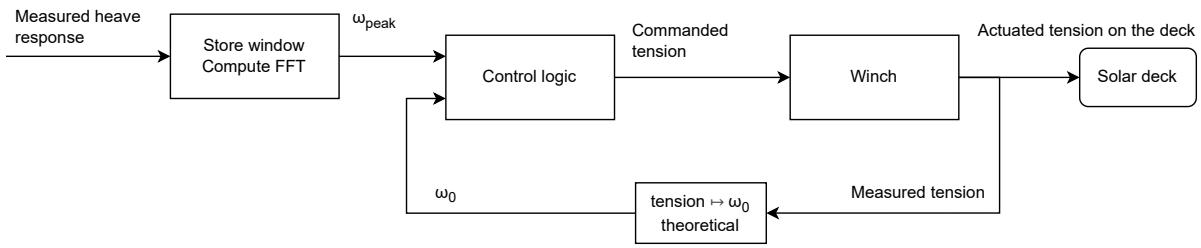

Figure 3.10: Control system using the FFT in a semi-avtive control scheme.

The control system in Figure 3.10 was not tested closed-loop in the model tests. No pulling actuator was included in the model tests in this thesis because of lack of strength in the actuators believed to fit the purpose. This represented one step away from a realistic closed-loop system, although sending commands to pulling actuators to produce a given (calibrated or measured) tension level is trivial, and is therefore not strictly necessary to show the working principle of the control system.

Since the control system shown in Figure 3.10 consists of discrete operations, it can be simulated as a discrete event simulation (DES). Each event can therefore be simulated by itself to demonstrate the working principle. However, as part of the closed system, the real-time FFT algorithm was implemented in the model test. The other events of interest in Figure 3.10 is the control logic module and the theoretical natural frequency calculation module. The winch is assumed to have an internal PID controller in order to not overshoot the desired tension level, so it will not be treated any further. The three events of interest are described in the following.

3.4.1 FFT algorithm and its implementation in the model tests

In the store window and compute FFT block, FFT is performed on the stored data window, yielding a frequency spectrum. ω_{peak} is extracted by locating the index of the max value of this spectrum. Applying the FFT algorithm to a stored data window is a lagging control scheme, as mentioned in the introduction of this thesis (Fossen 2021). However, this is acceptable when the control state changes rarely, as is the case for sea states. It is therefore proposed to perform FFT in a full scale installation for data gathered for 30 minutes, as this will give checkpoints for the controller a couple of times per hour. This should be enough, given that the present sea state does not change faster than this.

The FFT algorithm was implemented in the model tests using open source code from Qualisys, and adding some code lines to store and compute the FFT on batches of data. The data collected from the Oqus cameras is visual position data, meaning that velocity and accelerations are not considered in the FFT algorithm. This is unrealistic in a full scale installation, as direct position measurements will most likely not be available. However,

this was the only data that could be processed in real-time during the model tests, as accelerations are stored in the *.bin* files created after test runs are done.

The computer running the code will be receiving position data constantly from the camera feed. In the model test, FFT will be computed on the stored data windows for one of the Qualisys position markers meeting the waves first, which is marker 4. The data will be collected over a time period given by T_{window} in Equation 3.1.

$$T_{window} = N_{window} \cdot T_{sampling} = \frac{N_{window}}{F_{sampling}} \tag{3.1}$$

Where N_{window} is the total number of samples in a data window, while $T_{sampling}$ measured in [seconds/sample] is the time used to take one sample, and $F_{sampling}$ measured in [samples/second] is the sampling frequency. The maximum sampling rate of the position of the Qualisys markers is 50 Hz.

The FFT functions in Python and Matlab produce vectors of complex outputs. This vector contains an equal amount of elements as the data window parsed into the function. However, the last half of the resulting FFT vector will be mirroring of the first half of the vector, as shown in Figure 3.11. This is due to the complex nature of the Fourier Transform. Therefore, the last half of the vector can be excluded, so that the de-mirrored frequency results can be plotted like a frequency spectrum.

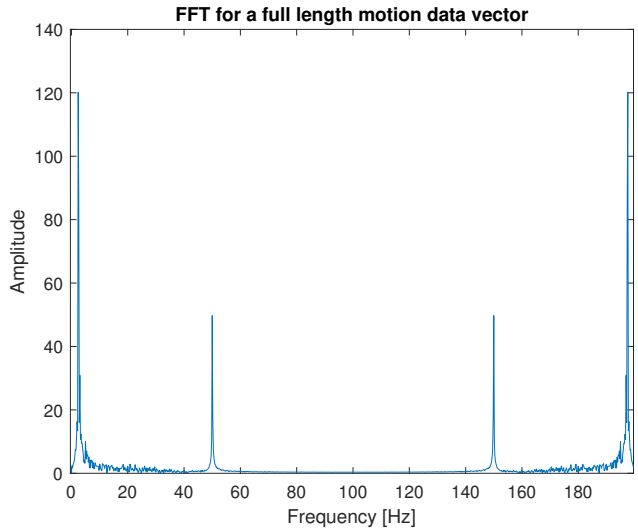

Figure 3.11: The whole resulting FFT frequency vector plotted against the corresponding frequency in Hz. This results in a mirrored plot, due to the complex nature of the Fourier Transform.

The x-axis vector needed in order to plot the resulting FFT frequency spectrum can be constructed from the motion data sampling parameters. Just like with the built-in FFT functions, there are functions constructing this vector as well, like the $rfftfreq(x, y)$ function in Python which takes N_window and F_interval as input (MacLeod 2022). The frequency interval is given as in Equation 3.2.

$$F_{interval} = \frac{F_{sampling}}{N_{window}} \tag{3.2}$$

The resulting frequency vector is equally long as the FFT vector, which for the de-mirrored case is half as long as the specified data window size. The frequency vector consists of linearly spaced elements, starting at zero with increment equal to $F_{interval}$. The last value in the vector will then be equal to $F_{sampling}$ divided by 2 for the de-mirrored case.

The pseudo-code and algorithm for the code used to capture real-time data and computing real-time FFT on a data window is shown below.

Python code

```
N = window_size
z4vec ← null
packet_counter ← 0
Callback: data packet received
z4vec ← data packet
packet_counter ← packet_counter + 1
if packet_counter == N then
    Normalize z4vec around zero
    FFT(z4vec)
    Save plot
    z4vec ← null
    packet_counter ← 0
end if
```

Here, z4vec is the vector preallocated for receiving data on the vertical position of motion capture marker 4. This marker is placed on the middle of the cylinder meeting the waves first, which is assumed to follow the waves the closest of the two cylinders. The variable packet_counter is used to keep track of the number of data points that have been inserted into z4vec. The packet_counter is compared to the predetermined $N = window\_size$ in order to include the desired number of data points when FFT is computed.

3.4.2 Control logic

There are assumed two main methods for the controller to find the desired tension levels. One is to use a model of the system so that the natural frequency of the solar deck is given as a function of the present tension. This would require a high-fidelity model of the dynamics of the solar deck, so that based on the current tension level, a natural frequency can be found. If the sea state frequency and the natural frequency of the solar deck is found to be similar, the optimal tension level given the current sea state can be commanded. This is useful as the optimal tension level is not necessarily above the current tension level. However, as mentioned, this would require a high fidelity model of the solar deck dynamics. However, this is only based on frequency, so if resonant waves of negligible

amplitudes are incoming, the controller might unnecessarily command a new tension level. This is a shortcoming the frequency based semi-active controller proposed in this thesis.

The other method is to use a look-up table or empirical mapping from model tests or full scale tests. This is based on measuring the response for various wave frequencies and tension levels, obtaining a heat-map over the motion in critical parts of the structure. These two methods are elaborated on in the following.

Control logic based on model of the system

The eigenfrequency of the solar deck can be calculated as a function of the present tension level in the solar deck, in accordance with a representative mathematical model of the solar deck. Two modelling approaches are here proposed in Section 2. The most high-fidelity one is based the discrete mass system shown in Figure 2.3. A more simple model is the string equation, given in Equation 2.5, rewritten under.

$$\omega_{0,n} = \frac{n\pi}{l}\sqrt{\frac{T}{m}}$$

The dominant frequency of the sea state can be assumed constant over a short period of time of about 30 minutes. If the eigenfrequency as a function of the present tension level matches the dominant frequency of the waves for a given FFT data window, resonance is likely. The eigenfrequency of the solar deck should then be changed. The eigenfrequency equation can then be written in terms of tension, as shown in Equation 3.3.

$$T = \frac{(\omega L)^2 m}{(n\pi)^2} \tag{3.3}$$

ω is now the resonant wave frequency which is constant at present, the linear mass m is constant, and L is approximately constant for neighbouring tension levels. The vibration mode should be shifted in order to change the mode of the string vibration and avoid the current resonant vibrations. The mode number n is therefore changed to being not a whole number. Changing n to a smaller number than 1 (which was assumed to be the mode of most concern) means increasing the tension, so there are limits to how much this can be done. Setting n = 0.75 gives the calculation in Equation 3.4.

$$T_{new} = \frac{T_{old}}{n^2} = \frac{T_{old}}{0.75^2} = \frac{16}{9} \cdot T_{old} \approx 1.78 \cdot T_{old} \tag{3.4}$$

A better result could be achieved by setting n as small as possible. Setting n = 0.5 is an option, but this results in a tension four times as large as before, which is not feasible for a full scale installation. However, the effect of this extreme tension increasement was tested during the lab tests.

Control logic based on a lookup table

The controller is very simple, as can be seen from the above. At first it was theorized

that it should only increase tension upon detecting resonance probability, as shown above. However, in light of the model tests, it seems that for some combinations of excitation frequencies and deck tensions, increasing the deck tension leads to larger vertical motion amplitudes in the solar deck. In some cases, a better result with regard to vertical deck motion can therefore be achieved by lowering the tension. These examples contradicts the aforementioned theory.

This leads to the possibility of introducing an empirical look-up-table type controller, where the controller input is the peak period or frequency, and it uses the minimize function on the isolated curve for the given peak period or frequency. The tension yielding the lowest motion amplitudes in the deck can then easily be returned and parsed on as a signal to the actuators. This would require an empirically and experimentally obtained matrix of peak periods and tension levels, like what is obtained in the model tests in this thesis.

3.4.3 Theoretical natural frequency calculation

For a string approximated solar deck behaviour, this can be done directly by calculating the natural frequency in the string equation based on the measured tension T, according to Equation 2.5. However, the string equation is most likely not a sufficiently representative model to correctly model the behaviour of the solar deck, due to its high linear mass and sag. The disadvantage of a semi-active control system is that a representative model of the control system dynamic is needed because of the larger gaps in time between comparison of measured and desired values (Septimiu, Chira and Roşca 2005).

4 Model test

In this section, the work done before, during, and after in connection with the experimental model tests will be presented. The model was made during January and February and was supposed to be tested in February and March, but due to covid-19 outbreaks, the production of the model was delayed. Therefore, the model tests took place in May.

The model was made by Trond Innset and Ole Erik Vinje from NTNU. Robert Opland, Terje Røsten, and Torgeir Wahl helped installing the model in the small model tank (Lilletanken). The model was made in scal 1:10.67 of what is believed to be a fitting size for a full scale installation. The main goal of the model testing was observing the behaviour of the solar deck in a larger scale than before and assess the likelihood of resonant vibrations and swinging motions on it.

A goal was also to contribute to a development towards a closed-loop system for controlling the tension in the deck. Therefore, real-time FFT wave estimation was implemented, although no actuators were included in the model tests.

4.1 Scaling

Scaling paragraph: From Steen 2014, similarity between forces in full scale and model scale concepts can be achieved by demanding geometrical (shape), kinematic (motion), and dynamic (force) similarity. It can be difficult to have all these similarities satisfied, so Froude scaling is often used as an alternative.

With Froude scaling, an initial scaling factor λ is defined as the ratio between two known lengths of the full scale and the small scale system. This ratio can be defined as $\lambda = \frac{L_F}{L_M}$. The fluid density in full and model scale then become important parameters contributing to the scaling, as these are often not the same; $\rho_F = 1025\ kg/m^3$ and $\rho_M = 1000\ kg/m^3$ are typical values. Scaling can then be done according to the following Table 1.

Table 1: Scaling factors used for converting between small and full scale. When calculating model scale values, it is assumed that $\rho_{FS} = 1025\ kg/m^3$ and $\rho_{MS} = 1000\ kg/m^3$

Parameter	Full scale (=)	Scaling factor	Model scale	Unit
Length	L_F	λ	L_M	[m]
Structural mass	M_F	$\lambda^3 \cdot \rho_F/\rho_M$	M_M	[kg]
Force	F_F	$\lambda^3 \cdot \rho_F/\rho_M$	F_M	[N]
Moment	M_F	$\lambda^4 \cdot \rho_F/\rho_M$	M_M	[Nm]
Acceleration	a_F	1	a_M	[m/s^2]
Time	T_F	$\sqrt{\lambda}$	T_M	[s]
Pressure	P_F	$\lambda \cdot \rho_F/\rho_M$	P_M	[N/m^2]

The cylinder that was deployed for the floaters had a diameter of 0.15 m. From Winsvold 2018, the full scale cross section diameter of each torus is given as 1.6 m. Knowing these corresponding measurements, the scaling factor can be calculated as $\lambda = \frac{1.6m}{0.15m} = 10.67$. Hence, the rest of the structure dimensions that are applicable to the 2D simplified model was dimensioned with this $\lambda = 10.67$.

4.2 Dimensions of small scale model

The wave maker in the small water basin used can make regular waves with $H \approx 0.2m$, depending on the frequency. Given an assumed wave height out at sea to be roughly 4 m, this means a scaling factor $\lambda = \frac{4m}{0.25m} = 16$. This was the initial sought scaling factor and would result in a cylinder with a diameter of $\frac{1.6m}{16} = 0.1$ m. This was believed to be too small of a scale to observe the system satisfactorily. A larger cylinder was therefore required. The mass of the model was also of significance, so a lightweight plexiglass cylinder was located, which had an outer diameter of 0.15 meters. The rest of the small scale model was made in accordance with the scale these measurements resulted in, which was $\frac{1.6m}{0.15m} = 10.67$.

Although the full scale waves are assumed 4m, the max wave height tested was 0.08m, corresponding to 0.85 m in full scale. There are some constraints on the wave heights the wave maker is able to produce given the relatively high excitation frequency needed to provoke swinging in the deck. This high wave frequency is impossible to combine with the sought wave height of 0.2 m in model scale. 0.85 m waves in full scale are not that large when seen in comparison to possible conditions at sea. However, because of how the model is designed, with nothing but the solar deck itself in between the floating cylinders, these waves were not tested in case the model would snap. Additionally, the most important aspect of the model tests was to provoke first mode vibrations in the solar deck, to observe how the tension affected these vibrations.

As mentioned, there are some uncertainties with the multi-torus structure dimensions. The full scale dimensions retrieved for the full scale concept from Winsvold 2018 and Sigstad 2019 are scaled up from their respective small scale models. The global diameter of the outer torus of 1 meter in these works can be scaled up to 50 meters in full scale. However, the data from Winsvold 2018 and Sigstad 2019 are not necessarily descriptive of an actual full scale installation, as the research done on the multi-torus concept so far has been conceptual studies. Therefore, the cylinder diameters and the distance between them might not be optimal in relation to the total size of the floating island.

Producing the model used in this thesis, the cylinders were attempted to be made as light-weight as possible. The solar panel loads in full scale were provided by Trygve Kristiansen directly, as 30-50 kg/m^2, so 40 kg/m^2 was chosen. The elasticity of the solar deck was never quantified, so no data is available for this. The net used for the model in this thesis was not very elastic. As seen in Section 3, this is beneficial when considering membrane stretching. However, it could be beneficial for the flexibility of the structure as a whole that the solar deck is somewhat elastic.

In Table 2, data about the multi-torus structure for the full scale installation from Winsvold 2018 and Sigstad 2019 is listed. The corresponding model scale data is listed for a 1:10.67 scale. The 1:10.67 is the theoretical data for the model, but as shall be seen later, the actual data for the model turned out to differ somewhat from the theoretical values.

Specifically, the values that differ in the actual model from the theoretical values in Table 2 are the torus mass per unit length. This linear mass was minimized in order to make the

Table 2: Model scale data scaled from full scale values, using the scaling laws.

Data description	Full scale	Model scale (1:10.67)
Distance between torus centres	5 m	0.47 m
Torus cross section diameter	1.6 m	0.15 m
Torus mass per unit length	642.5 kg/m	5.5 kg/m
Torus bending stiffness	$2.65 \cdot 10^8$ Nm^2	1869.4 Nm^2
Mooring line spring stiffness	35.9 kN/m	307.6 N/m
Truss spring stiffness	148.4 kN/m	1271.7 N/m
Solar panel load	40 kg/m^2	3.66 kg/m^2

draft of the actual model as small as possible, to make the floaters follow the waves as much as possible. Additionally, the model scale torus bending stiffness in the actual (2D) model is far higher than stated in the table because of the 2D consideration. The plexiglass cylinder was very stiff, which was necessary to properly increase the tension uniformly over the rectangular solar deck. In other words, the torus bending stiffness is not applicable to the actual model produced in this thesis. At last, the mooring lines and trusses between the toruses were not included in this thesis. The only member between the cylinders in this thesis is the solar deck, and the force applied in the tests is not representative for the force in the trusses in an actual multi-torus structure.

There were installed springs on each side of the model, as can be seen later in Figure 4.3. The spring stiffnesses were measured before the model tests to be about 170 N/m each. However, as will be seen later in Figure 6.2, the springs were severely deformed and permanently elongated, so this spring stiffness was not constant during the model tests.

4.2.1 Resulting components used in the model

Since a fitting cylinder for the sought scale and mass was located, this cylinder was chosen in order to save time. The dimensions in the model produced in this thesis differing in scale from the data given in Winsvold 2018 and Sigstad 2019 is not considered a significant issue, as the data about the multi-torus structure in these works is most likely not representative of what the dimensions would be in a full scale installation, because of the multi-torus being conceptually studied. The parts used and the actual masses of these are listed in the following.

- A 1.8 meter long plexiglass hollow cylinder with a mass of 6.73 kg is used. Linear mass is then $\frac{6.73kg}{1.8m}$ = 3.7 kg/m. This was cut in half, resulting in two cylinders of length 0.9 m.
- Solar deck or net with plates representing solar panels has a total measured mass of 1.665 kg. Theoretical solar panel load is 3.66 $kg/m^2 \cdot 0.9m \cdot 0.5m$ = 1.647 kg. There is therefore good agreement between the actual and the theoretically desired mass of the solar deck.
- Tri-foot or split-line rods on both sides of the model has a total mass of 0.125 kg.

- Qualisys orbs and accelerometers have an (unmeasured) approximated mass of 0.2 kg in total.

Ideally, the length of each cylinder should have been 1.5-2 times longer, in order to minimize the errors associated with hydrodynamic end effects at the cylinder end. The split-line rods have some small but unmeasured bending stiffness and were used for preventing roll motion for the cylinders. These rods are normally used as welding rods. As can be seen later, they proved to be not robust enough to withstand the cyclic wave loads, resulting in fatigue and snapping. The resulting actual masses of the components used for the model are listed in Table 3.

Table 3: Actual masses of the various components included in the model.

Mass description	Total mass value
Cylinder mass	6.73 kg
Solar panels with net	1.665 kg
Trifoot rods	0.125 kg
Qualisys orbs and accelerometers	0.2 kg
Total	$\approx$ 8.72 kg

To summarize the difference between the theoretical and the actual mass of the solar deck, the actual measured mass of 1.665 kg corresponds to a $1.665kg \cdot \frac{1}{0.5m \cdot 0.9m} = 3.7$ kg/m^2. This is quite close to the theoretical scaled value of 3.66 kg/m^2. The other way around, the theoretical scaled value 3.66 kg/m^2 corresponds to $3.66kg/m^2 \cdot 0.5m \cdot 0.9m$ = 1.647kg. The linear density for a 0.9 meter wide strip as in the case for the model, is $3.7kg/m^2 \cdot 0.9m$ or $3.66kg/m^2 \cdot 0.9m$, which are both roughly 3.3 kg/m. This is the value used when calculating model-specific parameters like the sag or the eigenfrequency from the string equations.

4.3 Setup

A first sketch of the model layout was made in the drawing program Rhinoceros, and was sent to Trond Innset. Physical solutions for implementing the model could then be found using the vast experience in model making of the model constructing team.

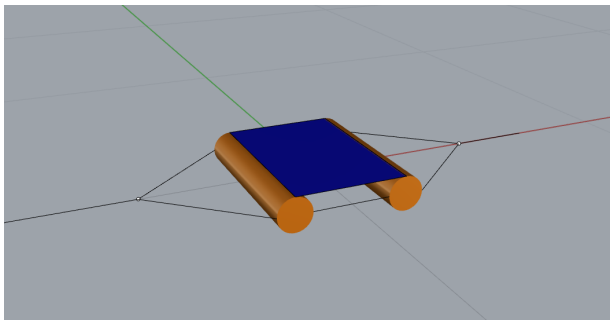

Figure 4.1: First sketch of the model layout, drawn in the program Rhinoceros. This model was sent to Trond Innset, who proposed solutions to physically realize the model. At first, it was proposed to have some truss-like member in between the cylinders near the ends, and the tension being applied in line with the center of the cylinder. However, this was abandoned as the moment and rotations the solar deck would cause on the cylinders, was further discussed.

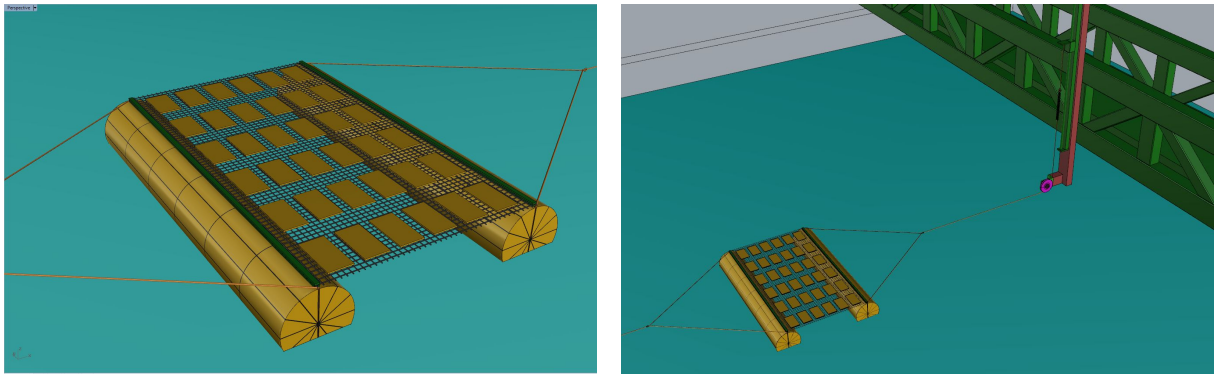

Figure 4.2: The model layout proposal drawn in the program Rhinoceros. This was drawn by Trond Innset.

A preliminary Rhinoceros drawing of the setup is shown in Figure 4.2. It should be noted that the number of solar panels have been changed in the resulting physical model. In this model, there were seven solar panels along the cylinder axis, and five rows along the tension direction

The actuator that would have represented one step closer to a closed-loop system is shown to the right in Figure 4.2. However, this actuator was not included in the model test as the actuators available at the lab were not strong enough to statically hold 35 N. It was envisioned to test tension levels of 10 N to at least 50 N, and possibly up, so the actuator would not have been able to hold these tension levels. This, and some alternatives is discussed in Tillegg C. The setup therefore resultingly included a manual hoist crane. The general layout of the model in the model tank is shown in Figure 4.3.

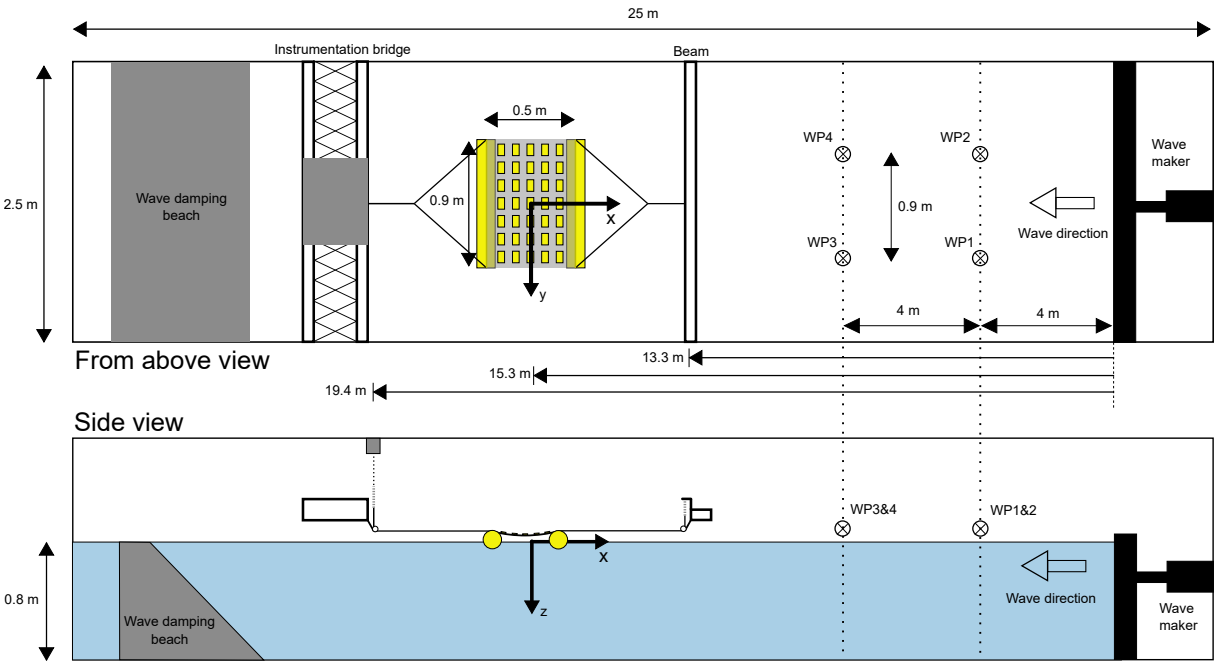

Figure 4.3: View of the setup from above and from the side. The coordinate system follows the coordinate system convention from the Oqus cameras. The lengths in the figure are up to scale relative to each other. The figure layout is inspired by the corresponding figure from Sigstad 2019.

The distance from the wave maker to the model shown in Figure 4.3 is not constant. This distance increases with increased tension due to the winching action only taking place on one side of the model in this setup. This is treated further in Section 5.

4.4 Instrumentation

For motion capturing and consequent FFT algorithm performing, reflective Qualisys motions tracking orbs were mounted on the model. These reflect the light, so that four Oqus cameras ccould calculate the position of each orb. Because the positions of each orb is calculated based on the light reflection off of each orb, the cameras are sensitive to other light reflections. This may cause the cameras to confuse other light reflections with the orbs, causing the position measurement to be lost. In order to prevent the model itself reflecting light, it is painted with a matte paint. The model and motion tracking orbs are shown in Figure 4.4.

Because of the solar deck motion being assumed to mainly consist of first mode string vibration, the measurements at the middle of the solar deck were important. The front marker 4 was used for FFT purposes, as this marker was in the middle of the cylinder and met the incoming waves first. Marker 7 was in the middle of the solar deck, expected to experience the most vertical motion. Also, it was of particular interest to measure the motion of marker 10 at the middle of the aft cylinder because of hydrodynamic couplings between the cylinders. The most important markers were therefore number 4, 7, and 10.

As mentioned, the split-lines consisted of welding rods placed into a slit on the sides of

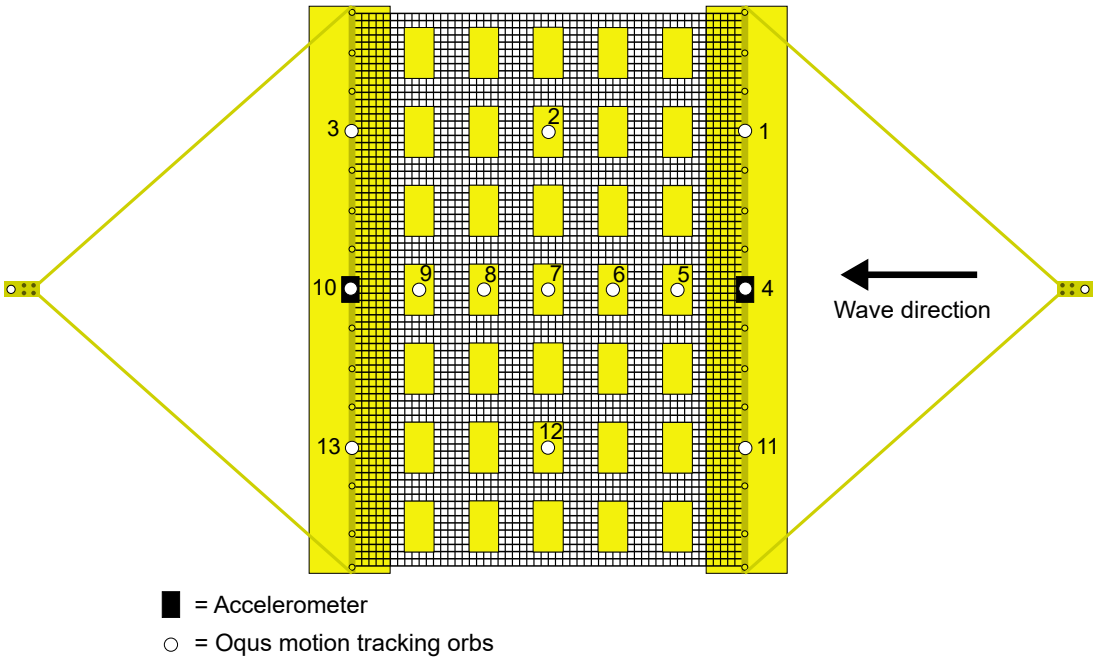

Figure 4.4: View of the model from above, with accelerometers at the mid-point of the cylinders, and Qualisys tracking orbs or markers at specified positions on the cylinders and the deck. The markers are numbered 1 through 13, as shown.

each cylinder. The rods were then bent 90 degrees over the top of the cylinder, and were then fixed to each other using two plates fastened to each other using screws, as shown in Figure 4.4. The mooring or tension line was connected to these two plates, connecting the mooring lines to the split-line rods and the model.

It was believed that the 90 degree bend in the welding rods would be able to withstand much of the moment induced from the waves, preventing roll motion of the cylinders. This proved to be a wrong assumption for waves with period 1-1.5 s, and after some days of testing the model, one of the welding rods snapped in the 90 degree bend from fatigue. After this, the model was repaired, and additional stiffeners around the 90 degree bend was added. This is discussed further in the appendices. The 90 degree bend in the split line rod and a side view of the model is shown in Figure 4.5.

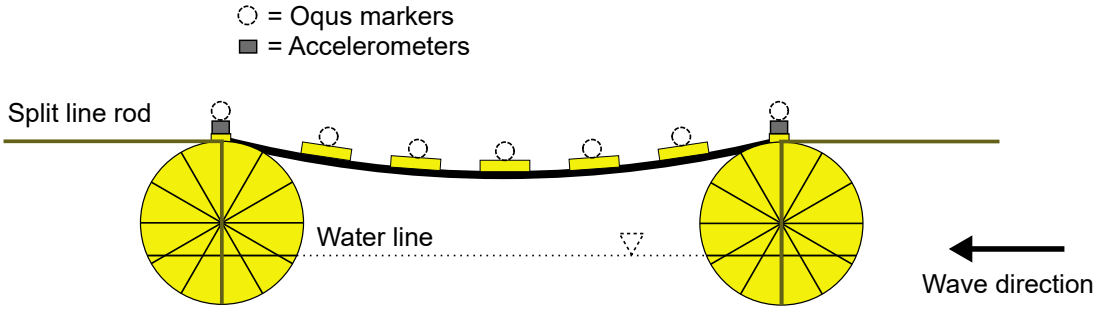

Figure 4.5: View of the model from the side. Oqus markers 4 and 10 were mounted on top of the accelerometers, which meant that the actual vertical position of these markers were 2 cm lower, as the accelerometers were 2 cm tall.

The mooring or winching lines connected to each side of the model were lead into identical

pulley systems, so that the springs could be mounted vertically and away from the water. The pulleys used were pulleys used on sailboats, so they were somewhat resistant to corrosion and resulted in small mechanical force losses. Tension changes were made on the backmost side of the model, as shown in Figure 4.6.

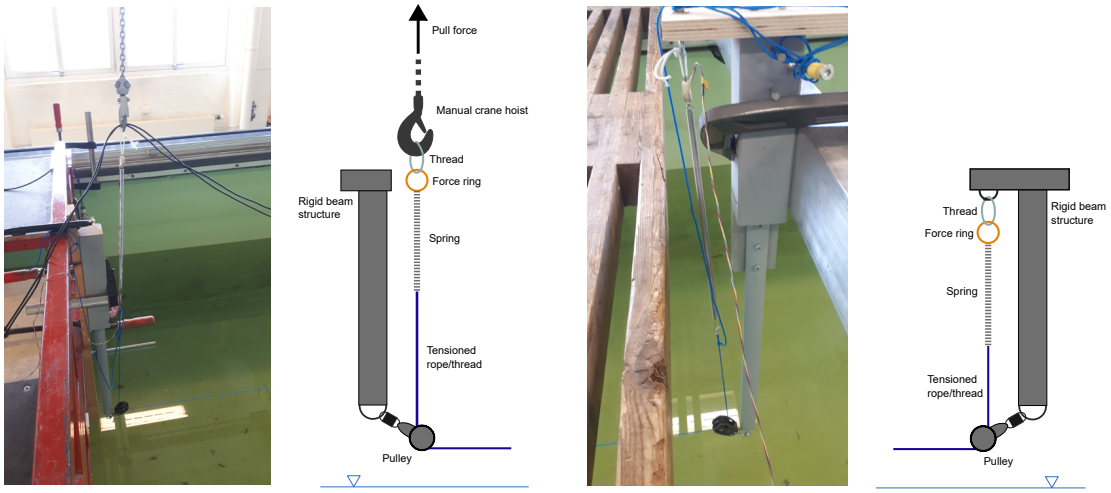

Figure 4.6: Actual and schematic illustration of the foremost and backmost pulley system on each side of the model. Increased tension was applied at the backmost end.

4.5 Test runs

The model tests that were planned to be executed, were in regular waves. The plan was for resonance mapping purposes to vary to parameters, tension and regular wave period. The wave maker proved to produce transverse sloshing phenomenons for regular wave periods below 0.4 s, so this will be the lowest period tested. From the parabola simplification of the freely hanging deck in Equation 2.3, the minimum tension for the solar deck to just touch the water is 10 N, so this will be the lowest tension tested. The highest tension to be tested was supposed to be up towards 100 N, but this proved to be straining on the springs in the model setup and was difficult to achieve because of the springs creeping. For mapping purposes, the max tension was therefore set to 50 N, which was a round number to stop at. The test matrix for mapping purposes is shown in Table 4. The period and amplitude are the period and amplitude commanded to the wave maker, which does not necessarily result in the actual period or amplitude specified.

For the purposes of testing the assumed most vibration inducing wave period, the test matrix in Table 5 was planned. This regular wave period was found from Equation 2.32 to be 0.566 seconds. For testing this wave period the tension was supposed to be tested to the extreme levels of above 50 N. This was abandoned when tension levels of 60 was reached, and at that point it seemed that hoisting the crane further did not increase tension a lot, mainly just elongating the spring permanently.

Table 4: Wave data for the test runs in regular waves, with the intent to map the response for various regular wave periods and tension levels.

Test name	Period [s]	Wave height [m]	Tension [N]
T04N1050	0.4	0.01	10:5:50
T05N1050	0.5	0.01	10:5:50
T06N1050	0.6	0.01	10:5:50
T07N1050	0.7	0.01	10:5:50
T08N1050	0.8	0.01	10:5:50
T09N1050	0.9	0.01	10:5:50
T10N1050	1.0	0.01	10:5:50
T11N1050	1.1	0.01	10:5:50
T12N1050	1.2	0.01	10:5:50
T13N1050	1.3	0.01	10:5:50
T14N1050	1.4	0.01	10:5:50
T15N1050	1.5	0.01	10:5:50

Table 5: Wave data for the test runs in regular waves with period T = 0.566 s. This was the regular wave period assumed to create the largest solar deck responses.

Test name	Period [s]	Wave height [m]	Tension [N]
T0566N5	0.566	0.015	5
T0566N10	0.566	0.015	10
T0566N15	0.566	0.015	15
T0566N20	0.566	0.015	20
T0566N25	0.566	0.015	25
T0566N30	0.566	0.015	30
T0566N35	0.566	0.015	35
T0566N40	0.566	0.015	40
T0566N45	0.566	0.015	45
T0566N50	0.566	0.015	50
T0566N55	0.566	0.015	55
T0566N60	0.566	0.015	60
T0566N63	0.566	0.015	63

Other tests that were planned for FFT performing purposes, were varying the sampling rate of the FFT algorithm with the wave period and the tension level. The corresponding test matrix is shown in Table 6.

Additional tests that were not planned, but were done regardless, were some tests done in irregular waves. This was done for testing how the FFT algorithm would perform when the sea state consisted of several superimposed regular waves. The peak period was tested for three variations, and the tension was tested in two different levels, while the FFT sampling rate was held constant at 20 Hz. The significant wave height was also held constant at 0.01 m. The test matrix is shown in Table 7.

Table 6: Wave data for the test runs in regular waves with period T = 0.5, 1.0, and 1.5 s for FFT performing purposes. Tests done for two tension levels, 25 N and 45 N, and for two FFT sampling rates of 10 Hz and 50 Hz.

Test name	Period [s]	Wave height [m]	Tension [N]	Sampl. rate [Hz]
T05N25FFT	0.5	0.02	25	10
T05N45FFT	0.5	0.02	45	10
T05N25FFT2	0.5	0.02	25	50
T05N45FFT2	0.5	0.02	45	50
T1N25FFT	1.0	0.02	25	10
T1N45FFT	1.0	0.02	45	10
T1N25FFT2	1.0	0.02	25	50
T1N45FFT2	1.0	0.02	45	50
T15N25FFT	1.5	0.02	25	10
T15N45FFT	1.5	0.02	45	10
T15N25FFT2	1.5	0.02	25	50
T15N45FFT2	1.5	0.02	45	50

Table 7: Wave data for the test runs in irregular waves with peak period T = 0.5, 1.0, and 1.5 s. Tests done for two tension levels, 20 N and 35 N, but for one FFT sampling rate of 20 Hz. The irregular waves were made with a Jonswap spectrum with peakness of 3.

Test name	Peak period [s]	Wave height [m]	Tension [N]	FFT sampling rate [Hz]
JT05N20FFT	0.5	0.01	20	20
JT05N35FFT	0.5	0.01	35	20
JT1N20FFT	1.0	0.01	20	20
JT1N35FFT	1.0	0.01	35	20
JT15N20FFT	1.5	0.01	20	20
JT15N35FFT	1.5	0.01	35	20

4.6 Test procedures and post-processing of data

There are many types of data measured during the model tests. Data concerning the force in each force ring, 3D position of each marker, 3D accelerations from the accelerometers, water level measured by the wave probes, temperature from a thermometer, and the flap position of the wave maker are all recorded into .bin files. These files are unreadable by most plotting programs, so the recorded data contained within the .bin files are obtained using the matlab function $catman_read.m$ provided by Trygve Kristiansen.

The Qualisys marker positions are the data sets used the most in post-processing in this thesis. These data sets are used in post-processing to plot the static configuration of the solar deck, and to indicate the motion of the markers during wave testing by computing the standard deviation of the marker motion in one spacial direction. Position data for the markers was also available as a stream of data in real-time. The FFT algorithm was therefore run on this real-time stream of data.

As shown in Table 4, the tension was a parameter to be varied with various wave periods. For wave periods $T \geq 0.6$ s, the tension was changed while the wave maker was running. For $T \leq 0.5$, this introduced extra accelerations into the basin, resulting in unwanted effects like transverse sloshing, as shown in Figure 4.7. Changes in tension was applied only at one end of the model, making it accelerate and likely contributing to the transverse sloshing phenomenon. For T = 0.4 s and T = 0.5 s, various tension and wave frequency combinations were therefore tested in initially still water.

Figure 4.7: Transverse sloshing in the wave tank observed for wave periods T $\leq$ 0.5, amplified or triggered by changing the tension in the solar deck while the wave maker was running, introducing additional waves in the tank basin.

Since the tension was changed while the wave maker was running for $T \geq 0.6$ s, each tension level was held for roughly 30-40 seconds in order to let the model enter a steady or static state in the waves. The time waited was not always the same. For processing the data, each wave test therefore had to be manually processed. This meant that a range where steady state was assumed to be achieved for each tension level was manually noted. From this noted range, standard deviations and other metrics could be calculated for the given tension level. This can be seen in Figure 4.8.

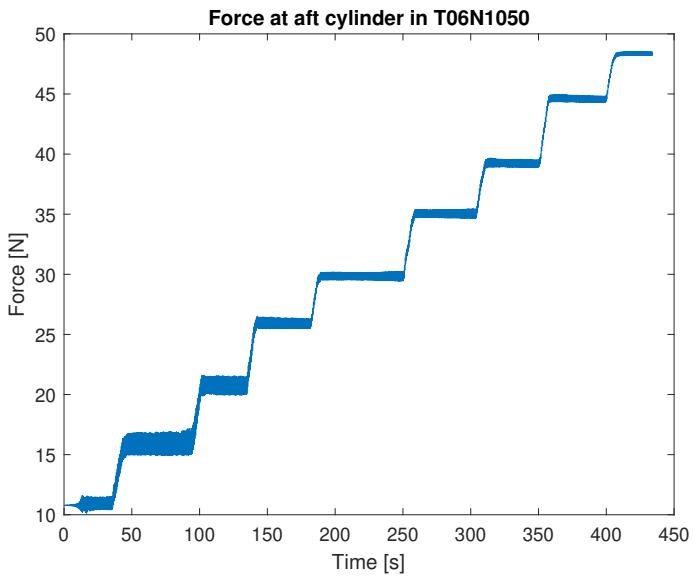

Figure 4.8: Tension incremented in the model test of T06N1050. The model quickly settled into a static state with the incoming waves.

When the tension was changed while the wave maker was running, the tension was always increased. This means that the lowest tension level was the tension level first introduced, and from here the tension was only increased. When changing the tension during the model tests, the actual value of the tension could be read live from the computer running the testing software (Although reading the force on screen live was possible, receiving it as a stream of data was not possible, so feedback on tension was not possible to implement in a closed-loop control system for the model). However, the computer was physically located some distance away from the hoisting mechanism used for changing the tension. This meant that reaching a decently accurate actual tension level in relation to the sought tension level would require going back and forth to the computer screen to check if the applied tension was near the sought level. This resulted in a calibration stick being implemented, where the vertical position of the crane hoist was marked on the stick for various tension levels. The calibration stick is shown in Figure 4.9. Throughout the duration of the model testing, this calibration stick had to be moved upwards because of the springs experiencing creeping.

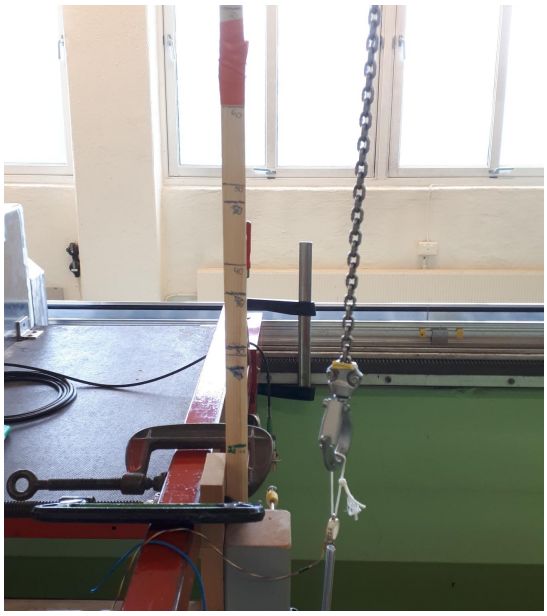

Figure 4.9: The tension calibration stick was implemented in order to quickly reach the desired tension levels. It represents an error source, as the applied tension level was not always exactly equal to the the desired tension level.

4.7 Theory applied to the model

4.7.1 String vibration

From Section 2, Equation 2.5 gives the eigenfrequency for a string with tension. Using data from Table 3, the values from the string vibration equation becomes L = 0.5 m (assumed roughly constant regardless of tension level), and linear mass m = 3.3 kg/m. A tension of 20 N then gives the calculation in Equation 4.1 for the first mode, n = 1.

$$\omega_{0,1} = \omega_{0,n} = \frac{n\pi}{l}\sqrt{\frac{T}{m}} = \frac{1 \cdot \pi}{0.5\,m}\sqrt{\frac{20\,N}{3.3\,kg/m}} = 15.5\,s^{-1} = \frac{2\pi}{15.5\,s^{-1}} = 0.41\,s \tag{4.1}$$

This is period was barely achievable by the wave maker in the lab, capable of producing regular waves with period 0.3-3 seconds. Trygve Kristiansen confirmed that wave periods below 0.5 seconds are generally deemed difficult to generate in wave tanks because of how fast the wave maker will have to move to create these types of waves. This fast movement can cause unwanted effects like sloshing in the transverse direction. Results obtained for these high frequent waves are therefore not as reliable as results obtained from longer wave periods.

4.7.2 Parabola equation

A draft of 0.05 m, which is one third of the cylinder diameter, was decided a fitting draft for the model. This draft results in a maximum sag of the solar deck of roughly 0.1 m before the solar deck touches the water. The corresponding tension according to the parabola equations from Section 2 is calculated in Equation 4.2.

$$S_x = \frac{pL^2}{8f} = \frac{3.3\,kg/m \cdot 9.81\,m/s^2 \cdot (0.5\,m)^2}{8 \cdot 0.1\,m} = 10.1\,N \tag{4.2}$$

Therefore, the solar deck should just barely touch the water surface when the tension is 10 N. As seen in the following results, this was not the case as theory and actual sag behaviour deviated with smaller tension levels.

4.7.3 Discrete mass approximation

The discrete mass and spring model shown in Figure 2.3 consists of discrete masses and springs. To find the appropriate values for the mass, data from Table 3 can be used. The total mass of the solar deck is 1.665 kg, and there are five rows of plates, eaning that each of the discrete masses can be approximated as $\frac{1.66\,kg}{5} = 0.33\,kg$.

The spring stiffnesses are more difficult to assess. From Orcina 2022, the axial stiffness of polyester ropes can be calculated as $1.09 \cdot 10^6 \cdot d^2\,kN$, where d is the diameter of the rope. This value might not be descriptive of a small thread like in the solar deck, as the model is likely fitted for larger rope cross sectional areas. However, this calculation is an approximation. Assuming a diameter of each thread inside the net to be 0.0002 m, the stiffness k becomes is calculated in terms of the axial stiffness from Orcaflex in the following calculation in Equation 4.3.

$$k = \frac{EA}{L} = \frac{1.09 \cdot 10^6\,kN \cdot (0.0002\,m)^2}{0.5\,m} = 87.2\,N/m \tag{4.3}$$

This is only for one thread, but there are 80 threads over the breadth of the solar deck, meaning 87.2 N/m $\cdot$ 80 = 6976 N/m is the approximate stiffness in the solar deck. This fits well with the maximum load tested in Tillegg A, where a load of 50-60 N was needed to break one thread of the net. The deflection was at this point about 0.01 m, although the breaking load includes some plastic deformation, so the deflection at breaking might not be representative for a linear spring deflection. Assuming the thread broke at 60 N, and at 50 N the deflection was 0.01 m, the stiffness is 5000 N/m. This shows that the stiffness of the solar deck is in the order of 1000, so for simulation purposes a stiffness of 5000 N/m is used. As mentioned, the stiffness may be higher because of the plastic deformation in the stretch test and also because of the uncertainty in applying the stiffness formula for such a small cross section. However, as will be discussed in the following results section, there were many actual stiffnesses contributing to the total mass spring system that was the solar deck. Most notably were the stiffnesses of the springs at each side of the model of about 170 N/m each. This means that the unknown actual stiffness to be used for calculating the natural frequency of the motion mode in the middle of the solar deck, is probably lower than the proposed and argumented for stiffness of 5 000 N/m.

5 Results

The model tested in the model tests does not have an exact scale. It is approximately in 1:10 scale of a possible full scale size. Therefore, the results obtained in the model tests will here be given in model scale because of the uncertainty associated with the actual full scale dimensions.

5.1 Theory comparison of deck shape

It was proposed that the shape of the solar deck would take the form of a catenary. However, due to the sag being small compared to the horizontal length of the catenary, it was approximated by a parabola as in Equation 2.3. The x and z values of marker 4 through 10 positions can be extracted from Qualisys Track Manager, to plot the following 2D profiles is Figure 5.1. Marker numbering is given as in Figure 4.4, and in the left figure of Figure 5.1 marker 4 is located at the right end, and marker 10 is located at the left end for all plotted profiles. The figure is plotted for 10 different tension levels, from 5 N to 50 N, with increments 5 N. It can be seen that the model moves horizontally when changing the tension, because of increased tension only being applied on one side of the model. It can also be seen that for low tension levels, there is a small unnatural looking angle by markers 5 and 9. This is likely due to these rows of metal plates are to some degree resting on top of the cylinders for low tension levels.

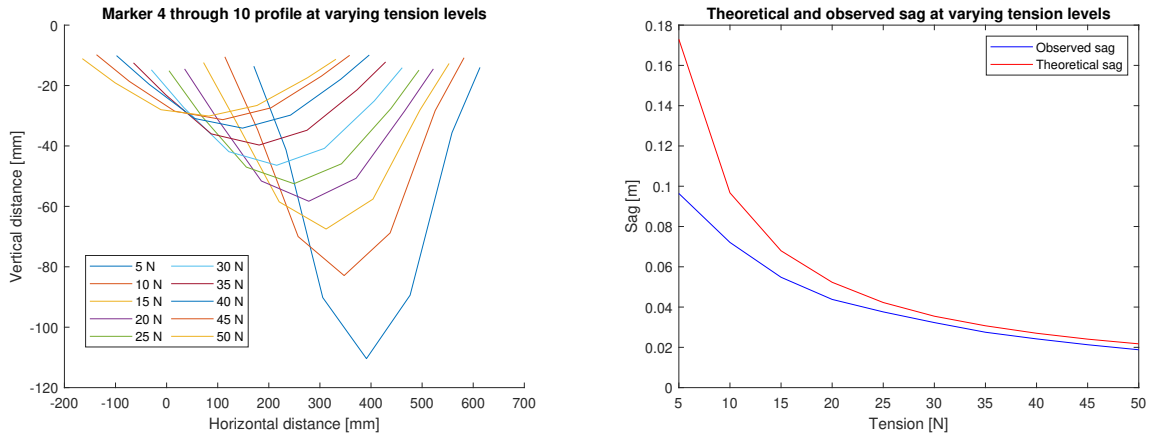

(a) (b)

Figure 5.1: 2D profiles and comparison of theoretical parabola predicted and actual sag in the solar deck for various tension levels. The parabola simplification predicted a sag of 0.1 m at 10 N, which can be seen in the figure to not be quite accurate as the observed sag is 0.1 m for approximately 5 N tension.

5.2 Theoretical natural frequency of the solar deck

Calculating the natural frequency of the solar deck is necessary so that the control logic can assess the likelihood of resonant vibrations. The natural frequency of the solar deck is calculated from Equation 2.5 in Section 2. The natural frequency of the higher fidelity discrete mass spring model shown in Figure 2.3, is calculated by Equation 2.22. The result is shown in Figure 5.2.

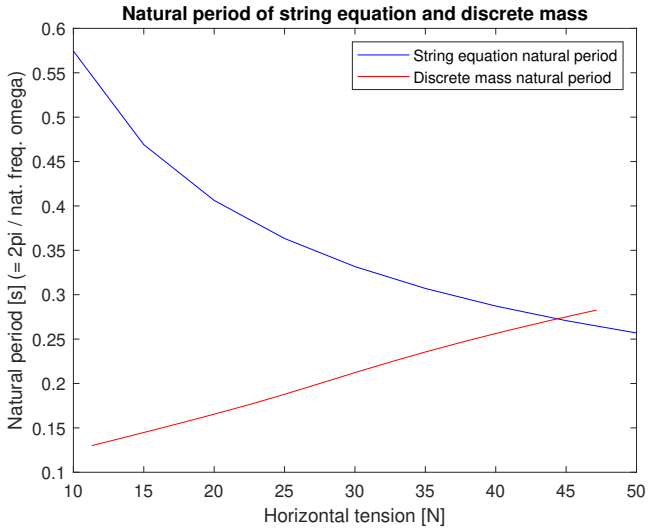

Figure 5.2: Theoretical natural period of the string equation and the discrete mass model as functions of tension level.

It can be seen from Figure 5.2 that for the string equation, the natural period decreases and therefore the natural frequency increases for increasing tension levels. This is expected for members with axial tension. However, for the discrete mass model, the inverse of this relation seems to be the case. This is not physical, as a higher tension should lead to a higher frequency of natural oscillation, as in the string equation.

5.3 Mapping the structure response by varying the deck tension and the regular wave period

For experimentally locating responses from combinations of regular wave periods and solar deck tension levels, a series of wave periods was tested where the tension was changed during testing. The regular wave periods mapped ranged from 0.4 seconds to 1.5 seconds with an increment of 0.1 seconds. The tension tested ranged from 10 N to 50 N with an increment of 5 N. The lowest tension 10 N was included because of the parabola simplified equations from Section 2 showed that the solar deck would just touch the water at a tension of about 10 N, so this was an interesting case to be included. The top level tension of 50 N is a bit arbitrary, and does not represent possible values for the tension in full scale. However in the model tests, 50 N was deemed a tension value corresponding to absolute maximum values in full scale. The tension was not increased beyond this level, because of the concern that this would severely affect the ability of the model to follow the wave motion because of the mooring setup. There were also some considerations with the springs used for the mooring setup. These springs were held at high tensions for a considerable amount of time, so creeping was present. Spring creeping is the nonlinear phenomenon of a spring experiencing plastic deformation, permanently elongating the length of the spring at which there is zero force through it. So in order to constrain the extent of this phenomenon, a max tension level was set at 50 N.

In Figure 5.3 the standard deviation of the vertical position of marker 4 and 10 is plotted as a function of the tension levels and regular wave periods tested. Marker 1, 3, 11, and 13 are not included because it is assumed that these will be much the same as the measurements at the middle of the cylinder they are placed on. Measurements of marker 4, 7, and 10 vertical positions are the measurements of the most interest. This is because they are measures of the how well the cylinders follow the waves in heave, and the degree to which first mode 2D vibration in the solar deck happens.

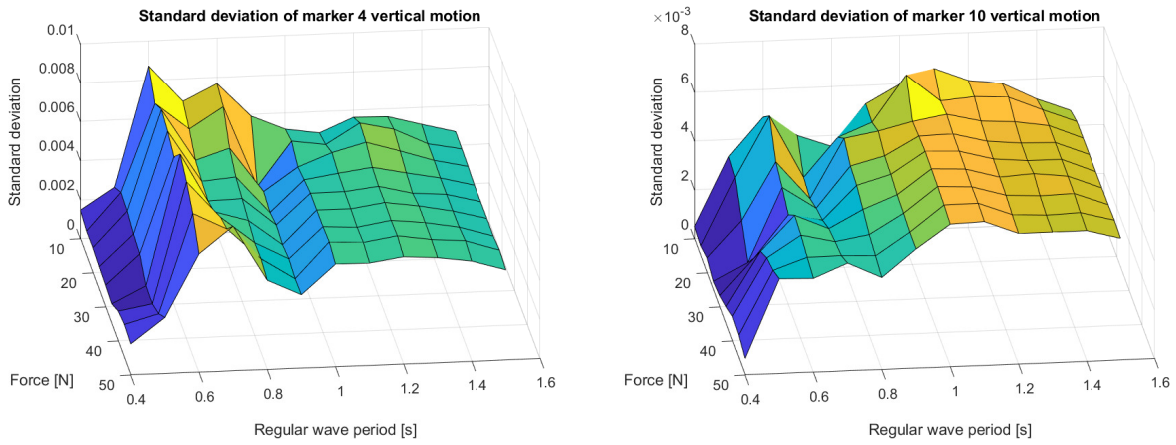

Figure 5.3: Surface plots of standard deviation of marker 4 and 10 vertical motion as function of small scale regular wave period and small scale tension level.

In Figure 5.4 the standard deviation of the vertical position of marker 5 and 9 is plotted as a function of the tension levels and regular wave periods tested. These are the markers next to markers 4 and 10, but one notch closer to the middle. The yellow aluminium plates representing the solar panels these markers are fixed to are somewhat resting on top of the cylinders for low tensions.

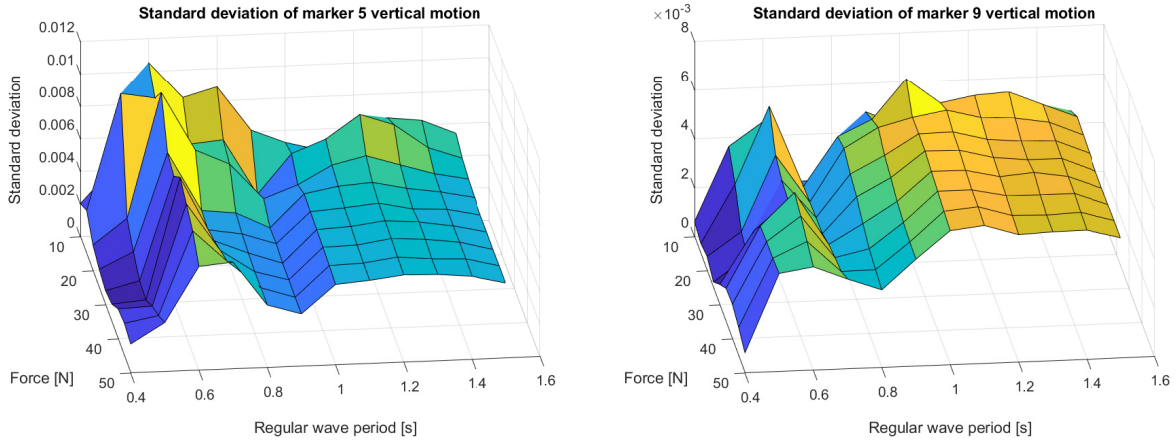

Figure 5.4: Surface plots of standard deviation of marker 5 and 9 vertical motion as function of small scale regular wave period and small scale tension level.

In Figure 5.5 the standard deviation of the vertical position of marker 6 and 8 is plotted as a function of the tension levels and regular wave periods tested. These are the markers the next closest to the middle of the solar deck.

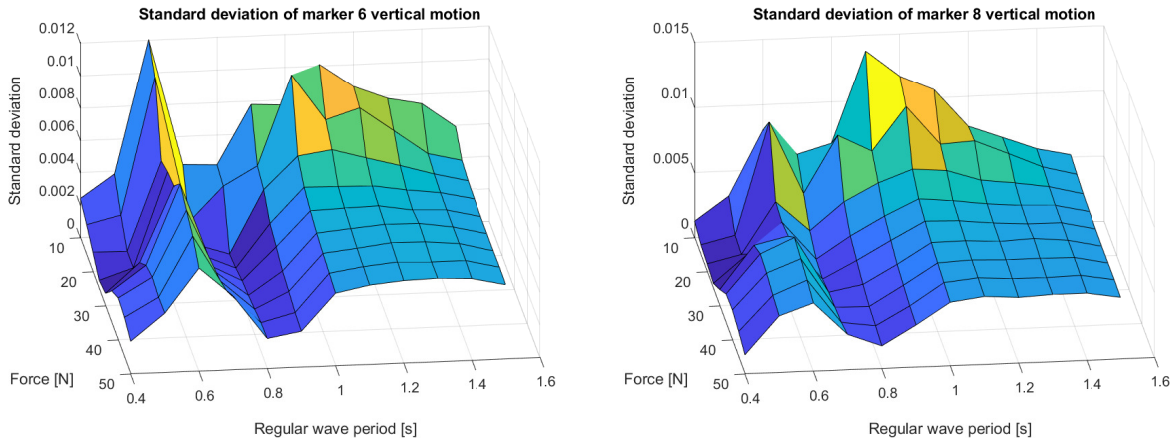

Figure 5.5: Surface plots of standard deviation of marker 6 and 8 vertical motion as function of small scale regular wave period and small scale tension level.

In Figure 5.6 the standard deviation of the vertical position of marker 7 is plotted as a function of the tension levels and regular wave periods tested. This is the marker on the middle of the solar deck, and is believed to have the largest motion amplitudes.

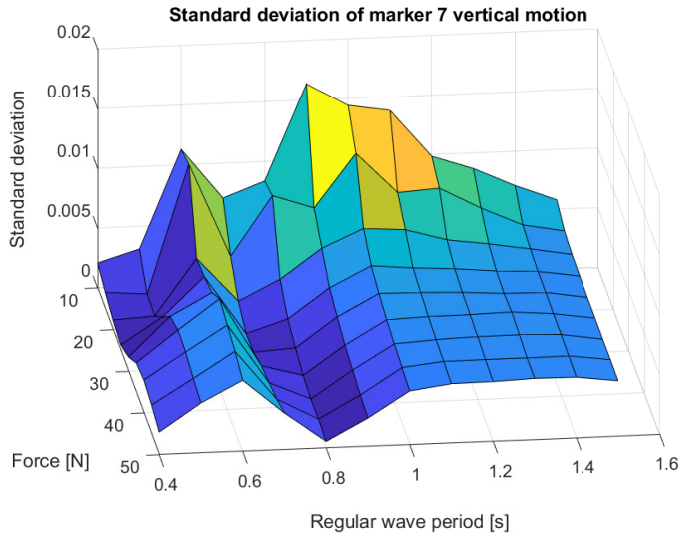

Figure 5.6: Surface plot of the standard deviation of the vertical position of marker 7 as function of small scale regular wave period and small scale tension level.

The vertical motion of marker 4 on the cylinder meeting the waves first is used as a wave estimator for FFT purposes. The vertical motion of this marker can therefore be regarded as a good approximation to the multi-torus structures response in the waves. Meanwhile, the vertical position measurements of marker 7 is the most reliable measurements of the first mode vibration in the solar deck. An RAO from marker 4 to marker 7 can therefore be made by dividing the matrix with standard deviations for marker 7 by the matrix with standard deviations for marker 4 and for marker 10, all in vertical direction. This is shown in Figure 5.7.

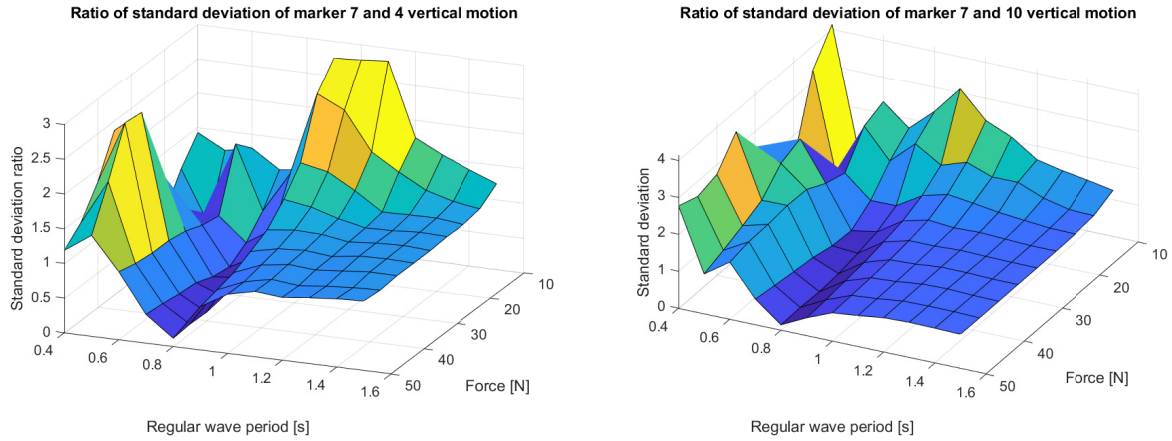

Figure 5.7: Surface plot of the ratio in standard deviation of the vertical position of marker 7 over 4 and 7 over 10 as function of small scale regular wave period and small scale tension level.

The corresponding RAO can be made for the case where the average of the two matrices for marker 4 and 10 is used as the denominator in the fraction. This case is shown in Figure 5.8.

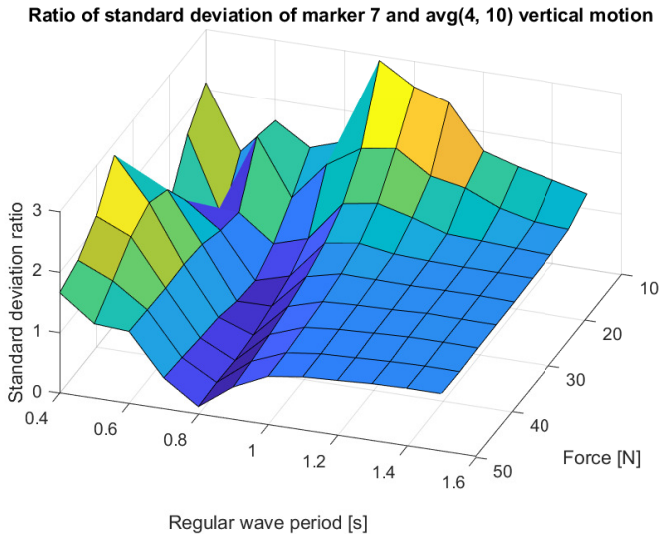

Figure 5.8: Surface plot of the ratio in standard deviation of the vertical position of marker 7 over 10 as function of small scale regular wave period and small scale tension level.

These are the vertical standard deviations, but the horizontal motion along the x-axis (in-line force direction) is also of interest. If these motions on the cylinders are large, it suggests that some of the vertical motion seen in the solar deck is due to changes in the distance between the cylinders, resulting in a change in the static configuration of the freely hanging solar deck, in other words a quasi-dynamic or possibly dynamic horizontal excitation mode of the solar deck ends. In Figure 5.9 the standard deviation of the horizontal position of marker 4 and 10 is plotted as a function of the tension levels and regular wave periods tested. Horizontal motion is present for low tension levels and the largest wave periods.

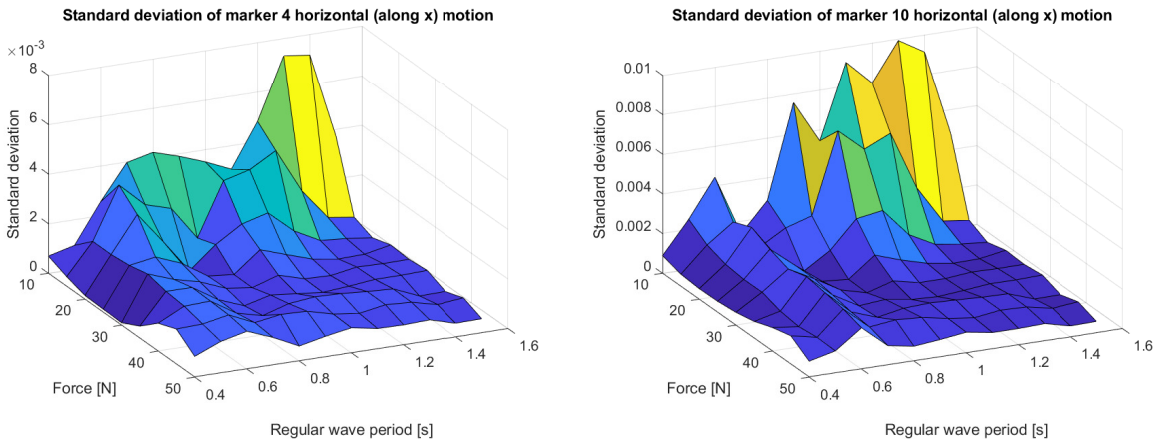

Figure 5.9: Surface plots of standard deviation of marker 4 and 10 horizontal motion as function of small scale regular wave period and small scale tension level.

5.4 Solar deck response in waves with wavelength assumed to be the most solar deck vibration inducing

It was assumed that waves with wavelength equal to the distance between the cylinders would provoke the largest motion amplitudes at the middle of the solar deck. It can be seen from Figure 5.6 that the standard deviation of the vertical motion of marker 7 has a local peak at 0.6 s, which is close to the calculated 0.566 s period. However, this peak is not the largest standard deviation value in Figure 5.6, as there are larger standard deviations for periods around 0.8-1.0 s for the lowest tension of 10 N. At any rate, local peaks are present near the period 0.6 s for all tension levels, meaning some natural frequency has been found at this wave period.

However, this might be because of quasi-dynamic and dynamic motion in the solar deck when the waves make the cylinders move in x-direction towards and away from each other at the same time. In other words, the peak for 10 N tension and 0.9 s period in Figure 5.6 might not be vibrations. This is further backed up by the fact that the peaks at T = 0.6 s are present for all tension levels, while the peak at T = 0.9 s period is only present for the lowest tension levels. This is discussed further in Section 6.

For the tests with a regular wave period of 0.566 s, the tension was supposed to be tested to extreme levels of above 50 N. This was abandoned when tension levels of 63 N was reached, as the spring at the winching end seemed to experience severe creeping at this tension level. The resulting tension levels tested for this period is then from 5 N to 60 N with 5 N increment, with the addition of 63 N. The resulting standard deviation of the vertical motion of marker 4, 7, and 10 is shown in Figure 5.10.

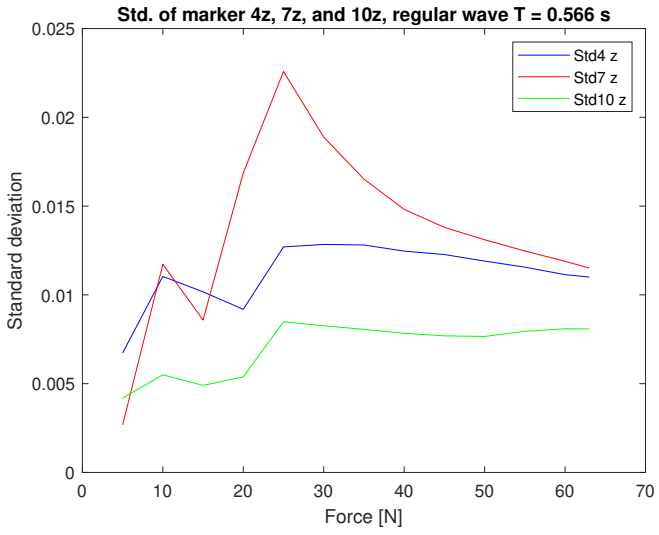

Figure 5.10: Standard deviation of the vertical motion of marker 4, 7, and 10 for T = 0.566s.

For a data type comparison, another data type than the standard deviation extracted from the model tests was the mean height of the motion amplitudes of the markers. This was done by finding all the local maxima and minima in the data for the oscillating positions, and taking the mean of all the maxima and the minima respectively, and taking the

difference between the mean of the maxima values and the mean of the minima values. This data corresponding to the Figure 5.10 is shown below in Figure 5.11. The plots are quite similar, meaning the standard deviation plots are good representations of the relative motion of markers.

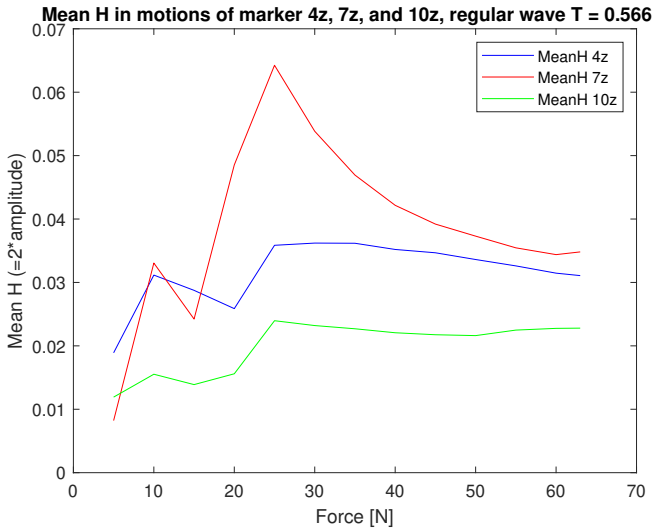

Figure 5.11: Mean height of the vertical motion of marker 4, 7, and 10 for T = 0.566s and H = 0.015 m.

RAOs from marker 4 to 7, and from marker 10 to 7 can be plotted for vertical motions, as shown in the following Figure 5.12. A dynamic amplification factor (DAF) of 1-3 is seen for the RAOs from the front and aft cylinder to the middle of the solar deck.

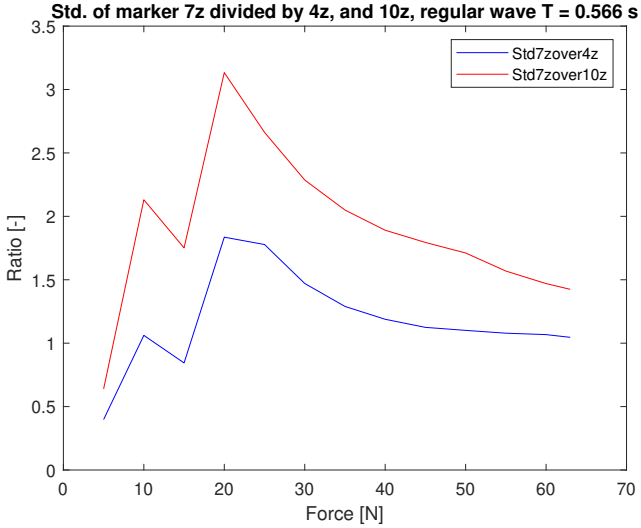

Figure 5.12: Standard deviation of the vertical motion of marker 7 over 4 and 10 respectively, for T = 0.566 s.

An RAO from the average of marker 4 and 10 to marker 7 is shown in Figure 5.13.

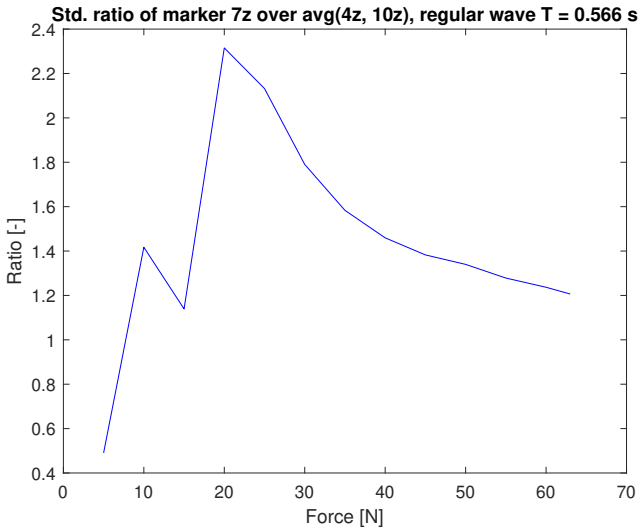

Figure 5.13: Standard deviation of the vertical motion of marker 7 over the average of marker 4 and 10, for T = 0.566 s.

In Figure 5.13, Figure 5.12, Figure 5.11, and Figure 5.10 it can be seen that 20-25 N is critical, and is hence a tension level that should be avoided.

Along the row of motion tracking markers 4 through 10, the standard deviation of the vertical motion for these markers are shown in the following Figure 5.14. Symmetry is observed for the solar deck, as the standard deviations are largely symmetric about the mid point of the deck, marker 7.

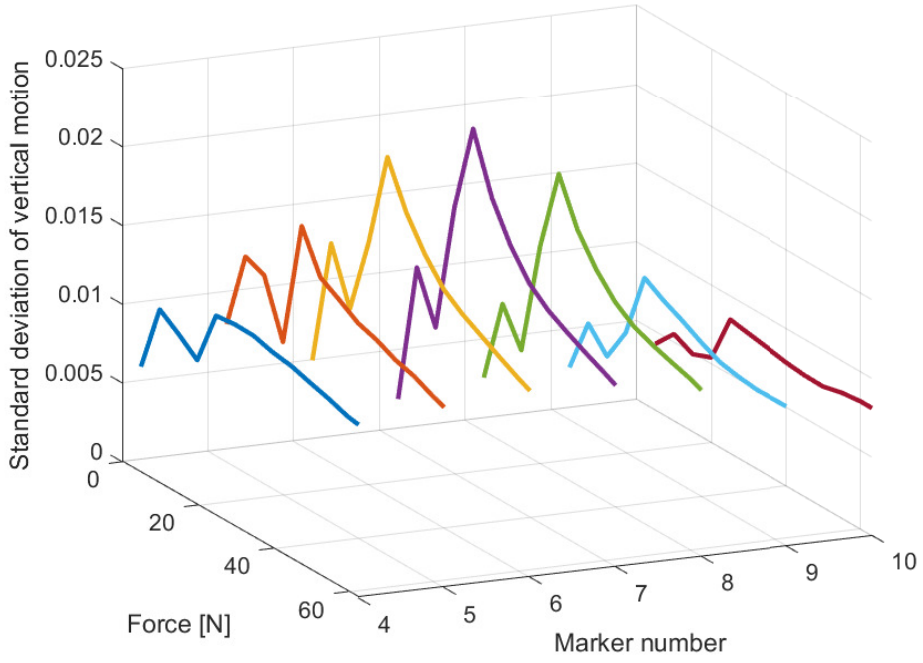

Figure 5.14: Standard deviation of the vertical motion for markers 4 through 10 for T = 0.566s.

A quite interesting phenomenon is here observed when comparing the 2D plots of the standard deviation of marker 7 vertical motion for T = 0.566 s in Figure 5.10 with the isocurves for T = 0.5 s and T = 0.6 s from the surface plot of the standard deviation of the vertical motion of marker 7 vertical motion in Figure 5.6. The comparison plot is shown in Figure 5.15. The difference is big in behaviour for increasing tension levels, which is unexpected because the wave periods are similar. This could have to do with the way tension was increased in the surface plot making tests. In these tests, a constant period propagated towards the model while the tension was increased step wise, and each tension level was held for a duration of 30-50 seconds. This holding time was unfortunately not constant for all tensions. The holding time not being constant, and the action of increasing the tension while waves were propagating towards the model might have caused this difference observed. At the same time, it could be that the solar deck becomes more excited in waves with wavelengths exactly equal to the cylinder distance.

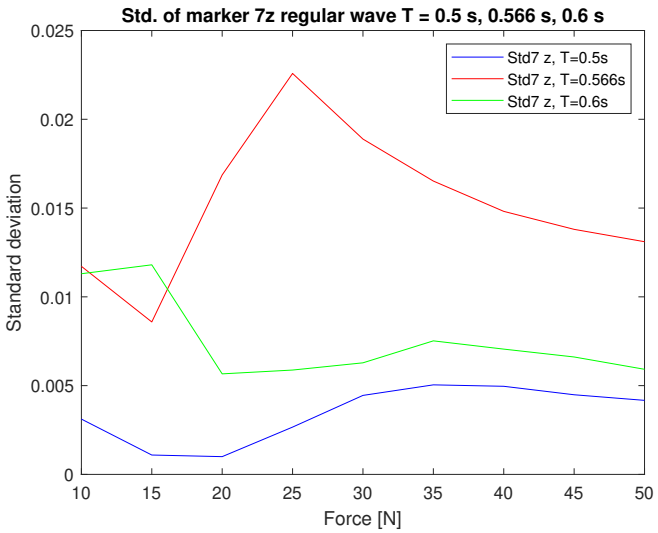

Figure 5.15: Standard deviation of marker 7 vertical motion for T = 0.5 s, T = 0.566 s, and T = 0.6 s. Since T = 0.566 was tested for more tension levels, the tension levels not tested in these tests were not included in this plot.

5.5 Real-time FFT testing

5.5.1 FFT for various sampling rates, regular wave periods, and solar deck tensions

Tests done for 3 regular wave periods: 0.5, 1.0, and 1.5 seconds period. These are tested with the tensions 25 N and 45 N, with 10 Hz and 50 Hz sampling rate for the FFT algorithm. The duration of sampling is held constant, so that the 50 Hz windows contain five times more data points than the 10 Hz windows. The raw data only is plotted in these FFT estimated frequency spectra, and they are not smoothed. The plots are shown in Tillegg D, and discussed later in Section 6.

5.5.2 FFT for irregular waves for various peak periods and tension levels

The FFT algorithm was performed on the motion of the model in three Jonswap wave spectra with peak frequency $T_p = 0.5$ s, 1.0 s, and 1.5 s, and a significant wave height $H_s = 0.01$ m. All three spectra had peakedness $\gamma = 3$, and a duration of 35 s. FFT was performed with a sampling rate of 20 Hz for a duration of 30 s, and the tension levels tested were 20 N and 35 N. FFT was performed on the vertical motion of markers 4, 7, and 10. These results are discussed further in Section 6.

Figure 5.16 shows FFT performed on the vertical motion of the model for a Jonswap wave spectrum with peak frequency $T_p = 0.5$ s, and significant wave height $H_s = 0.01$ m. FFT was done with a sampling rate of 20 Hz for 30 s, and the tension levels were 20 N and 35 N. FFT was performed on marker 4.

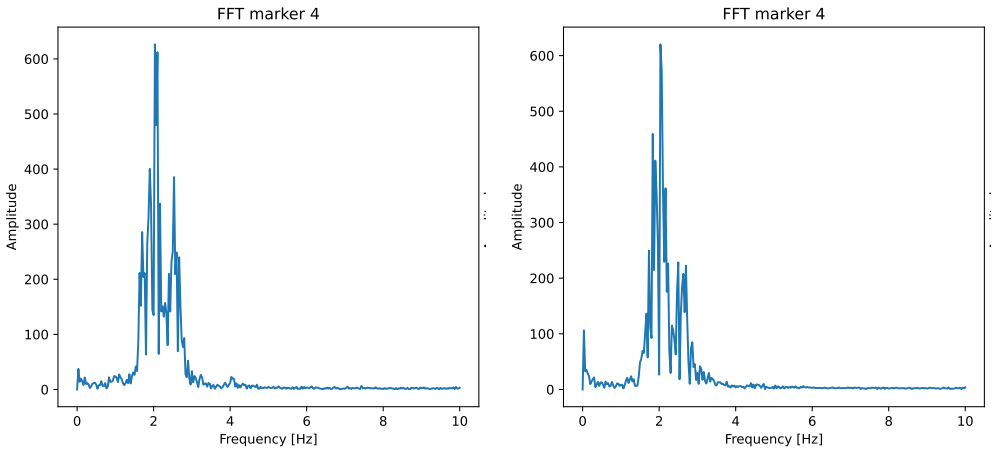

(a) Solar deck tension 20 N. (b) Solar deck tension 35 N

Figure 5.16: FFT for Jonswap spectrum. Tp = 0.5 s, Hs = 0.01 m. (a) Marker 4 max value frequency (at peak) is 2.03 Hz. (b) Marker 4 max value frequency is 2.03 Hz.

Figure 5.17 shows FFT performed on the vertical motion of the model for a Jonswap wave spectrum with peak frequency $T_p = 1.0$ s, and significant wave height $H_s = 0.01$ m. FFT was done with a sampling rate of 20 Hz for 30 s, and the tension levels were 20 N and 35 N. FFT was performed on marker 4.

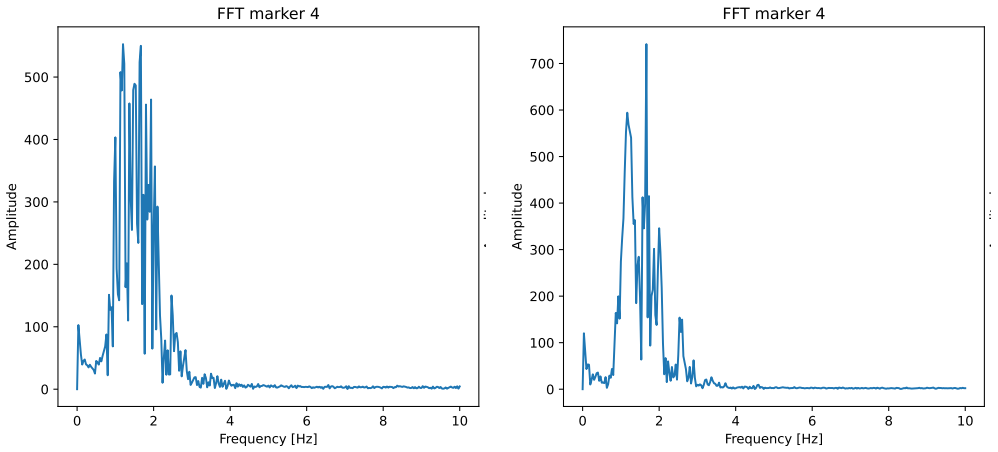

(a) Solar deck tension 20 N (b) Solar deck tension 35 N

Figure 5.17: FFT for Jonswap spectrum. Tp = 1.0 s, Hs = 0.01 m. (a) Max value frequency (at peak) 1.2 Hz for marker 4. (b) Max value frequency (at peak) 1.67 Hz for marker 4.

Figure 5.18 shows FFT performed on the vertical motion of the model for a Jonswap wave spectrum with peak frequency $T_p = 1.5$ s, and significant wave height $H_s = 0.01$ m. FFT was done with a sampling rate of 20 Hz for 30 s, and the tension levels were 20 N and 35 N. FFT was performed on marker 4.

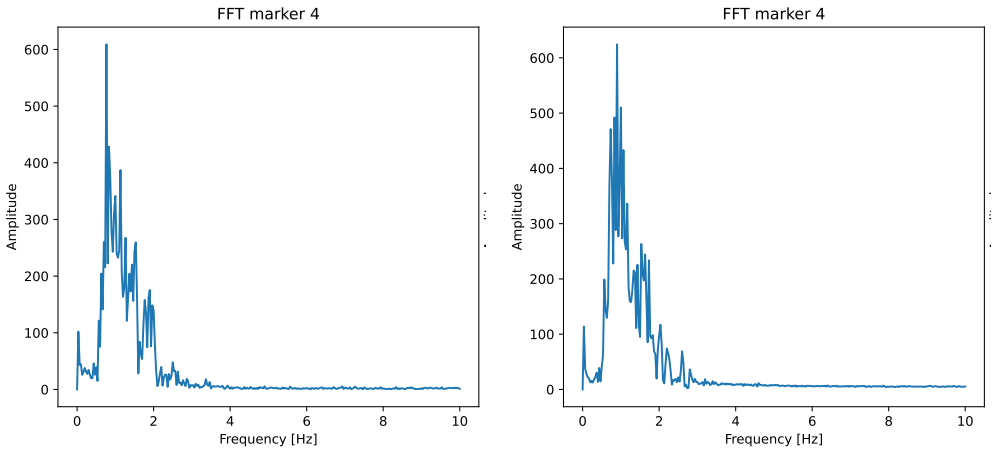

(a) Solar deck tension 20 N (b) Solar deck tension 35 N

Figure 5.18: FFT for Jonswap spectrum. Tp = 1.5 s, Hs = 0.01 m. (a) Max value frequency (at peak) 0.77 Hz for marker 4. (b) Max value frequency (at peak) 0.9 Hz for marker 4.

5.5.3 FFT of vertical acceleration in irregular waves in post processing

Vertical position measurements relative to a fixed reference frame will likely not be possible in a full scale installation. An alternative is therefore performing FFT on acceleration measurements stored. For irregular waves present out at offshore locations, the FFT algorithm may fall short. As shown in Figure 5.19, neither the raw data nor a smoothed frequency spectrum curve is able to locate the peak frequency of 0.67 Hz. This may reduce the functioning level of an actual offshore implementation of the FFT based control system presented in this thesis.

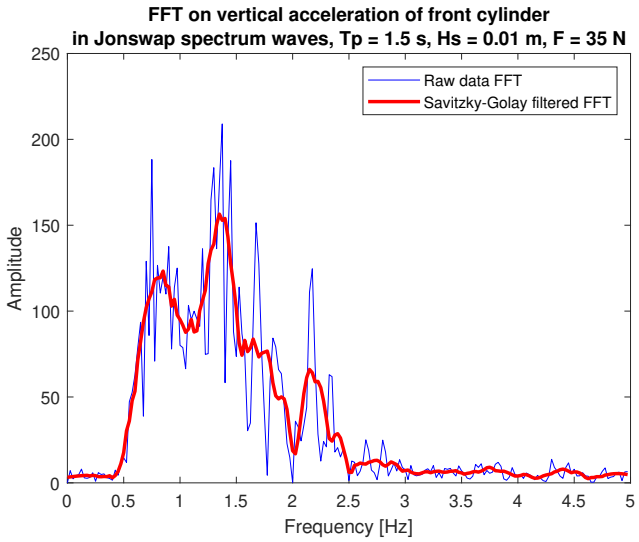

Figure 5.19: Comparing raw and smoothed FFT frequency spectrum in irregular waves with Tp = 1.5 s, Hs = 0.01 m, the same waves as in Figure 5.18, and tension 35 N.

5.6 Instrumentation verification

5.6.1 Variance in measurements

It was of interest to test the variance in the Qualisys marker position measurements in order to assess how biased the measurements were. It can be seen from Figure 5.20 that for practical purposes, there is little deviation as the deviations are in the range of millimeters. The plot still gives a good visualization of the variance in the position measurements dealt with during the model testing in this thesis.

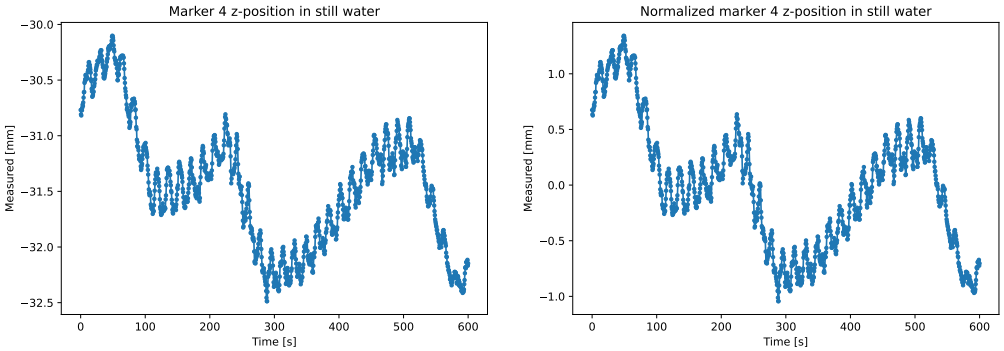

Figure 5.20: Oqus measurements vary in two main ways. They are varying over 10-15 seconds, but also because of water leaking out of the tank and pumps pumping water back in. These two modes of measurement noise contributes to errors in the measurements.

It was found that the measurements of the corner markers, markers 3, 13, 1, and 11 had some unexpected differences in vertical position. From a 1 minute test in still water, the vertical position of all four markers were recorded. It was found from this test that the average difference in vertical position between the two outermost markers (marker 1 and 11) on the foremost cylinder was 11.8 mm. For the two outermost markers (marker 3 and 13) on the backmost cylinder the average difference was 12.7 mm. These are not very big differences, but they indicate that the two cylinders have a slight inclination and asymmetry so that markers 1 and 3 are below markers 11 and 13, or that the Qualisys frame of reference has a small rotation.

5.6.2 Observed phenomenons

Drop in motion amplitudes in wave tank

At around 65 seconds it can be qualitatively seen a slight reduction in the amplitude of the motion in Figure 5.21. It is not known what the reason for this is. A slowly varying water level can also be observed, which is the leaking of water out of the tank, and pumps pumping it back in.

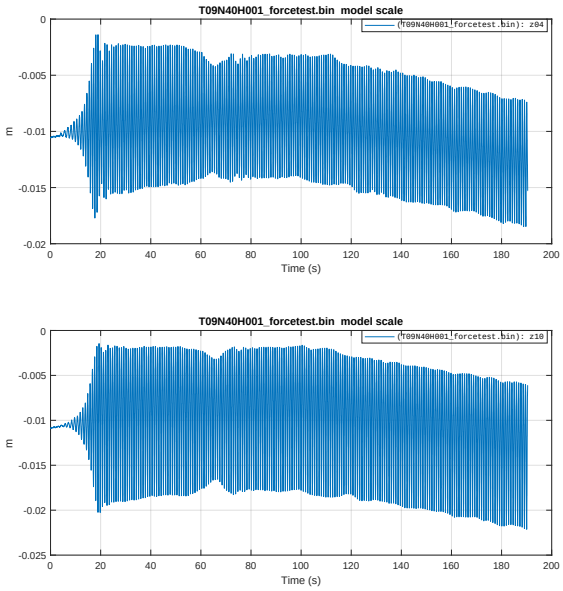

Figure 5.21: Unexplained drop in the amplitude of the vertical motion of the cylinders at around 65 s. Vertical motion for marker 4 and 10, at the fore and aft cylinder in regular waves with T = 0.9 s, and H = 0.01 m.

Force loss through pulley system

It can be qualitatively seen from Figure 5.22 that the tension in the line in front of and behind the model differs. The initial values of 23.6 at the foremost force ring and 26.5 at the backmost force ring show that there are some losses through the pulley system. The differences between the two are greater for small solar deck tension levels (10-20 N), and diminishes for larger tension level (40-50 N). The tension level was therefore increased during the model tests until the average of the two force measurements reached the sought force level. This is a good approximation, as there is one pulley present between each of the force rings and the model. Assuming equal force losses through both of the pulleys, the tension through the model should be the average of the two measurements.

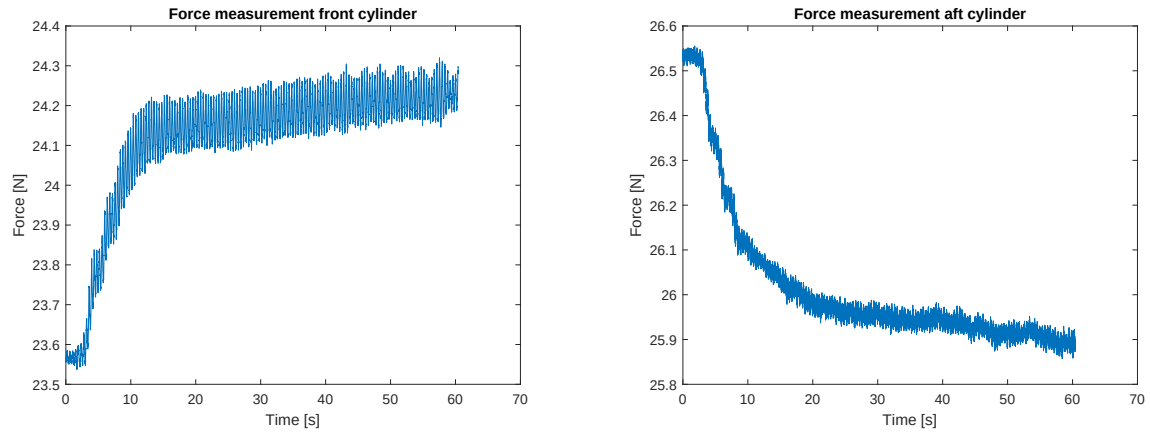

Figure 5.22: Force measurement at the front force ring, and at the aft force ring. Since the force is measured in line with the wave direction, the wave drift forces make the front measurement increase, while the aft measurement decreases.

6 Discussion

In the following, the findings in this thesis are discussed. The discussions are divided into discussion regarding error sources present during the model tests, the theory used to arrive at the results that were presented in Section 5, and the implications of the findings for a full scale installation.

6.1 Error sources in the model tests

6.1.1 The 2D simplified model

There were several error sources present during the model tests. To begin, some of these error sources are attributed to the design behind the model. As mentioned in Section 4, the model was built with main focus on the solar panel carrying deck. Trusses between the cylinder floaters were excluded because of the fact that the tension would propagate through both the solar deck and the trusses in this case. If the trusses were connected to the cylinders at the cross section center height, and the solar deck was connected to the top, this would have created a rotating moment arm equal to the radius of the cylinder. The tension would then have propagated through the solar deck to a higher degree with increased tension levels, causing the cylinder to have some rotation depending on the tension level.

This problem originates from the model consisting of two rigid bodies with no initial connection between them. For several concentric toruses, this problem is not present. In essence, the tension through the solar deck in a 3D multi-torus setup is compensated by the fact that many cylinders carry the solar deck. The radial force from the solar deck at the top of one of the inner toruses is in equilibrium with the force through the solar deck on top of the two neighbouring toruses. However, this is not true for the outermost torus. On this torus, the radial forces through the trusses and the solar deck towards the middle of the island is compensated by only the force through the mooring line and by the stiffness of the torus. Therefore, the model constructed is a decent approximation to the behaviour of the solar deck between the outermost torus and the next torus towards the middle of the structure.

For a full scale installation, it might be that the tension through the solar deck is negligible in comparison with the force through the trusses, and that most of the force propagates through the trusses. Estimates on this issue could quite easily be calculated, but was not done in this thesis, as the solutions to this problem of the 2D simplification was solved by excluding the trusses from the model. In hindsight, a better solution could have been to include some spring connections between the two cylinders. There are some disadvantages to this as well, like affecting the ability of the floaters to follow the waves independently, and affecting the measurements of the solar deck pretension, and waves interacting with the connections. However, for the analysis of only the solar deck, extra floater trusses and connections could have been an option.

There were other issues associated with simplifying the model to 2D. The static force

considerations were discussed in the above, but the dynamics of the simplified model are also topics of discussion. Preventing the cylinders from rotating due to wave forces, when they are (to some extent) prevented from translational motion in x-direction was a challenge. Mechanically, this meant introducing moment stiffness at the top of the cylinders. At first, it was believed that the bending stiffness in the split-line welding rods was enough to absorb the necessary moment. However, as mentioned and treated further in Tillegg B, this was not enough, and one of the rods snapped after cyclic bending fatigue. After this, an additional framework of force absorbing rods around the top of the cylinder was installed. The framework increased the moment stiffness at the connection point at the top of the cylinders satisfyingly.

An additional error source related to a design flaw, was the error associated with the rows of panels the closest to the cylinders. These were to some degree resting on the cylinders for low tension levels as seen in Figure 5.1, which might have effectively reduced the length of the freely hanging solar deck. Reducing the length of the solar deck approximated as a string was seen from Section 3 and Equation 2.5 to be an effective way to change the eigenfrequency. Therefore, this might have had an effect on the standard deviations seen in the surface plot of standard deviations of the vertical marker 7 motion in Figure 5.6 for low tension levels. However, the PV technology resting on top of the toruses is also expected to be seen for a 3d multi-torus structure as well, so it is an acceptable error.

Another design flaw of the model was each cylinder being only 0.9 m long. The breadth of the wave tank is 2.5 m, meaning there was room for longer cylinders. However, the cylinder that was located and used was 1.8 m, and a similar one was not found. This cylinder was chosen to save time, but it could have been an advantage to spend time locating longer cylinders. The shortness of the cylinder can cause some vortex shedding around the cylinder in x-direction. This is not beneficial as the model was assumed to be of a 2D nature, meaning that water flowing around the 2D cross section contradicts this 2D assumption. The shortness of each cylinder therefore represents some contradictions between the actual cylinder behaviour compared to the theory of infinitely long cylinders. Making the cylinders longer, maybe 1-2 m each, would make the effect of vortex shedding smaller in comparison to the mass of the cylinder, making it a closer approximation to an infinitely long cylinder.

The cylinders being flat at the ends may have contributed to vortex shedding because of the sudden change in geometry. From (Pettersen 2018), vortex shedding can cause oscillating lift forces in the direction normal to the incoming waves or flow. This may have contributed to the nonlinear effects observed for regular wave periods $T \leq 0.5$ s, by triggering motion in y-direction, normal to the waves. This was also observed for a long period tested, T = 1.7 s, which was larger than the largest period for the mapping purposes of T 1.5 s. The phenomenon observed here is resonance in y-direction as shown in Figure 6.1.

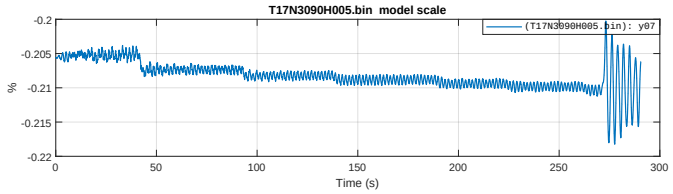

Figure 6.1: Raw data showing resonance in y-direction for a regular wave period T = 1.7 s and tension of 45 N.

6.1.2 Surrounding error sources

There were also error sources associated with the surroundings in the wave tank. These error sources cannot be avoided. These error sources are those noted in Section 5.6, with the Qualisys measurements varying naturally, and with the water level in the water tank. The water level in tank was slowly draining over time, and pumps were supposed to pump water back into the tank. Still, a difference in the average water level of about 4-5 cm was noted from the beginning of the model tests to the end. The tank also being small can result in unexplainable phenomenons like in Figure 5.21. The small dip in this figure could be because of reflected waves. Additionally, the force rings have temperature dependencies, and it is not known if and how much they drift over time, meaning the rings can measure different force values for the same actual force. However, the temperature dependency and drift of the force rings were believed to not be of large significance, and the force measurements were satisfactory. Lastly, the force measurements were influenced by force loss through the pulleys, as seen in Figure 4.3. Also the force measurements are affected by the waves as seen in Figure 5.22.

Wave maker error: This is especially true for low wave frequencies because of the pistons having to move so fast, so they either overshoot the desired max position or they have to start moving the other way before they reach the desired max position. Wave maker making uneven waves / smaller waves when the period is longer. Because for short periods, it does not have time to reach the specified position on time, so it moves jerky and creates bigger waves than it is supposed to?

6.1.3 Error sources with the model setup

There were error sources associated with the model setup in the model tests. The middle of the model was not directly in the middle between the two pulleys in x-direction, as seen in Figure 4.3. This probably made the rotational stiffness of the cylinders different. Installing the model closer to the pulleys would cause less rotation motion of the cylinders, given stiff moment absorbers at the top of the cylinder. This is due to the vertical component of force through the tensioned rope decreases with the length for a given vertical displacement.

Similarly, Other aspects about the model test setup worth discussing is the vertical beams that the pulleys were connected to. The heights at which the pulleys were positioned above the still water surface were not the same, as this was not accurately measured when installing the model in the basin tank. At a later time, it was measured that the pulley at the front of the model was 0.12 m above the still water level, and the aft pulley was 0.14 m

above the still water surface. The pulleys should have had the same heights above the still water level to create symmetry in the vertical force components through the tension line.

The spring stiffnesses were not constant throughout the model testing. They were known to be roughly 170 N/m at the beginning of model testing. However, the springs experienced creeping, as shown in Figure 6.2. The spring at the end where tension was changed was elongated the most. It can be theorized that this was due to increased tension being applied faster than the model could follow perfectly, considering inertia and hydrodynamic damping in x-direction, resulting in small elongations each time the tension was increased.

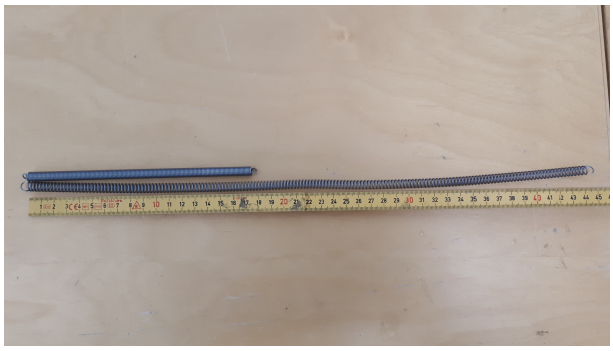

Figure 6.2: Creeping in the spring where tension was applied. There was not as much creeping in the spring at the other end.

Another error source with the model setup is associated with the tensioned rope increasing the tension in the solar deck also being the mooring line. The ability of the model to follow the waves is hence affected by the tension, because of the externally applied tension going through the pulleys, which have a fixed vertical position. The vertical component of the externally applied tension increases with the vertical displacement of the model. This means that for large wave heights, the model experiences an increased vertical force component, pulling it towards the height of the pulleys. Hindering the model from following the waves is an unwanted effect in model testing. An additional unwanted effect from the vertical beam and pulley setup would be the beams and pulleys touching waves with large enough amplitudes, which would be 0.12-0.14 m. However, these wave heights were never tested, so this was not observed as a problem during the model testing.

It is also worth noting the difference in the tested wave heights compared to the down-scaled assumed wave heights the installation is expected to be exposed to. It is assumed that the structure will be exposed to significant wave heights H_s = 4m, which is 0.4 m for the corresponding 1:10 scale. This is likely far larger than what is possible to achieve in the model tank. These waves would probably cause severe bending in the critical point of the model in the split-line rods at the top of the cylinder ends, and in the split-line rods themselves. The model did break once, as treated in Tillegg B. As a result, concern was associated with testing extreme wave conditions, as the model repeatedly snapping would cause delays in the work schedule. The waves testes for the 3D surface mapping purposes in for example Figure 5.6 had a height H = 0.01 m. This corresponds to about 0.1 m in full scale, which is not large waves. However, significant swinging motion in the solar deck was achieved for the regular waves with period T = 0.566 s, seen in for example

Figure 5.10, which was tested for wave heights H = 0.015 m, corresponding to 0.15 m in full scale. The fact that resonance can be achieved by waves this small has significance for a full scale installation, as rough weather conditions are not the only conditions of concern for seakeeping purposes.

6.2 Discussion on theory, results and methods

6.2.1 Solar deck modelling

Parabola approximation

As seen to the right in Figure 5.1, the theoretical sag predicted by the parabola simplification from Equation 2.3, and the observed sag for given lengths L and tension levels T seem to fit well for large tension levels and small sags. However, the theoretical tension at the largest sag possible, calculated in Equation 4.2, was larger than the actual tension in the deck at the largest sag level. The parabola equations are therefore acceptable approximations to the static solar deck shape for the tension levels tested in this thesis.

String approximation

The applicability of the continuous string equation in Equation 2.5 on the relatively heavy solar deck in this thesis is a topic for discussion. Firstly, the string equations assume a linearly distributed mass along the string, but this is not the case for the solar deck in this thesis. The mass is mainly grouped along the plates, with small amounts of mass in between the solar panels, being the net. Secondly, the string equations assume that there is no sag in the string, which is not the case for the solar deck.

The resulting natural frequency calculated by the string vibration approach in Figure 5.2 was quite large, with a correspondingly low period. However, from Figure 5.2, first mode string vibration gives natural period of 0.55 s at 10 N, and 0.47 s at 15 N, which seems to be the case for the standard deviation of marker 7 vertical motion in Figure 5.6 as well. The standard deviation in Figure 5.6 for T = 0.6 is larger for 10 N and 15 N than the higher tension levels. This indicates that there was some first mode string vibration for these period and tension combinations. However, the peak at T = 0.6 s could also be due to the middle of the solar deck experiencing less motion at T = 0.8 s. This is due to the waves at this period are twice as long as the distance between the cylinders, meaning that two cylinders just rotate around the middle of solar deck, causing the vertical motion of marker 7 i z-direction to be smaller than usual. This effect might begin at T = 0.6 s, which is why this is a peak for all tension levels.

Figure 5.14 also shows that there is symmetry as predicted in the vibration or swinging mode, as the standard deviations are roughly the same on both sides of the middle of the solar deck. This supports the initial theory that the main motion mode for the solar deck is first mode string vibration.

Discrete mass-spring model

The discrete mass-spring model was modelled as six springs with five discrete masses in between the springs. This system was assumed to be symmetric in its static and dynamic behaviour, meaning that it could be reduced to a one-dimensional problem with three dofs. The values used for calculating the natural frequency of the solar deck came from the model itself, from Table 3.

Modelling the member in between the masses as springs implies that there is some elasticity in the solar deck. Although the actual solar deck net in the model seems quite in-elastic when pulled by hand, it was believed that the distributed mass resting on the deck would be large enough that the deck would be slightly elongated, resulting in the solar deck net functioning as a spring for large tension levels. The plot arrived at in Figure 5.2 shows that the discrete mass model results in natural frequencies in the same order as the string equation predicted.

However, as noted in Figure 5.2, the natural frequency of the discrete mass and spring approximated solar deck decreases for increasing tension levels, which is somewhat unphysical. The string equation predicts higher natural frequency for higher tension levels, which is in agreement with the equation for the natural frequency of any mass-spring system. From Equation 2.42, the natural frequency is given as $\omega_0 = \sqrt{\frac{k}{m}}$, and increasing the tension is equivalent to increasing the stiffness and rigidity, k.

In the discrete mass model, this phenomenon comes from the calculation and assumption in Equation 2.9, where a larger angle for each spring with the horizontal line leads to a larger equivalent vertical stiffness, directly derived from a force decomposition consideration. These results lead to the possibility that this is the wrong method to calculate the equivalent vertical stiffness for the simplified system with three degrees of freedom in Figure 2.3. For the purpose of the control system, a more representative mathematical model would therefore be needed. This could have been achieved by modelling members of constant length with masses in between them, with springs on each end point. This would be a more representative mathematical model of the actual tested system.

Also, for the purpose of calculating the eigenfrequency directly as a function of the tension, the discrete mass model would need to include horizontal dofs for all the discrete masses in the model. Because of the masses in the present discrete model being restrained in horizontal direction, it is impossible to apply horizontal forces at the two end points that will have an effect on the tension and sag of the solar deck modelled by this approach. To achieve this, the discrete masses and the end points would have to be modelled as free to move in 2 dofs each, complicating the modelling and system. This was beyond reach for the author, and was therefore not pursued further. Still, satisfactory estimates of the natural frequency of the solar deck were achieved by both the string equation and the discrete mass approach.

6.2.2 Dynamics of the model tested

As mentioned in the previous subsection, large standard deviations at the 10-15 N levels for T = 0.6 s in Figure 5.6 could be explained by string vibrations. However, these

large standard deviations can also be explained by quasi-dynamic and dynamic horizontal behaviour in the solar deck induced by the springs on each side of the model. The vertical motion in the middle of the solar deck is also a function of the horizontal motion of the top of each cylinder, where the solar deck is fixed. As seen in the surface plot for the standard deviations of horizontal (x) motion for marker 4 and 10 in Figure 5.9, there are increased standard deviations for tension levels 10-15 N for most wave periods, but especially around T = 1.4 s. This indicates that tension levels of 10-15 N allow the cylinders to have larger motion amplitudes in x-direction, further supporting the theory that the horizontal cylinder motion effects contribute to the vertical motion at the middle of the solar deck. However, there is likely some codependency in the vertical motion in the middle of the solar deck and the horizontal (x) motion of the cylinders. It is likely that they have an influence on each other, meaning it can not be explicitly concluded what the main contribution is based on the data obtained in this thesis.

Quasi-dynamic and dynamic horizontal motion of the top of the cylinder is made up of two contributions; translational motion along the x-axis, and rotation of the cylinder. If the top of the cylinder has some vertical distance from the point of rotation, a rotational contribution is found. These contributions are illustrated in Figure 6.3. The welding rods and added stiffness around the top of the cylinder was meant to prevent the rotational contribution from being large.

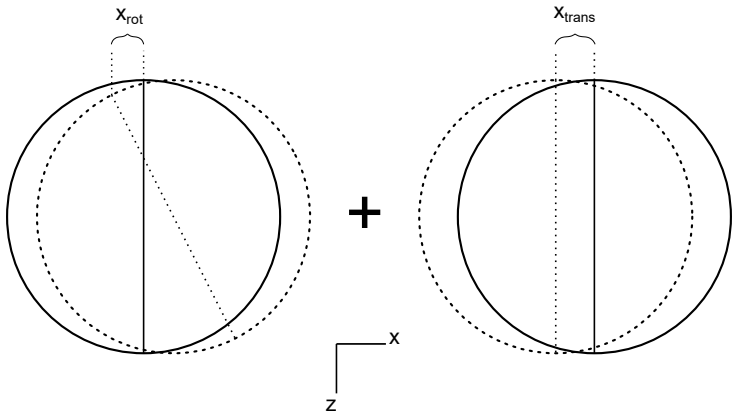

Figure 6.3: Translation and rotation of the cylinders contributing to horizontal motion of the top of the cylinder.

When extracting the standard deviation data from the model tests, the motion of each marker in z direction could have been extracted as a deviation from its equilibrium position for the given tension level. This would have indicated if the vertical motion amplitudes were similar on both sides of the equilibrium position, as it is assumed that a horizontal string vibrates so that the amplitude is equally large in vertical direction. This is stated by the constant amplitude ϕ_0 in Equation 2.4. This could have further indicated to what degree vertical string vibration or horizontal spring quasi-dynamics and dynamics are contributing to the total vertical motion in the solar deck.

In order to properly model the natural frequency and vertical motion in the solar deck, the stiffness in horizontal motion of the cylinders would have had to be considered. However, there were other factors contributing to the natural frequency of the actual model setup

that was tested. In the following, these factors are listed including the translational and rotational stiffnesses of the cylinders mentioned above.

- The translational stiffness of the cylinders from the springs near the force measurement rings, seen in Figure 4.6. These were given as 170 N/m, and likely contributed to some horizontal motion of the cylinders.
- The rotational or bending stiffness of the moment absorbers near the top of the cylinders. This was very low before one of the rods snapped, but acceptably large after modifying this part, as treated in Tillegg B.
- The torsional and bending stiffness of the beams placed over the wave tank in the transverse direction of the waves, as shown in Figure 4.3. The tensioned lines going vertically down from the transverse beams introduced a moment arm, and considering that the transverse beams were not completely rigid, some small bending and torsion contributions were visually observed.

These contributions were additional stiffnesses contributing to the full mass-spring-damper system that makes up the actual small scale model test system. Summarized, the total theoretical dynamic system describing the model setup is quite complex. Modelling the entire tested system for predicting the natural frequency and behaviour would have been challenging. In addition, hydrodynamic considerations like resonant wave excitation in surge and heave would also have had to be considered.

Relatively simple estimates were instead employed for the modelling the dynamics of the system, only considering the stiffness in the solar deck. So what are the implications of this for the control system? It means that a higher fidelity model of the 2D system would have had to be implemented in order to correctly assess the natural frequency as input to the controller. For a semi-active controller to be feasible in a full scale installation, the coupled torus and solar deck behaviour would have to thoroughly modelled.

6.2.3 FFT as wave frequency estimator

FFT for regular waves

In Section 5.5.1, FFT was performed on marker 4 and 7 vertical motion for three regular wave periods; 0.5 s, 1.0 s, and 1.5 s. These periods are tested with the tensions 25 N and 45 N, varying with 10 Hz and 50 Hz sampling rate for the FFT algorithm. The duration tested was 5 seconds, which in hindsight is realized is quite low. This duration is also not the duration of an envisioned data window in full scale, of about 20-30 minutes. 5 seconds data windows were simply used in order to save time when conducting the tests. However, the plots show that good estimates of the regular wave frequency can be obtained from relatively small motion data windows.

It can be seen from the plots that the 50 Hz FFT sampling frequency tend to overestimate the wave frequency, while the 10 Hz FFT sampling frequency estimates the frequency more accurately. Also, FFT applied to the middle deck marker 7 leads to higher peak frequency in the estimated spectrum. This can be explained by the vertical motion of marker 7 being

affected by the surge motion of both of the cylinders and the wave frequency. Smoothing the curves and extracting the peak of the smoothed spectra could have given more accurate frequency estimates.

Increasing the tension does not seem to affect the peak frequency of the estimated spectrum by a lot. It is only observed for marker 7 for wave period T = 0.5 s and wave height H = 0.02 m. The resulting FFT peak frequencies are also seen to match more closely with the actual regular wave frequency when the frequency decreases, meaning for increasing periods. This is reasonable, as the lowest period tested is 0.5 s, and at this period, the model does not necessarily follow the waves because of their frequency being too high.

FFT for irregular waves

In Section 5.5.2, the FFT algorithm was performed on the motion of the model in three Jonswap wave spectra with peak frequency $T_p = 0.5$ s, 1.0 s, and 1.5 s, and a significant wave height $H_s = 0.01m$. FFT was performed with a sampling rate of 20 Hz for a duration of 30 s, and the tension levels tested were 20 N and 35 N.

At $T_p = 0.5$ s, the peak frequency is satisfactory estimated by the FFT algorithm as 2.03 Hz by marker 4 for both 20 N and 35 N tension levels. At $T_p = 1.0$ s, the peak frequency estimated at marker 4 by the FFT algorithm is 1.2 Hz for 20 N tension level, and 1.67 Hz for 35 N tension level. For $T_p = 1.5$ s, the peak frequency estimated at marker 4 by the FFT algorithm is 0.77 Hz for 20 N tension level, and 0.9 Hz for 35 N tension level. This suggests that higher tension levels in the model test setup seem to affect the motion, so that the FFT algorithm yields different peak frequencies for the given irregular sea state. Other than this, for a 20 N tension level, the FFT gives an acceptable estimate of the peak frequency in the spectrum.

6.3 Discussion on the findings in this thesis with regard to a full scale installation

6.3.1 FFT based control algorithm

The applicability of performing FFT and control based on a single natural frequency for the solar deck in sea states consisting of many superimposed sea states is a topic for discussion. As seen in the plots in Section 5.5.2, the FFT algorithm can to some degree estimate the frequency of an irregular sea state, given that the structure is not too restricted from following the wave motion. In Section 5.5.2, a sampling frequency of 20 Hz was chosen, which seemed to function well for estimation the frequency. However, as seen in Section 5.5.1, the accuracy of the FFT estimated frequency can be affected by the sampling frequency, meaning that an optimal sampling frequency might depend on the peak frequency of the sea state, which is not known before it is measured.

Also, the FFT algorithm was performed directly on position data during the model tests in this thesis. However, obtaining equally accurate position measurements in a full scale installation is most likely not possible. For a full scale offshore installation, the FFT algorithm could be performed directly on acceleration measurements, by the use of an accelerometer. As discussed over e-mail (T. Kristiansen, personal communication, June 2022), FFT on measurements of acceleration in heave will lead to increased sensitivity to changes in the measured frequency, because of the wave frequency ω being squared in the equation for acceleration in vertical direction from potential theory in Equation 2.25.

Figure 5.19 shows the smoothed plot of FFT performed on acceleration in irregular waves. It shows that the frequency spectrum becomes not very representative of the actual sea state, which will be problematic for the control system in a full scale installation. Performing the FFT algorithm on acceleration was not done in real time in the model tests in this thesis due to the acceleration not being available as sampled data in real time, only after data recording had ended.

6.3.2 Tension levels in the solar deck

The maximum tension level tested on the model in this thesis was 63 N. This is the extreme level, and is not likely will be able to implement for a multi-torus structure. From Table 1, a relatively large tension level that could be used in the case that resonant vibrations is likely, is for example 40 N in the model scale. In full scale, this corresponds to $10.67^3 \cdot \frac{1025}{1000} \cdot 40N = 49.8$ kN, or 5.08 tons of force, which is unfeasible for lightweight winches envisioned to be used for the purpose of controlling the motion.

Implementing a control system for the multi-torus structure entails many technical challenges with regard to how control action is actuated. As discussed in Section 3, the actuators need to be placed so that they can efficiently change the natural frequency of the solar deck. However, changing the natural frequency of the solar deck is only possible to some extent, given that the solar deck can be moved and stretched, meaning it is to a lesser degree fixed to the toruses. The membrane solar deck must perhaps be able to slide over the toruses if control shall be possible to introduce.

This ties into the question of whether or not it is feasible, possible, and necessary to introduce control for the structure. It could be that active or even semi-active control is overkill for the problems related to the flexible nature of the structure. Passive control measures, like designing solar decks that are flexible enough to allow the structure to follow the waves, but stiff enough to avoid resonant vibrations, could be sufficient. However, this is speculation, so the topic needs more research in order to converge towards efficient solutions.

6.3.3 Maintaining electrical efficiency

Maintaining electrical efficiency is important for FPV installations. However, for offshore applications, the surrounding conditions will be rough. This can lead to waves overtopping over the structure and slamming from underneath the solar deck, as shown in Figure 6.4.

(a) Overtopping waves

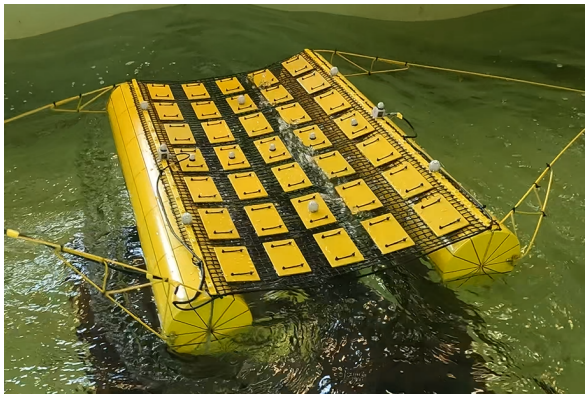

(b) Slamming

Figure 6.4: Overtopping waves and slamming from underneath for a Jonswap spectrum with $H_s = 0.05$ m, $T_p = 1$ s, and peakedness $\gamma = 3$. The tension level was 45 N.

Overtopping and slamming can lead to water collecting on top of the solar deck. This was carried in mind while finding an appropriate design for the solar deck in this thesis. The result was the black net, which drained water well. However, water splashing onto the top of the solar deck and solar panels was noted in the model tests, as seen in Figure 6.5. For a full scale installation, this could lead to accumulation of sediments, crystallized salt, seaweeds and other debris on top of the solar panels, reducing their efficiency. Active or passive routines for removing this would be needed so that optimal electrical efficiency could be maintained.

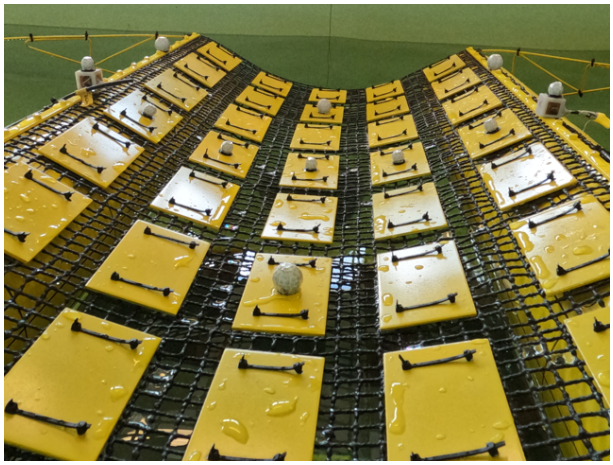

Figure 6.5: Despite the deck being well draining, some water still splashed up and onto the solar panels. In full scale with salt water, this can lead to decreased electrical efficiency.

7 Conclusion and further work

The vibrations and swinging motions of a freely hanging 2D solar panel deck spanned in between two cylindrical floaters have been investigated in this thesis. The 2D simplified solar deck is a part of a 3D multi-torus structure, consisting of several concentric toruses with a membrane deck resting on top of the toruses. The 2D simplified model investigated is obtained by considering a cross section of the two outermost toruses and the solar deck freely hanging in between them. A goal has been to introduce the concept of semi-active control to this simplified 2D system. The method of which control has been introduced is through regulating the tension on the freely hanging solar deck.

Actively regulating states requires a lot of energy, often in the form of electricity. For FPVs it is of interest to use as little of the electrical energy produced as possible. This is important in order to not spend more electrical energy than is produced by the solar panels. Therefore, a semi-active control system based on controlling the natural frequency of the solar deck has been proposed. The proposed control system for a full scale installation involves performing a FFT algorithm on recorded and stored data windows. These data windows are proposed to be of 20-30 minutes duration as the sea state changes slowly, and contains heave measurements from the multi-torus structure. A peak frequency can be obtained from the FFT algorithm, which is then compared to a natural frequency of the solar deck calculated as a function of the present tension in the solar deck. The control logic then commands a new tension level if resonant vibrations are found to be likely.

The vibration mode of the solar deck was assumed to be similar to first mode string vibration in between the floater elements, so a string vibration based natural frequency calculation module was proposed. An additional discrete mass and spring model representing a freely hanging member was presented as an alternative higher fidelity natural frequency calculation module. The discrete mass and spring model yields a lower natural frequency when the tension and thus the stiffness is higher, contradicting the underlying laws of a mass-spring system, where the natural frequency increases with increased stiffness and rigidity. The discrete mass and spring model is therefore not representative of the solar deck behaviour, and needs improvement.

A small scale model was built in 1:10.67 scale of what is believed to be a fitting size for the multi-torus structure. The model was built based on the 2D simplification of the multi-torus structure. The solar deck in the small scale model consisted of a square flexible net with metal plates representing the load from the solar panels. This net was fastened at two opposing ends to the top of two circular cylindrical floaters representing the torus cross section, leaving the two other ends of the net free to move. The model was tested in regular waves for the purpose of mapping the response of the solar deck and investigate the effect of changing the tension in the solar deck. The tested regular wave periods were 0.4 s to 1.5 s, with increments of 0.1 s. The tensions tested were 10 N to 50 N with 5 N increments. The results showed that the vertical motion of the solar deck was largest for 10-15 N and was almost always reduced when increasing the tension up 40-50 N. Despite the tension being increased through the mooring line of the model, the ability of the model to follow the waves was not noticeably decreased.

An additional tested special case was testing regular waves that had a wavelength of 0.5 m, equal to the distance between the floaters. This was believed to be the waves that would cause the most vibrations in the solar deck, with a period of T = 0.566 s. Here, the results showed that to the vertical motion in the middle of the solar deck was amplified in comparison to the vertical motion of the cylinder floaters with increased tension levels. Furthermore, 20-25 N seemed to be a critical tension level, representing the peak of the motion amplitude in the middle of the solar deck. However, it was concluded that this peak in vertical motion was not necessarily only caused by resonant vibrations in the solar deck itself, but also by resonant vibrations in the springs of the model setup.

Real-time FFT tests were also conducted on the vertical response of the model. These were done by receiving a real-time stream of data from the motion tracking system Qualisys, storing the position data, and computing the FFT algorithm for the data batches, acquiring an estimate of the frequency spectrum for the incident waves. The peak frequency could then be extracted from these spectra. There was originally supposed to be a winching actuator present in the model tests that could actuate based on the real-time FFT-estimated frequency, but the allocated actuator proved to not be powerful enough to statically hold the sought tension levels for the model tests.

To conclude, the multi-torus structure as a flexible floating island meant to support solar panels is a promising concept. This can be concluded by the results of previous studies of the hydrodynamic behaviour of the structure. However, judging by the findings in this thesis, the flexible membrane deck is prone to swinging motions, as theorized from the beginning. However, isolating the solar deck motion to only heave in the 2D model tests proved challenging, meaning that the swinging motion observed in this thesis could have been amplified by the model setup itself. This problem may therefore not be that big of an issue for a 3D structure. A solution to the problem was nevertheless proposed as a semi-active controller, although it is possible that passive solutions will suffice. More research is therefore needed on the multi-torus structure behaviour.

7.1 Further work

The multi-torus structure as a floating island for supporting PV technologies is a relatively new concept. Previously, two experimental hydrodynamics focused master theses and two numerical hydrodynamics focused master theses have been written on the subject. This thesis studies the behaviour and introduces control of the solar deck meant to carry the solar panels, and this was done for a 2D simplification of the multi-torus structure.

A natural next step is to study the behaviour of and introduce control for a structure consisting of 3D toruses. This could involve studying the innermost torus with a solar deck on top of it. A weighted membrane could then be adhered to the top of either a single torus or several. Membrane vibrations could then be considered in the middle of the torus, and alternatively in between toruses for the case with several toruses present. For further work on control for the structure, expanding on the control scheme in this thesis to include the wave height as input could be beneficial as the controller in this thesis is only based on the frequency of the sea state.

This is given that the solar deck is suspended in mid-air. This might not be an optimal solution, so further studies could also focus on optimizing the structure design. This could involve studying the optimal number of toruses and the distance between them, optimal cross section diameters, and the corresponding optimal solar deck span length, mass distribution, and configuration. This could be done through hydrodynamic analyses of the torus interaction with each other, which can lead to better understanding of the optimal draft for the structure.

Design and research also needs to be put into the process of installing a full scale structure. The marine operation of cost-efficiently installing the islands, and placing the solar deck on top of the multi-torus structure are both important aspects for making the solution economically sustainable. Other aspects of a full scale installation that need research are the accumulation of sediments, salt, seaweeds and other debris on top of the solar panels, reducing their efficiency. Routines, either active or passive, for removal of these are needed so that optimal electrical efficiency can be maintained.

References

Bachynski, Erin E. et al. (2019). Course TMR4182 Marine Dynamics Compendium, Department of Marine Technology, NTNU.

Balchen, Jens G., Trond Andresen and Bjarne A. Foss (2016). *Reguleringsteknikk 6. utgave*. NTNU Grafisk senter.

Bell, Kolbein (2014). *Konstruksjonsmekanikk, del 1: Likevektslære*. Fagbokforlaget.

Borvik, Petter Plünneke (2017). *Experimental and Numerical Investigation of Floating Solar Islands*. Master's thesis, Department of Marine Technology.

Brodtkorb, Astrid H., Ulrik D. Nielsen and Asgeir J. Sørensen (2015). 'Sea State Estimation Using Model-scale DP Measurements'. In: *Proceedings of OCEANS '15*.

– (2018). 'Online wave estimation using vessel motion measurements. This work was supported by the Research Council of Norway through the Centres of Excellence funding scheme, project number 223254 - NTNU AMOS'. In: *IFAC PapersOnLine* 51(29), pp. 244–249.

Brown, David T. and Subrata K. Chakrabarti (2005). 'Chapter 8 - Mooring systems'. In: *Handbook of Offshore Engineering* Volume 1, pp. 663–708.

Buljan, Adrijana (2022). *Offshore Wind Investments to Reach USD 810 Billion by 2030 – Rystad Energy*. URL: https://www.offshorewind.biz/2021/04/30/offshore-wind-investments-to-reach-usd-810-billion-by-2030-rystad-energy/ (visited on 23rd May 2022).

EMCE-Winches (2022). *Winch selection*. URL: https://emce.com/about-winches/winch%5C%20selection (visited on 27th Mar. 2022).

Equinor, ASA (2021). *Vil teste ut flytende sol utenfor Frøya*. URL: https://www.equinor.com/no/news/20210114-test-offshore-solar.html (visited on 15th Dec. 2021).

Faltinsen, Odd M. (2011). 'Hydrodynamic aspects of a floating fish farm with circular collar'. In: *International Workshop on Water Waves and Floating Bodies* 26.

Faltinsen, Odd Magnus (1990). *Sea loads on ships and offshore structures*. Cambridge University Press.

Fossen, Thor Inge (2021). *Handbook of Marine Craft Hydrodynamics and Motion Control, second edition*. Wiley and Sons Ltd.

Garanovic, Amir (2022). *Albania's 500kWp floating solar plant restarts commercial operation*. URL: https://www.offshore-energy.biz/albanias-500kwp-floating-solar-plant-restarts-commercial-operation/ (visited on 23rd Apr. 2022).

Hovland, Kjetil Malkenes (2021). *Ocean Suns flytende solkraftverk alvorlig skadet*. URL: https://e24.no/boers-og-finans/i/6zx6eO/ocean-suns-flytende-solkraftverk-alvorlig-skadet (visited on 20th Aug. 2021).

Kristiansen, Trygve et al. (2021). 'A flexible multi-torus solar island concept'. In: *The 36th International Workshop on Water Waves and Floating Bodies, Seoul, South Korea*.

Li, Peng (2017). *A Theoretical and Experimental Study of Wave-induced Hydroelastic Response of a Circular Floating Collar*. PhD thesis, Department of Marine Technology.

MacGregor (2022). *Chain stopper*. URL: https://www.macgregor.com/Products/products/deck-machinery/chain-stoppers/ (visited on 5th Apr. 2022).

MacLeod, Cameron (2022). *Fourier Transforms With scipy.fft: Python Signal Processing*. URL: https://realpython.com/python-scipy-fft/ (visited on 25th Apr. 2022).

Moore, W. Robert (2022). *Distribution of Fossil Fuels*. URL: https://www.nationalgeographic.org/encyclopedia/distribution-fossil-fuels/ (visited on 23rd May 2022).

Ocean Sun, AS (2021). *About Ocean Sun*. URL: https://oceansun.no/about/ (visited on 2nd Sept. 2021).

Oceans-Of-Energy (2022). *North Sea 1*. URL: https://oceansofenergy.blue/north-sea-1/ (visited on 5th May 2022).

OceanSun (2022). *Annual report 2021*. URL: https://oceansun.no/wp-content/uploads/2022/04/2021-Ocean-Sun-annual-report.pdf (visited on 27th May 2022).

Offshore-Technology (2022). *Which Winch – Hydraulic or Electric?* URL: https://www.offshore-technology.com/contractors/lifting/winches-inc/pressreleases/presswhich-winch-hydraulic-electric/ (visited on 22nd Mar. 2022).

Olsen, Øyvind (2020). *A Numerical Study of a Multi-torus Floating Solar Island Concept, with the use of Computer Programming*. Master's thesis, Department of Marine Technology.

Onsrud, Magnus (2019). *An Experimental Study on the Wave Induced Vertical Response of an Articulated Multi-Module Floating Solar Island*. Master's thesis, Department of Marine Technology.

Orcina (2022). *Rope/wire: Axial and bending stiffness*. URL: https://www.orcina.com/webhelp/OrcaFlex/Content/html/Ropewire,Axialandbendingstiffness.htm (visited on 24th June 2022).

Our World In Data, Org (2022). *Electricity Mix*. URL: https://ourworldindata.org/electricity-mix (visited on 20th Feb. 2022).

Patterson, Bruce D. et al. (2019). 'Renewable CO2 recycling and synthetic fuel production in a marine environment'. In: *Proceedings of the National Academy of Sciences - PNAS,* 116 (25), pp. 12212–12219.

Pettersen, Bjørnar (2018). *Marin teknikk 3, hydrodynamikk*. Akademika.

Ren, Zhengru et al. (2021). 'Sea state estimation based on vessel motion responses: Improved smoothness and robustness using B´ezier surface and L1 optimization'. In: *Marine structures* 76, p. 1.

ScienceDirect (2022). *Levelized Cost of Electricity*. URL: https://www.sciencedirect.com/topics/engineering/levelized-cost-of-electricity (visited on 6th June 2022).

Septimiu, Luca, Florentina Chira and Victor-Octavian Roşca (Jan. 2005). 'Passive, Active and Semi-Active Control Systems in Civil Engineering'. In: *Bulletin of the Polytechnic Institute of Jassy, CONSTRUCTIONS. ARCHITECTURE Section, Tomme LI (LV), Fascicle 3-4, pages 23-32 (2005)* 3.

Sigstad, Mari Vassdokken (2019). *A Numerical and Experimental Study of a Multi-torus Floating Solar Island Concept*. Master's thesis, Department of Marine Technology.

Steen, Sverre (2014). *Experimental Methods in Marine Hydrodynamics*. Department of Marine Technology. URL: https://home.hvl.no/ansatte/gste/ftp/MarinLab_files/Litteratur/NTNU_Eksprimentelle_metoder_kompendium.pdf.

Swimsol (2022). *Recent Swimsol solar energy projects*. URL: https://swimsol.com/solar-projects-offshore-solarsea-and-rooftop/ (visited on 6th May 2022).

Technical-University-Wien (2022). *Heliofloat – A floating lightweight platform*. URL: https://www.tuwien.at/fileadmin/Assets/dienstleister/forschungsmarketing/messe/Messe_Rueckblick/HM2016/HELIOFLOAT_platform_EN.pdf (visited on 6th May 2022).

Thern-Winches-and-Cranes (2022). *What is an air winch? Benefits and applications*. URL: https://thern.com/blog/what-is-an-air-winch/ (visited on 22nd Mar. 2022).

Tolaas, Svanhild (2020). *A Numerical and Theoretical Study of a Multi-torus Floating Solar Island Concept*. Master's thesis, Department of Marine Technology.

Tom Smedley, BBC (2021). *Is the world running out of fresh water?* URL: https://www.bbc.com/future/article/20170412-is-the-world-running-out-of-fresh-water (visited on 15th Dec. 2021).

Trapani, K. and D. L. Millar (2014). 'The thin film flexible floating PV (T3F-PV) array: The concept and development of the prototype'. In: *Renewable energy* 71, pp. 43–50.

Trapani, K. and M. R. Santafé (2015). 'A review of floating photovoltaic installations: 2007–2013'. In: *Progress in photovoltaics: Research and applications* 23, pp. 524–532.

US Energy Information Administration, Org. (2022). *EIA projects nearly 50 percent increase in world energy use by 2050, led by growth in renewables.* URL: https://www.eia.gov/todayinenergy/detail.php?id=49876# (visited on 20th Feb. 2022).

US Office Of Energy Efficiency, Org. (2022). *Solar Photovoltaic Cell Basics.* URL: https://www.energy.gov/eere/solar/solar-photovoltaic-cell-basics (visited on 20th May 2022).

Vo, Thi Thu Em et al. (2021). 'Overview of Possibilities of Solar Floating Photovoltaic Systems in the OffShore Industry'. In: *Energies* 14(21), p. 6988.

Weisstein, Eric W. (2021). *Catenary, from MathWorld - A Wolfram Web Resource.* URL: https://mathworld.wolfram.com/Catenary.html (visited on 16th Dec. 2021).

– (2022a). *Discrete Fourier Transform. From MathWorld - A Wolfram Web Resource.* URL: https://mathworld.wolfram.com/DiscreteFourierTransform.html (visited on 16th Apr. 2022).

– (2022b). *Fast Fourier Transform. From MathWorld - A Wolfram Web Resource.* URL: https://mathworld.wolfram.com/FastFourierTransform.html (visited on 16th Apr. 2022).

– (2022c). *Fourier Matrix. From MathWorld - A Wolfram Web Resource.* URL: https://mathworld.wolfram.com/FourierMatrix.html (visited on 16th Apr. 2022).

Winsvold, Jonathan (2018). *An Experimental Study on the Wave-Induced Hydroelastic Response of a Floating Solar Island.* Master's thesis, Department of Marine Technology.

Wong, Y. Wesley and Sergio Pellegrino (2006). 'Wrinkled membranes part I: Experiments'. In: *Journal of Mechanics of Materials and Structures* 1.

Yin, Luqi et al. (2021). 'Semitransparent polymer solar cells floating on water: selected transmission windows and active control of algal growth'. In: *Journal of Materials Chemistry C* 9, pp. 13132–13143.

Appendix

A Making the model

The model was made to be as light as possible, because of the need for an air-gap under the solar deck, with some margin. This was also because of the draft of the multi-torus floating island being assumed to be small compared to the cross sectional diameter of the toruses. This meant that the draft was something to be calculated, based on the known shape of the floaters and the load they were supposed to carry. This is somewhat different than the usual approach with model testing, where a sought water-line and stability condition results in the geometry and mass distribution of the model. In other words, it was not crucial to have a given draft, because what the draft would be for a full scale installation is not.

The buoyancy force on the cylinder is given by Equation A.1, where ∇ is the volume displaced by the object, ρ_w is the water density, and g is the gravitational constant.

$$F_B = \nabla \cdot \rho_w \cdot g \tag{A.1}$$

So for the making of this model, this equation was solved for the draft as part of the volume displacement, ∇ by trial and error. ∇ is the volume of the structure underwater, so for a circular cylinder this is given by the submerged area multiplied by the length of the cylinder. For a draft of one third of the diameter for a circle with radius 0.075 m, the underwater area becomes 0.00516 m^2, as shown in Figure A.1.

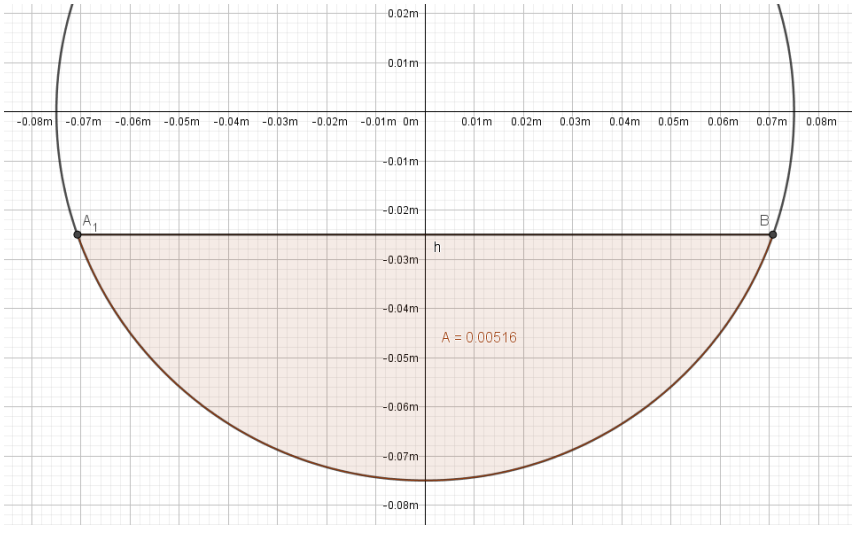

Figure A.1: Area of a circle of radius 0.075m below a horizontal line at 0.05 m height above the bottom of the circle. The shaded (underwater) area is 0.00516 m^2

The corresponding mass displacement Δ then becomes $0.00516m^2 \cdot 1.8m \cdot 1000kg/m^3 = 9.288kg$, which fits quite well for the measured total mass of the model of 8.72 kg. The waterline was painted at this draft of 0.05m, which seemed to fit well when placing the model on water.

A full scale solar panel mass of 40 kg/m^2 was chosen instead of 50 kg/m^2 in order to give some margin for equipment in both model scale and in full scale, but also in order to give a smaller draft, which at the time was sought. A good alternative could have been dimensioning for the draft of half the diameter. This would have made the hydrodynamics more linear in behaviour. However, it was believed at the time of making the model that allowing some sag in the deck would be beneficial in order to test many different tension levels, some of them quite low, which would result in a large solar deck sag.

The model was made with a plexiglass cylinder with an outer diameter of 0.15 m, and a wall thickness of 0.005 m (5 mm). The cylinder was taken from a Sintef material storage, and had an original length of 1.8 m, and was therefore cut into two halves. Two circular disks of about a centimetre width, and radius about the same as the cylinders, were glued to the ends of each cylinder to seal the ends off. The disks had a slit cut into them, so that the split-line welding rod could be placed inside it and glued in place. A beam with holes in it was glued on top of each cylinder, so that a second beam with holes could be fastened to the glued beam using screws. Between the two beams, the solar deck net would be placed, effectively fixing it to the top of the cylinders.

Figure A.2: Picture from the cylinder production. Painted yellow with black lines. A water line was also included at a later point in time. The small beam with screws along the cylinders can here be seen. The purpose of these was to fix the solar deck net to the cylinders.

As mentioned, the membrane deck was chosen with water drainage in mind. Therefore, a net was chosen as an approximation to the actual layout of the deck in full scale. This also made attaching the solar panels to the deck easier, as seen in Figure A.3. The net was bought at 'Stoff og Stil' at Tiller, south of Trondheim. The aluminium plates were cut out from an aluminium sheet which was also found in a Sintef material storage.

The net bought was described by the manufacturers as 30% polyester and 70% PVC. From the author's knowledge, it is believed that the strings in the net consists of a polyester thread inside a soft PVC foam-like coating. The net is originally designed to be used as a means of preventing carpets from slipping (anti-slip). Despite this everyday-use, the net is quite strong, as shown in Figure A.4.

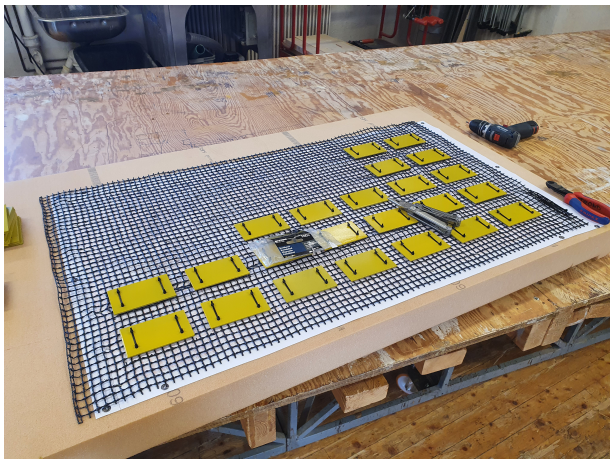

Figure A.3: Using strips to attach the solar panels to the net. For this, there had to be drilled holes in the panels so that the plates could reliably be attached to the net.

Figure A.4: Testing the ultimate strength of the net in the same direction that tension will be applied during model testing. Here the force measurement shows approximately 34 N.

The strength test proved that the ultimate strength for one bearing string was 50-60N. For two bearing strings, as shown in Figure A.4, the ultimate strength was roughly 100-110 N. This implies that one string can carry roughly 50 N. Over the breadth of the model, the amount of strings carrying in-line tension was counted to be 80. This means that the net should be able to handle at least $50\text{N} \cdot 80 = 4000$ N. This is well above the tension levels in the model tests.

The stretch tests were done for soaked and not soaked samples, and the differences between observed ultimate strengths were negligible. However, the mass of the soaked test sample was roughly 1.5 times as large as a dry sample of the same size. The effect of evaporation in air after having been soaked was not tested. Also, the effect of repeated soaking and drying has not been tested, but in hindsight could have been an interesting study. The objective of the soaking test done here was to see if water had any noticeable effects over a couple of days. So the study could have been conducted for a longer time, but at the time it was conducted, it was decided that testing over a weekend would be enough.

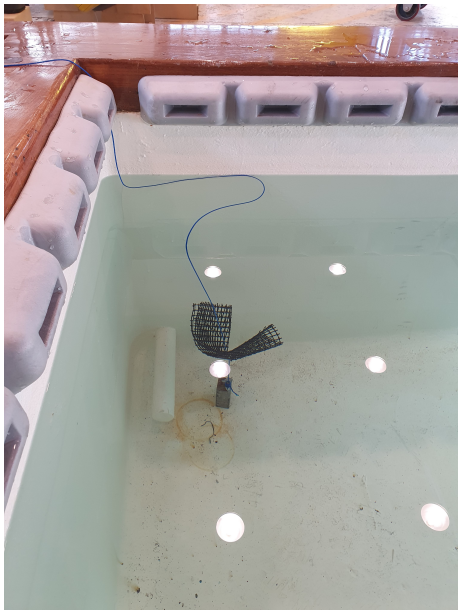

Figure A.5: The net was tested for any unexpected water soaking effects over a weekend.

B Model fatigue, breaking and reconstruction

Since there were no trusses between the two floaters, they were prone to rotational motion about the top of the cylinders, where they were fixed to the solar deck net and split-line rods. The most likely breaking mechanism was the waves interacting with the cylinders, pushing them in the direction of the incoming waves. Since only the top part of the cylinder is held in place in x-direction, the cylinders would rotate around their topmost point, bending the split line rods near the 90°angle. This was an oscillatory rotational motion, with the max amplitude of motion shown in Figure B.1. It resulted in fatigue in the 90 degree bend in one of the four split-line rods at the top end of each cylinder.

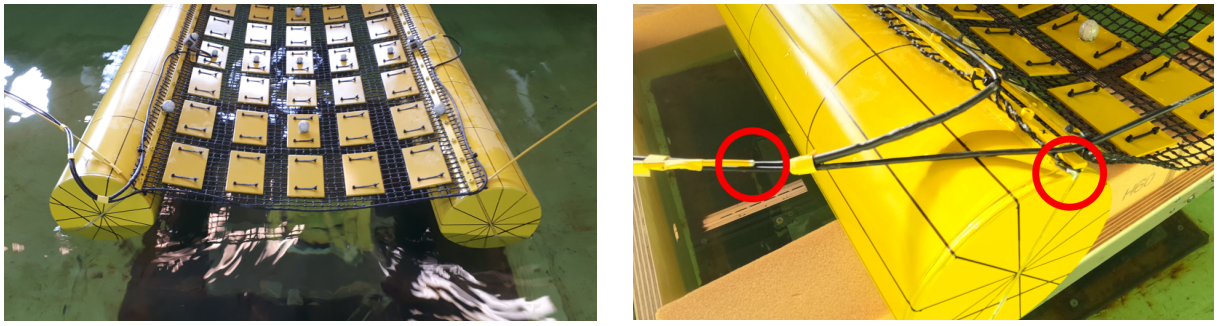

Figure B.1: Original model bending due to wave forces, leading fatigue from this repeated bending in the split-line rod at the 90 degree angle bend over the cylinder top.

The model then had to be redesigned with this bending in mind, and some extra stiffness around the 90 degree bend in the rod was added. The author of this thesis suggested including a frame of smaller triangles for increased stiffness instead of one bigger triangle, as this was believed to increase the rotational stiffness of each cylinder to a larger extent than one extra load-bearing member. The model constructor team then came up with the idea to make the added framework in the shape of a single rod, bent appropriately beforehand. This pre-bent rod in one piece was adhered to the original rod and cylinder with screws, glue, and plastic strips.

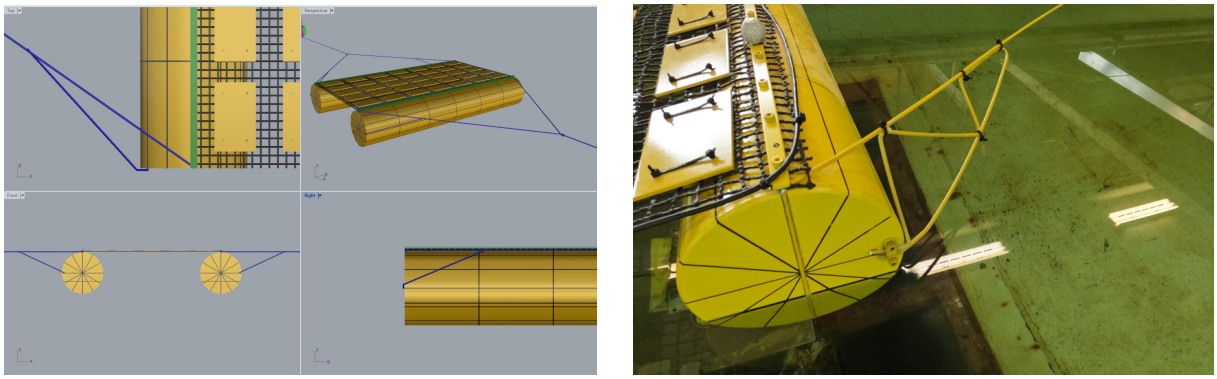

Figure B.2: Projected stiffeners on the improved model, and the resulting stiffeners. The resulting stiffness was satisfactory.

C Feasibility of including an actuator in the model tests

The winching actuator that was meant to be included in the model tests was an actuator rotating a screw-like member, making a trolley slide with translational motion. This actuator is shown in Figure C.1. This was controlled by Bluetooth, meaning that somewhat easy model scale test implementations could have been made. The actuator took input in the form of desired positions of the trolley. The actuator did not have feedback on the tension however, so this would have had to be measured and calibrated based on the position of the trolley.

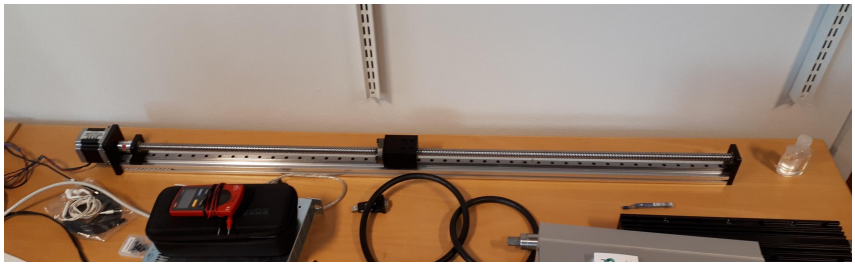

Figure C.1: Screw actuator that could have been included in the model tests, if it had been powerful enough.

If this actuator had been included in the model tests, the only remaining step away from a closed loop-system would have been the measured tension from the force rings seen in Figure 4.6 being available as real-time data to the computer running the control system code. This would have enabled the control program to compare the natural frequency calculated as a function of the tension and the frequency of the waves, assessing the likelihood of resonant vibrations, and if so sending commands to change the tension and natural frequency of the solar deck. However, a simplified method to achieve this could have been implemented by calibrating the tension measured in the solar deck as a function of its position, since the x-position changed for varying tension levels, as seen in Figure 5.1. This would require interpolating the tension between noted tension levels for given positions of the model, assuming that the springs on each side of the model were linearly elastic.

D Regular wave FFT testing

Regular wave period 0.5 s, solar deck tension 25 N

10 Hz sampling frequency shown in Figure D.1.

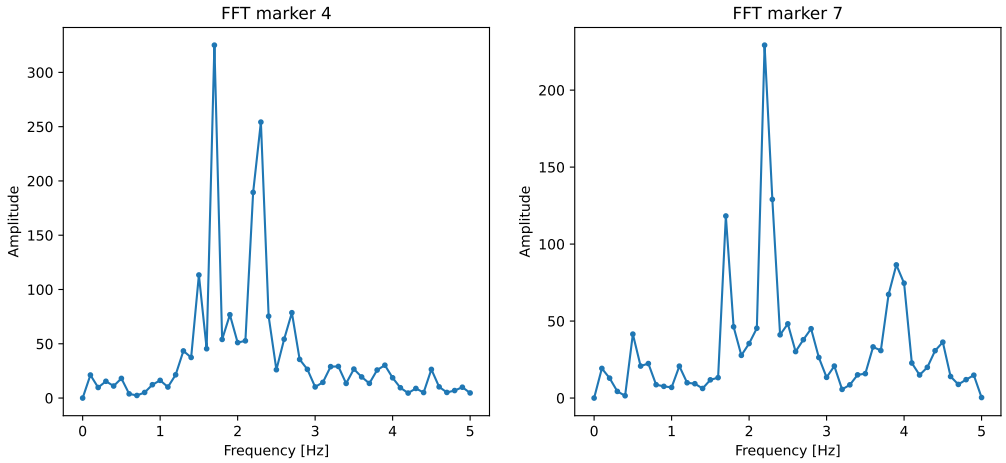

Figure D.1: FFT for marker 4 and 7 vertical motion. Regular wave period 0.5 s, force 25 N, wave height 0.02 m, and FFT sampling rate 10 Hz. Max value frequency (at peak) 1.7 Hz for marker 4 and 2.2 Hz for marker 7.

50 Hz sampling frequency shown in Figure D.2.

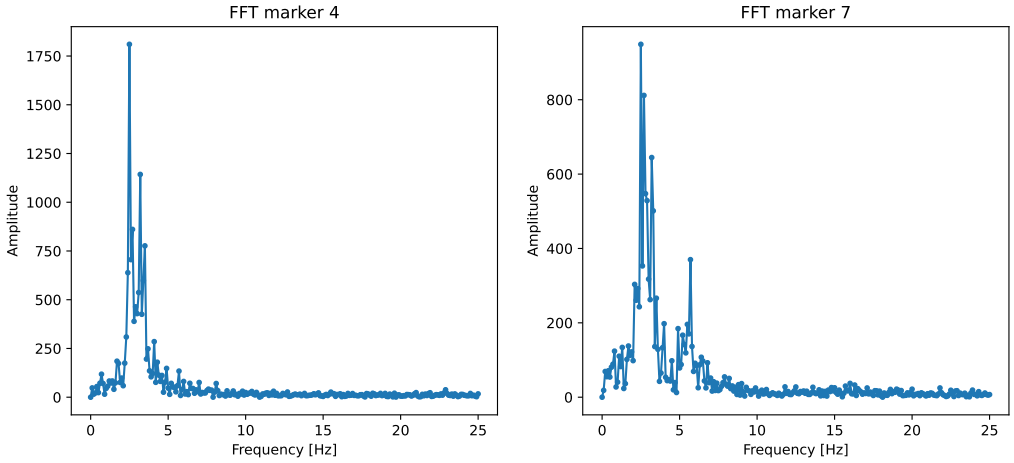

Figure D.2: FFT for marker 4 and 7 vertical motion. Regular wave period 0.5 s, force 25 N, wave height 0.02 m, FFT sampling rate 50 Hz. Max value frequency (at peak) 2.5 Hz for marker 4 and marker 7.

Regular wave period 0.5 s, solar deck tension 45 N

10 Hz sampling frequency shown in Figure D.3.

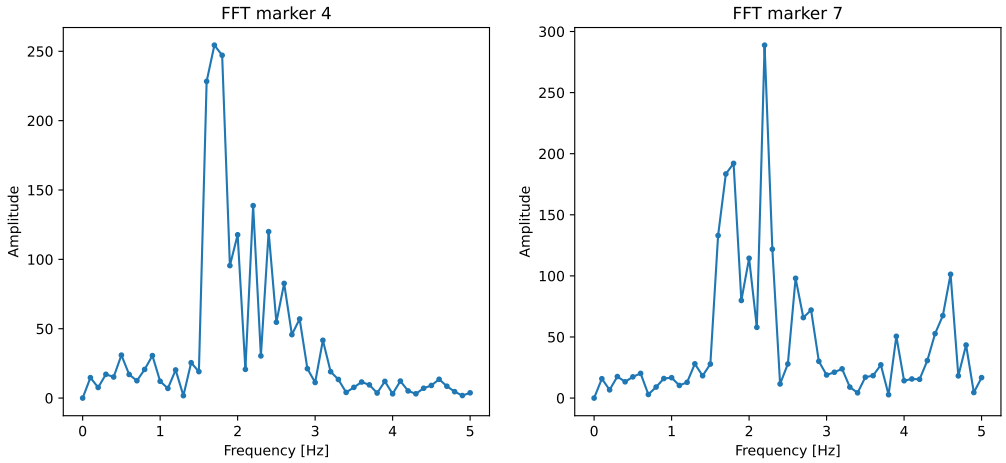

Figure D.3: FFT for marker 4 and 7 vertical motion. Regular wave period 0.5 s, force 45 N, wave height 0.02 m, FFT sampling rate 10 Hz. Max value frequency (at peak) 1.7 Hz for marker 4 and 2.2 Hz for marker 7.

50 Hz sampling frequency shown in Figure D.4.

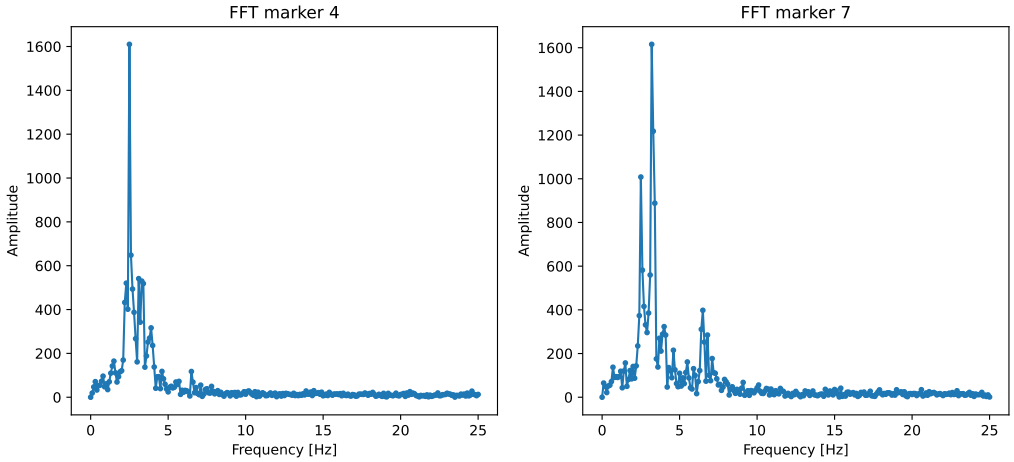

Figure D.4: FFT for marker 4 and 7 vertical motion. Regular wave period 0.5 s, force 45 N, wave height 0.02 m, FFT sampling rate 50 Hz. Max value frequency (at peak) 2.5 Hz for marker 4 and 3.2 Hz for marker 7.

Regular wave period 1.0 s, solar deck tension 25 N

10 Hz sampling frequency shown in Figure D.5.

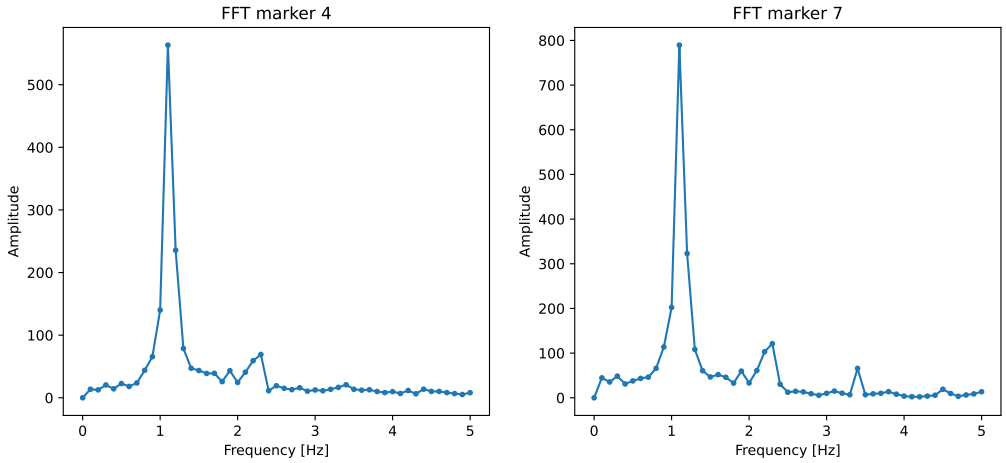

Figure D.5: FFT for marker 4 and 7 vertical motion. Regular wave period 1.0 s, force 25 N, wave height 0.02 m, FFT sampling rate 10 Hz. Max value frequency (at peak) 1.1 Hz for marker 4 and marker 7.

50 Hz sampling frequency shown in Figure D.6. Some $n \cdot \omega$ effects can in Figure D.5 and Figure D.6 be seen for tension 25 N. They are seen by spikes appearing at a whole number times the peak frequency.

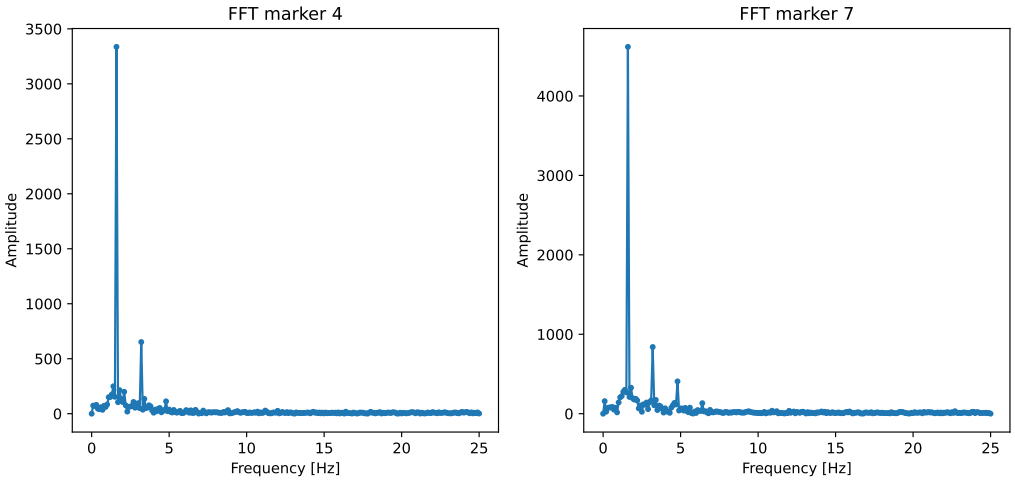

Figure D.6: FFT for marker 4 and 7 vertical motion. Regular wave period 1.0 s, force 25 N, wave height 0.02 m, FFT sampling rate 50 Hz. Max value frequency (at peak) 1.6 Hz for marker 4 and marker 7.

Regular wave period 1.0 s, solar deck tension 45 N

10 Hz sampling frequency shown in Figure D.7.

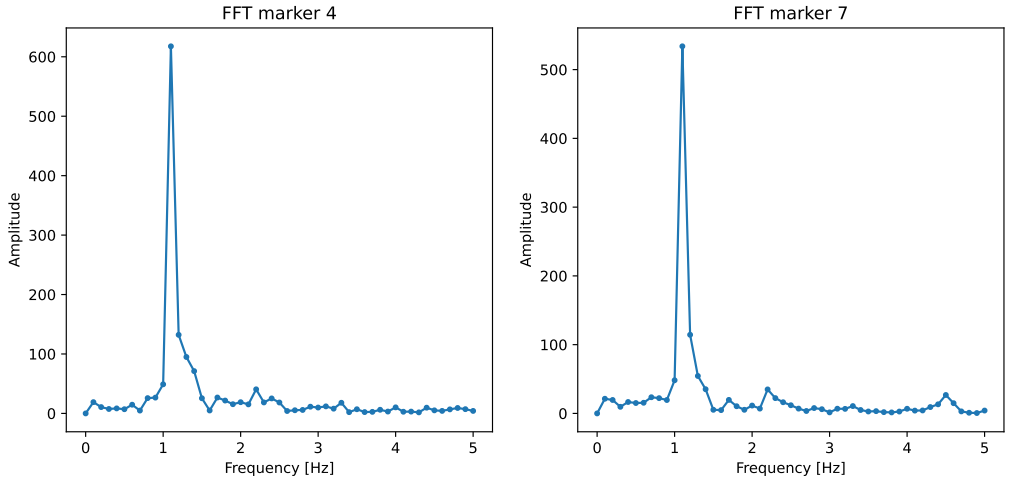

Figure D.7: FFT for marker 4 and 7 vertical motion. Regular wave period 1.0 s, force 45 N, wave height 0.02 m, FFT sampling rate 10 Hz. Max value frequency (at peak) 1.1 Hz for marker 4 and marker 7.

50 Hz sampling frequency shown in Figure D.8. Some $n \cdot \omega$ effects can be seen for 45 N in Figure D.7 and Figure D.8 as well, but to a lesser degree than for a 25 N tension level.

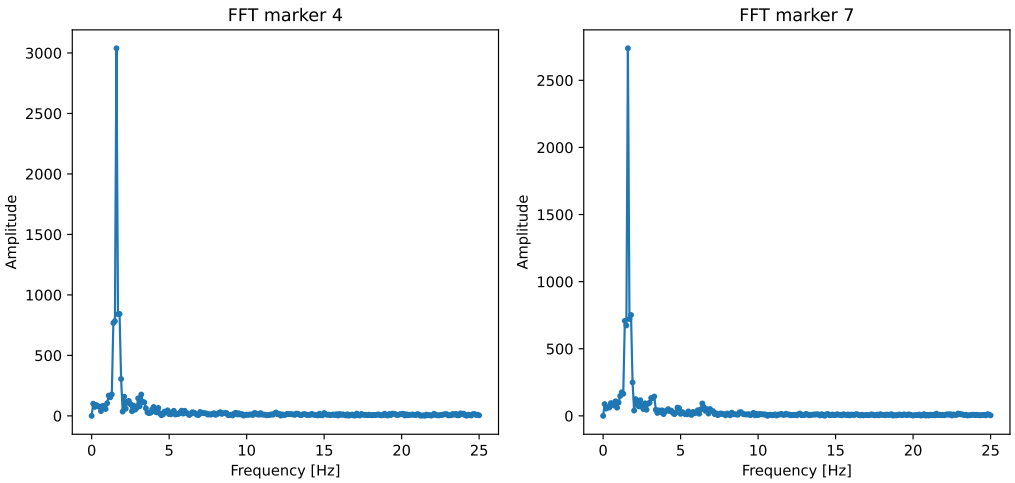

Figure D.8: FFT for marker 4 and 7 vertical motion. Regular wave period 1.0 s, force 45 N, wave height 0.02 m, FFT sampling rate 50 Hz. Max value frequency (at peak) 1.6 Hz for marker 4 and marker 7.

Regular wave period 1.5 s, solar deck tension 25 N

10 Hz sampling frequency shown in Figure D.9.

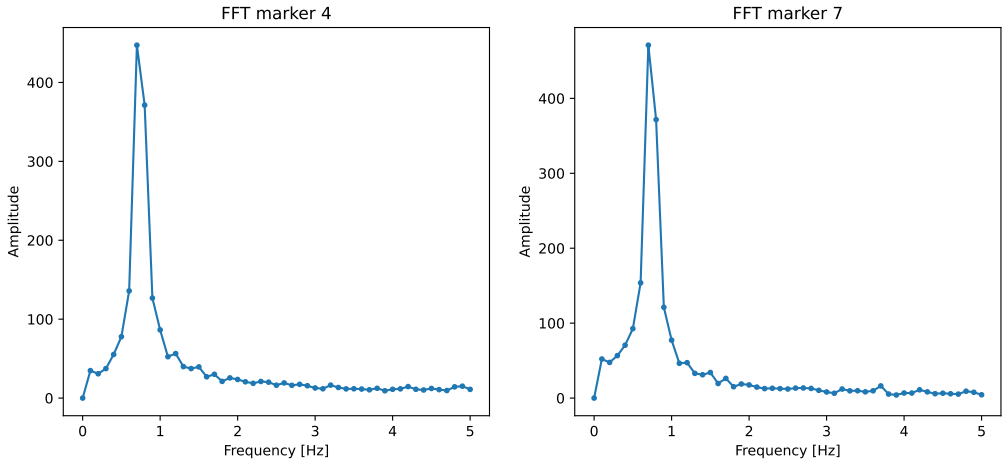

Figure D.9: FFT for marker 4 and 7 vertical motion. Regular wave period 1.5 s, force 25 N, wave height 0.02 m, FFT sampling rate 10 Hz. Max value frequency (at peak) 0.7 Hz for marker 4 and marker 7.

50 Hz sampling frequency shown in Figure D.10

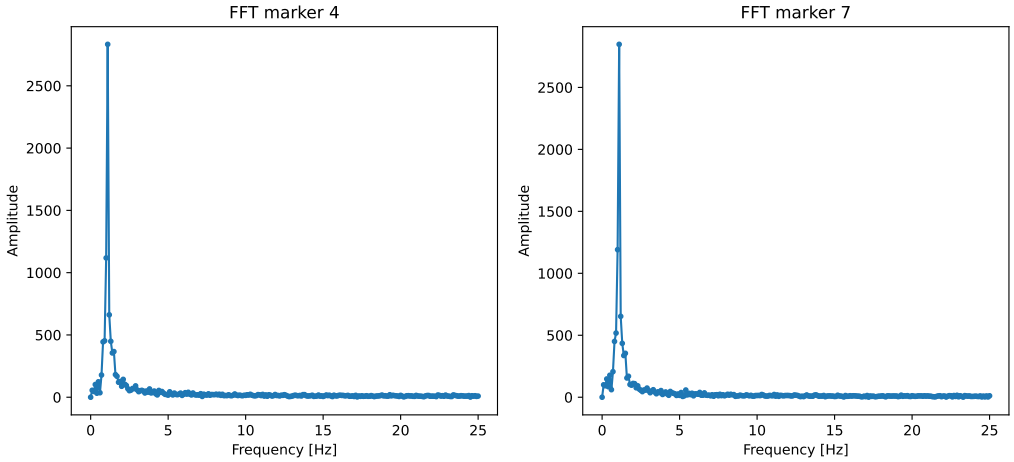

Figure D.10: FFT for marker 4 and 7 vertical motion. Regular wave period 1.5 s, force 25 N, wave height 0.02 m, FFT sampling rate 50 Hz. Max value frequency (at peak) 1.1 Hz for marker 4 and marker 7.

Regular wave period 1.5 s, solar deck tension 45 N

10 Hz sampling frequency shown in Figure D.11.

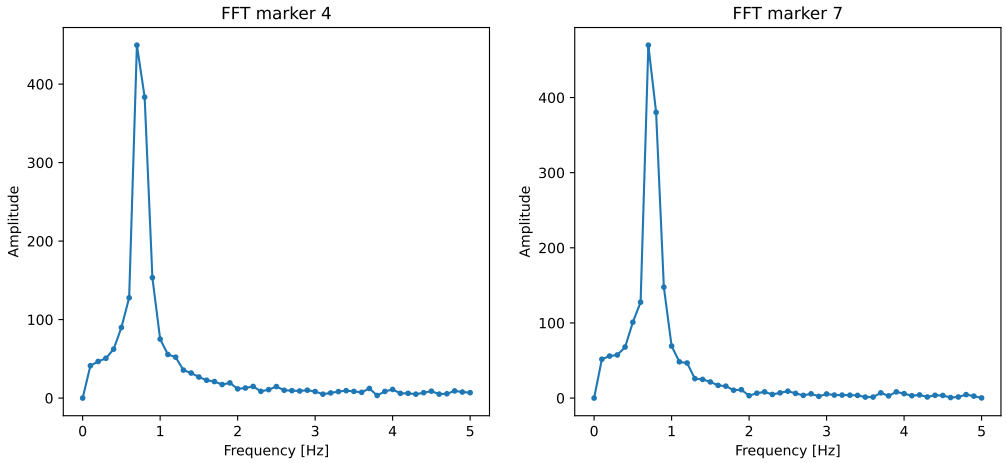

Figure D.11: FFT for marker 4 and 7 vertical motion. Regular wave period 1.5 s, force 45 N, wave height 0.02 m, FFT sampling rate 10 Hz. Max value frequency (at peak) 0.7 Hz for marker 4 and marker 7.

50 Hz sampling frequency shown in Figure D.12.

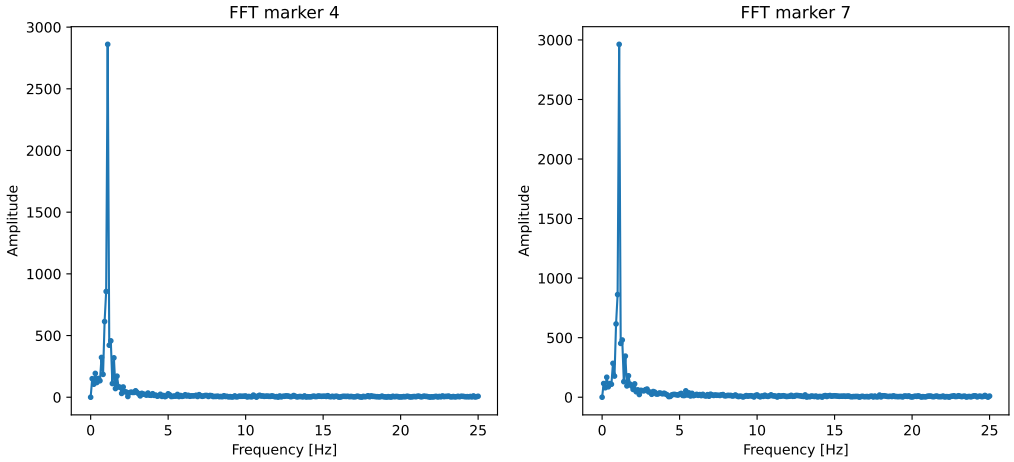

Figure D.12: FFT for marker 4 and 7 vertical motion. Regular wave period 1.5 s, force 45 N, wave height 0.02 m, FFT sampling rate 50 Hz. Max value frequency (at peak) 1.1 Hz for marker 4 and marker 7.

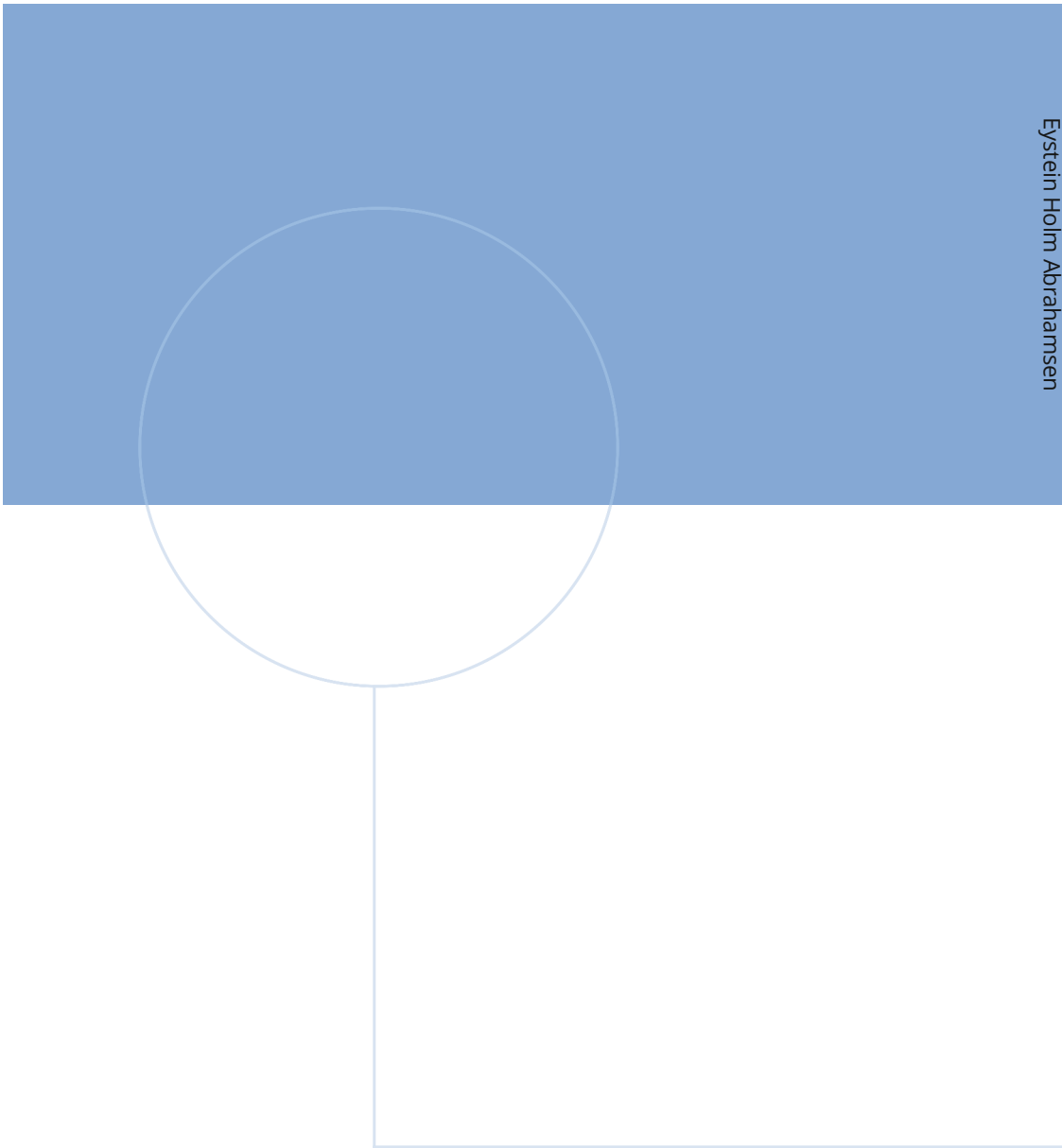

Eystein Holm Abrahamsen

NTNU
Norwegian University of
Science and Technology